Springer Theses
Recognizing Outstanding Ph.D. Research

Matthew J. Cliffe

Longitudinally Polarised Terahertz Radiation for Relativistic Particle Acceleration

Springer

Springer Theses

Recognizing Outstanding Ph.D. Research

Aims and Scope

The series "Springer Theses" brings together a selection of the very best Ph.D. theses from around the world and across the physical sciences. Nominated and endorsed by two recognized specialists, each published volume has been selected for its scientific excellence and the high impact of its contents for the pertinent field of research. For greater accessibility to non-specialists, the published versions include an extended introduction, as well as a foreword by the student's supervisor explaining the special relevance of the work for the field. As a whole, the series will provide a valuable resource both for newcomers to the research fields described, and for other scientists seeking detailed background information on special questions. Finally, it provides an accredited documentation of the valuable contributions made by today's younger generation of scientists.

Theses are accepted into the series by invited nomination only and must fulfill all of the following criteria

- They must be written in good English.
- The topic should fall within the confines of Chemistry, Physics, Earth Sciences, Engineering and related interdisciplinary fields such as Materials, Nanoscience, Chemical Engineering, Complex Systems and Biophysics.
- The work reported in the thesis must represent a significant scientific advance.
- If the thesis includes previously published material, permission to reproduce this must be gained from the respective copyright holder.
- They must have been examined and passed during the 12 months prior to nomination.
- Each thesis should include a foreword by the supervisor outlining the significance of its content.
- The theses should have a clearly defined structure including an introduction accessible to scientists not expert in that particular field.

More information about this series at http://www.springer.com/series/8790

Matthew J. Cliffe

Longitudinally Polarised Terahertz Radiation for Relativistic Particle Acceleration

Doctoral Thesis accepted by
the University of Bristol, Bristol, England

Springer

Author
Dr. Matthew J. Cliffe
School of Physics and Astronomy
The University of Manchester
Manchester
UK

and

The Cockcroft Institute
Sci-Tech Daresbury
Daresbury, Warrington
UK

Supervisors
Dr. Darren M. Graham
School of Physics and Astronomy
The University of Manchester
Manchester
UK

and

The Cockcroft Institute
Sci-Tech Daresbury
Daresbury, Warrington
UK

Prof. Wendy R. Flavell
School of Physics and Astronomy
The University of Manchester
Manchester
UK

Dr. Steven P. Jamison
The Cockcroft Institute
Sci-Tech Daresbury
Daresbury, Warrington
UK

and

Darebsury Laboratory, Accelerator Science
and Technology Centre, Science
and Technology Facilities Council
Daresbury, Warrington
UK

ISSN 2190-5053
Springer Theses
ISBN 978-3-319-48642-0
DOI 10.1007/978-3-319-48643-7

ISSN 2190-5061 (electronic)

ISBN 978-3-319-48643-7 (eBook)

Library of Congress Control Number: 2016956174

Printed on acid-free paper

This Springer imprint is published by Springer Nature
The registered company is Springer International Publishing AG
The registered company address is: Gewerbestrasse 11, 6330 Cham, Switzerland

Supervisors' Foreword

Particle accelerators have become indispensable tools in the search for new subatomic particles, in medical therapy, and in materials inspection. While physicists have been refining particle accelerators for over 80 years, their basic principle of operation has remained the same as the first radio frequency (RF) linear accelerator demonstrated by Rolf Wideröe in 1927. The use of RF acceleration techniques, and in particular the use of RF accelerating cavities, limits the maximum acceleration gradient. With accelerators on the multi-km scale, and a push for compact industrial and medical accelerators, there is a desire for a reduction in the size and cost which requires a new approach.

The acceleration of charged particles with ultrafast terahertz electromagnetic radiation could improve many aspects of accelerator operation and lead to new applications. In addition to overcoming the acceleration gradient limit, it could also enhance our ability to synchronise an accelerator to an external laser and provide shorter electron bunches for ultrafast time-resolved pump-probe spectroscopy.

In his thesis work, Matthew Cliffe developed terahertz radiation sources with attractive properties for accelerator-based applications. These include a radially biased large-area photoconductive antenna (PCA) that provided the largest longitudinally polarised terahertz electric field component ever measured from a PCA. While a number of approaches have been taken in recent years to develop such sources in the terahertz spectral region, the longitudinal field amplitudes have typically been less than 30 Vcm^{-1}, far below the field strengths required for particle acceleration. The detailed characterisation work carried out by Matthew showed that by using a 76-mm-diameter GaAs photoconducting antenna, a longitudinal component with a peak amplitude of 2.22 $\mathrm{kV\ cm}^{-1}$ could be obtained. Matthew subsequently used this radially biased PCA in conjunction with an energy recovery linear accelerator at the Daresbury Laboratory for electron acceleration experiments.

To enable even higher longitudinally polarised terahertz electric field strengths to be obtained, together with the ability to temporally tune the terahertz radiation, Matthew explored the potential of nonlinear optical crystals for terahertz generation. Magnesium-oxide-doped stoichiometric lithium niobate (MgO:SLN) has

become a popular non-linear material for use in the generation of linearly polarised terahertz radiation with a high peak electric field strength. Terahertz sources with electric field amplitudes in excess of 1 MVcm^{-1} have previously been realised by employing a pulse-front-tilt pumping scheme to enable the coherent transverse addition of the Cherenkov terahertz emission. Such sources are, however, linearly polarised and produce only weak longitudinally polarised components when focused. In order to apply these sources to accelerator applications requires conversion to a mode with a strong longitudinally polarised component, such as a radially polarised mode. As it is impractical to employ a radially segmented MgO:SLN generation scheme with a single pump beam, Matthew developed a novel scheme employing a matched pair of polarity-inverted MgO:SLN crystals. The interferometric recombination of the two polarity-inverted terahertz pulses effectively formed a Hermite-Gaussian 01 (HG01) spatial mode and enabled the generation of longitudinally polarised single-cycle terahertz radiation with an electric field amplitude of 11.7 kV cm^{-1}. Matthew found excellent agreement between the measured spatial, temporal, and polarisation properties of this source and the results of terahertz beam propagation calculations. Furthermore, Matthew showed that by using commonly employed techniques this generation method could in principle be scaled to produce longitudinally polarised terahertz electric fields with field amplitudes in excess of 1 MV cm^{-1}.

Manchester
August 2016

Dr. Darren M. Graham
Prof. Wendy R. Flavell
Dr. Steven P. Jamison

Abstract

The acceleration of charged particles with ultrafast terahertz electromagnetic radiation could enable new, and improve many of aspects of, accelerator applications. These include providing shorter electron bunches for ultrafast time-resolved pump-probe spectroscopy, enabling complex longitudinal profiles to be imparted onto charged particle bunches, and significantly improving the ability to synchronise an accelerator to an external laser.

In this thesis, I present investigations into terahertz radiation sources that enabled the generation of terahertz radiation with attractive properties for accelerator-based applications. Specific attention has been paid to temporally tunable sources that generate strong longitudinally polarised electric field components as these enable a free-space colinear interaction geometry to be implemented. A simulation describing the propagation of radiation from such sources has been developed. Terahertz sources have been designed, and the radiation generated is characterised *via* electro optic detection. These include a radially biased photoconductive antenna (PCA)-based source of which the longitudinally polarised terahertz electric field component was found to have an amplitude of 2.22 kV cm^{-1} as well as a near-single-cycle temporal profile. This radially biased PCA was used in conjunction with the Accelerators and Lasers in Combined Experiments (ALICE) energy recovery linear accelerator at the Daresbury Laboratory in an electron acceleration experiment.

To enable higher longitudinally polarised terahertz electric field strengths to be obtained, as well as the ability to temporally tune the terahertz radiation, generation within nonlinear optical crystals was investigated. Magnesium-oxide-doped stoichiometric lithium niobate (MgO:SLN) was investigated as a possible candidate due to its high nonlinear susceptibility tensor and reported ability to impose temporal tuning directly from the pump laser beam. A scheme consisting of two MgO:SLN crystals, each generating a separate linear polarised terahertz pulse which were then combined *via* a lens, was designed and built. Electro optic detection techniques were used to characterise the radiation generated from this source. Peak terahertz electric fields amplitudes of 11.6 and 47 kV cm^{-1} were measured for both the longitudinally and transversely polarised field components,

respectively. Temporal profiles measured from both the longitudinally and transversely polarised electric field components showed electric field periods of approximately 300 fs. This method of generating terahertz radiation employed a pulse-front-tilt technique. Allowing for the same scaling as recently reported in the literature for MgO:SLN generation techniques, which will in principle allow this method to scale to longitudinally polarised terahertz electric field profiles in excess of 1 MV cm^{-1}.

Acknowledgements

Firstly, to my supervisors Dr. D.M. Graham, Dr. S.P. Jamison, and Prof. W.R. Flavell for giving me this opportunity and for their guidance. To Dr. B.F. Spencer, Dr. T. Thakker, and Dr. D.A. Walsh for all the help and advice they have given me over the years. To my friends and family for all their support, patience, and encouragement; and to Lisa for all the love and laughter.

Contents

1 Introduction 1
1.1 Optical Generation of Terahertz Radiation 3
1.1.1 Optical Generation of Longitudinally Polarised Terahertz Radiation 6
1.2 Terahertz Based Charged Particle Acceleration 8
1.3 Thesis Outline 9
References 11

2 Theoretical Background 15
2.1 Non-linear Wave Equation 15
2.2 Non-linear Polarisation 17
2.3 Terahertz Generation 18
2.3.1 Optical Terahertz Generation 18
2.4 Terahertz Detection 30
2.4.1 Thermal Terahertz Detectors 30
2.4.2 Electro-Optic Detection 32
2.5 Photoconductive Antenna Generation 39
2.6 Longitudinally Polarised Radiation 42
2.7 Acceleration of Charged Particles 44
2.7.1 Relativistic Motion 45
2.7.2 Acceleration Within an Electromagnetic Field 47
2.7.3 Acceleration with Terahertz Radiation 48
References 49

3 Experimental Apparatus 51
3.1 Laser Systems 51
3.2 Large Area Photoconductive Antenna 53
3.3 Accelerators and Lasers in Combined Experiments (ALICE) 54
3.3.1 Accelerator Beam Line 56
References 57

4 Radiation Propagation Simulation 59
4.1 Introduction 59
4.2 Theory 60
4.2.1 Linear Propagation 60
4.2.2 Focusing Beams 62
4.2.3 Adding a Bandwidth 67
4.2.4 Adding Complex Input Beams 70
4.3 Calculating the Longitudinal Component 74
4.4 Simulation Structure 77
4.5 Simulation Applications 78
4.6 Conclusion 83
References 83

5 ALICE Energy Modulation Induced by Terahertz Radiation (AEMITR) 85
5.1 Introduction 85
5.2 Experimental Setup 86
5.2.1 Terahertz Generation 86
5.2.2 Injection and Interaction 88
5.2.3 Terahertz Detection 89
5.3 Temporal Synchronisation 91
5.4 Electron Beam—Terahertz Alignment 92
5.5 Electron Beam Detection 93
5.6 Discussion and Conclusion 97
References 98

6 Photoconductive Antenna Generation 99
6.1 Introduction 99
6.2 Photoconductive Antenna 100
6.3 Optical Setup 101
6.4 Confirmation of Radially Polarised Terahertz Radiation 104
6.5 Profiling the Probe Beam 106
6.6 Detection Crystal Angles 107
6.7 Transversely Polarised Terahertz Radiation 109
6.8 Longitudinally Polarised Terahertz Radiation 112
6.9 Field Strength Calculation 117
6.10 Transverse and Longitudinally Polarised Comparison 119
6.11 Conclusion 121
References 122

7 Non-linear Optical Crystal Generation 123
7.1 Introduction 123
7.2 Design 126
7.3 Preliminary ZnTe Experiment 127
7.3.1 Introduction 127
7.3.2 Experimental Setup 127

7.3.3 Results . . . 129
7.3.4 Discussion . . . 131
7.4 Lithium Niobate Generation . . . 132
7.4.1 Crystals . . . 133
7.4.2 Experimental Setup . . . 135
7.4.3 Single Crystal Results . . . 136
7.4.4 Double Crystal Results . . . 137
7.4.5 Discussion . . . 138
7.5 Conclusion . . . 140
References . . . 140

8 Conclusions and Future Work . . . 143
Reference . . . 144

Appendix . . . 145

The Author . . . 149

Chapter 1
Introduction

Ever since their conception in the late 1920s to early 1930s particle accelerators have been extremely useful scientific instruments. Their applications range from ultrafast pump-probe spectroscopy [1, 2], capable of unveiling the universe on the smallest of time scales, to particle beam therapy [3], with the possibilities of medical applications. All of these applications depend upon the properties of the charged particles accelerated by the particle accelerator being accurately tuned. In recent years there has been a drive to control the properties of these particles ever more precisely and to push the limits of what can be achieved. Current particle accelerators are capable of producing electron bunches with temporal durations on picosecond timescales [4, 5]. These accelerators rely on radio frequency (RF) electromagnetic radiation to provide an electromagnetic potential through which the particles travel either gaining or losing energy depending upon their relative phase.

As radio frequency (RF) electromagnetic radiation has a temporal period on the order of 10s of nanoseconds it is very difficult to impose fine scale, i.e. sub-nanosecond, temporal structure to accelerated particle bunches. It would be attractive to use radiation with a shorter temporal period to impose a longitudinal energy modulation or even direct acceleration, thus giving the produced bunches a more tunable temporal structure. Lasers could be one possible solution to this problem, commonly providing radiation with short temporal periods, down to 10s fs, and very high peak electric field strengths, in excess of 1 G Vcm^{-1} [6]. The use of lasers for particle acceleration has been explored in recent years and problems that prevent it from being used within mainstream accelerators identified [7–9]. The main problem with using radiation with such a short temporal period is the phase slippage between the accelerating radiation and the charged particle bunch. Due to the difference in the velocity of the accelerating radiation and the charged particle bunch their relative phase will change as propagation occurs. If this phase slippage becomes more than half a cycle of the accelerating radiation then the section of the particle bunch that was previously experiencing a positive electric field starts to experience an equal but opposite electric field thus undoing any effect

M.J. Cliffe, *Longitudinally Polarised Terahertz Radiation for Relativistic Particle Acceleration*, Springer Theses, DOI 10.1007/978-3-319-48643-7_1

that was imposed upon it. This condition greatly reduces the feasibility and usefulness of the energy modulation of charged particles with optical laser radiation in free space. Even with ultra-relativistic electron bunches with energies in the 25 MeV regime a longitudinal interaction region of only 3 μm is possible before the electron bunch slips half a cycle out of phase. It would be ideal to identify a frequency regime in which the temporal period was short enough to provide fine scale temporal energy modulation but whilst being long enough to enable both the radiation and charged particle bunches to co-propagate in phase [7].

Terahertz radiation is radiation which exists within the 0.1×10^{12} and 10×10^{12} Hz region of the electromagnetic spectrum. Pulsed electromagnetic radiation within this region typically has a temporal duration on the order of 300 fs to 1 ps and can be produced with only a single electromagnetic oscillation. Radiation with temporal durations on this order would be able to propagate with a 25 MeV electron bunch up to around 1 m before they slip more than half a cycle out of phase. This distance is a vast improvement on the previous 3 μm possible with optical radiation. Whilst terahertz radiation does not possess the ultra-short temporal periods that optical laser radiation does it still has a temporal period much shorter than that of RF radiation, and is still able to impose fine longitudinal energy modulations that would either be impossible or extremely difficult with RF radiation. Possible applications of being able to co-propagate terahertz radiation with particle bunches and impose a longitudinal energy modulation include micro-bunching and laser to particle bunch synchronisation. Micro-bunching would be very useful for applications that use accelerator driven ultrafast light sources as it would be able to provide ultrafast radiation pulses with variable time delay between the pulses [7]. Such a concept can be seen in Fig. 1.1, where a single particle bunch is propagating in a co-linear fashion with a terahertz pulse. An energy modulation is imposed upon the particle bunch which then enters a set of bending magnets. As the particle bunch travels through the bending magnets, particles with different energies take different trajectories. They therefore take a different path length through the magnetic structure and are separated in time. At the exit of the magnets the electron bunch contains a longitudinal density distribution as a direct result of the energy

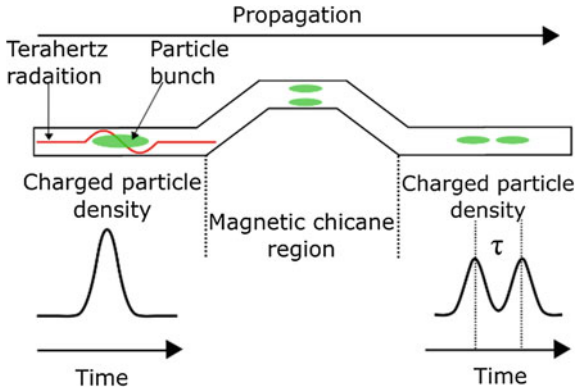

Fig. 1.1. Micro-bunching of an electron bunch (*green*) via the co-linear propagation with terahertz radiation (*red*) concept (Online color figure)

modulation imposed by the terahertz radiation. This density distribution will then be imposed upon any radiation that is produced by the electron bunch.

Accelerators are also increasingly being used in combination with lasers, as either a light source, such as in pump-probe spectroscopy, or in conjunction with laser radiation to generated new radiation, such as in free-electron lasers (FEL). Such applications whilst requiring specific electron bunch properties as mentioned above also require accurate synchronisation between both the accelerator and laser. With the recent progress in laser based single-cycle terahertz generation methods it is possible to see how terahertz radiation could be used in a post acceleration device to provide sub-10 fs temporal stability between a laser and a charged particle beam. Most of this recent progress has been aimed at increasing the peak electric field strength or improving the efficiency. Whilst these attributes are important for terahertz-accelerator applications the schemes listed above require the electron beam to interact with a longitudinally polarised electric field component. A terahertz source that combines both the high electric field strengths and polarisation states that allow for a dominant longitudinally polarised electric field component has not yet been created. Within this thesis the development of such a source is described, which involved both simulations and experimental characterisation.

1.1 Optical Generation of Terahertz Radiation

Optical generation of ultrafast single-cycle terahertz radiation can be split into three sections. The first being the optical rectification and difference frequency mixing of optical lasers within non-linear crystals, the second being the generation of terahertz radiation by the photoexcitation of a photoconductive antenna (PCA) and the third being plasma generation within air. Optical rectification was first demonstrated by Bass et al. in potassium dihydrogen phosphate (KDP) using a 100 ns ruby laser [8]. Since then this technique has been used for many different applications within many different fields, one of which has been the generation of terahertz radiation. The first demonstration of terahertz radiation generation within non-linear optical crystals was presented by Shen et al. in 1971 [9, 10]. This method used lithium niobate, a commonly used electro optic crystal within the field of optics, to generate picosecond pulses from a mode-locked optical laser. One of the most common crystal types for the optical generation of terahertz radiation is zinc blende cubic electro optic crystals such as zinc telluride (ZnTe) or gallium phosphide (GaP) cut in a (110) orientation [11, 12]. Terahertz generation within (110)-cut ZnTe typically uses an ultrafast femtosecond laser with a central wavelength of 800 nm and pulse durations on the 25–150 fs range. Typically radiation generated with such laser pulses within ZnTe has a frequency range of 0.1–3 THz and has pulse energies on the nJ scale [13]. Recently advances in pushing the pulse energy and electric field strength to even higher levels have been presented [14, 15]. ZnTe has a low saturation level due to the two-photon absorption that occurs at 800 nm. These advances have therefore taken the guise of increasing the crystal size and pump area [14, 15].

To date one of the highest terahertz pulse energies recorded from a ZnTe based source is 1.5 μJ. This was reported by Blanchard et al. in 2007 [14]. In this paper Blanchard et al. reported using a 75 mm diameter 0.5 mm thick (110)-cut ZnTe crystal in combination with a 48 μJ, 800 nm, 45 fs optical laser pulses. It is reported that terahertz radiation with a pulse energy of 1.5 μJ was generated leading to an efficiency of 3.1×10^{-5}. This efficiency is more than one order of magnitude greater than the efficiency, 1.5×10^{-6}, that was obtained from the excitation of small area ZnTe crystals by Kitaeva [13]. Given the large excitation region and relatively low excitation pulse energy this suggests that this method could still be scaled further.

In recent years different electro-optic crystals have been used with the aim of further increasing the generated terahertz pulse energy and electric field strength. A number of polymer materials such as 4-dimethylamino-N-methyl-4-stabazolium-tosylate (DAST), 4-N,N-dimethylamino-4′-N′-methyl-stilbazolium2,4,6-trimethyl benzenesulfonate (DSTMS) and 2-(3-(4-Hydroxystyryl)-5,5-dimethylcyclohex-2-enylidene)malononitrile (OH1) [16] are able to generate terahertz pulses with bandwidths up to, and in some cases beyond, 3 THz [17]. These new polymer materials have vastly improved the obtainable terahertz pulse energies and electric field strengths with pulse energies of 62, 150 and 270 μJ which correspond to electric field strengths of 6.2, 18 and 9.9 MV cm^{-1} being reported from DAST, DSTMS and OH1 respectively [18].

In addition to polymer based crystals different non-polymer based crystals have also been used such as lithium tantalite ($LiTaO_3$) and most notably lithium niobate ($LiNbO_3$). $LiNbO_3$ has a very large non-linear susceptibility tensor and so has the capabilities of generating terahertz radiation with high pulse energies and electric field strengths. Its advantages over polymer based crystals are not solely due to its large non-linear susceptibility tensor, as in comparison to some polymer crystals, such as OH1, the non-linear susceptibility is smaller. It is however more affordable, can be pumped with wavelengths more commonly available in scientific laboratories, and it is more resistant to optical damage and environmental contamination. There is however one drawback, in that the phase velocity in the terahertz regime is much smaller than the optical group velocity. This causes the generated terahertz radiation to slip out of phase with the generating optical radiation and gives rise to a maximum interaction length of 50 μm, negating the positives related to its large non-linear susceptibility tensor [13]. It was noticed that this effect gave rise to a Cherenkov cone of terahertz radiation that trailed the pump pulse, however due to the lack of phase addition the electric field strengths were as low as 10 V cm^{-1} [19, 20]. A solution to the lack of co-linear phase matching was suggested by Hebling et al. in 2002 [21]. This solution was to apply a pulse-front tilt to the optical pump beam. This technique enabled the projection velocity of the optical pump beam to be tuned, as described by

$$v_o^p = v_o^g \cos(\gamma), \tag{1.1}$$

where v_o^p is the projected velocity, v_o^g is the optical group velocity and γ is the tilt of the optical pump beam wavefront with respect to the propagation direction. This

enables the velocity to be matched to the phase velocity of the generated terahertz radiation. Phase addition could then occur in the direction perpendicular to the optical wavefront allowing for the generation of terahertz radiation with large pulse energies. This discovery lead to a number of papers being published with ever increasing terahertz pulse energies. In 2005 Stepanov et al. [22] demonstrated the ability to generate pulse energies of up to 240 nJ of terahertz radiation via the implementation of this method; an improvement of over 75 times when compared to a standard not employing the pulse-front tilt technique [22]. This number continued to grow rapidly over the next few years with Yeh et al. [23] reporting the generation of terahertz radiation with pulse energies of 10 μJ by this method [23]. In more recent years this has again been improved upon with Fulop et al. [24] reporting the generation of terahertz pulses with energies of up to 125 μJ generated via the same method [24]. This work continues to this day with ever increasing efficiencies and studies on the Hamster process reported [28–30].

Another commonly used optically based terahertz generation method involves the use of photoconductive antennas (PCAs). This method uses a semiconductor which is held under a large electrical bias field, the semiconductor surface is photo-excited via an incident optical pump laser liberating charge carriers from the valence band into the conduction band. These charge carriers then accelerate under the applied electrical bias field generating electromagnetic radiation with electric field oscillatory periods that are proportional to the time the charge carriers spend within the conduction band. Semiconductor materials such as gallium arsenide (GaAs) and indium phosphide (InP) are commonly used within such devices as their carrier lifetime is on the order of 100s of femtoseconds. PCAs were first suggested as a terahertz generation device as early as 1984 by Auston et al. [25]. These devices were originally only capable of producing low terahertz pulse energies in the sub-nJ regime. It was found that increasing the optical pump fluence did not increase terahertz pulse energies as the PCAs quickly saturated. It was instead found that it was more efficient to increase the applied electrical bias field and that the generated terahertz pulse energies scaled linearly with the applied electric bias [26, 27]. This lead to an increase in the producible terahertz pulse energies with You et al. [28] and Budiarto et al. [29] reporting terahertz pulse energies of 0.8 and 0.4 μJ respectively in 1993 and 1996 [28, 29]. Both of these publications report the use of large-area antennas with You et al. [28] reporting the use of a 1 cm electrode spacing and Budiarto et al. [29] reporting the use of a 3 cm electrode spacing. This increased pulse energy can be attributed not only to the increased antenna area but also to the increased electric bias field applied to the wafer and the increased optical pump pulse energy. Both You et al. [28] and Budiarto et al. [29] report electrical bias fields with multi-kV field values and optical laser pulse energies of 0.8 and 0.4 μJ respectively. As it can be difficult to work with large voltage fields a method of providing a high electric bias field to the wafer from a low voltage source was developed. This method involved splitting the large area of the wafer up into many identical sections. The electrodes which provide the electrical bias fields are then placed around these sections thus lowering the distance between the electrodes and hence increasing the electric bias field

whilst still enabling a large surface area to be used. This device is known as an interdigitated PCA and is commonly used throughout terahertz spectroscopy as both a terahertz source and detection device.

The spectral content of the terahertz radiation generated with these large area, high pulse energy antennas generally had a bandwidth of 0.1–1 THz with a spectral peak around the 0.3–0.5 THz region [26, 27]. As this device was typically used within the terahertz spectroscopic community a push towards increasing the bandwidth was made. To do this the trapping time of the semiconductor needed to be reduced and a method of doing so was proposed in 1988 by Smith et al. [30]. This new method involved a new semiconductor growing technique known as the low-temperature growth (LT) technique. By growing LT-GaAs wafers with the implantation of oxygen, silicon and nitrogen it was possible to reduce the charge carrier lifetime down to the sub-100 fs level and therefore extend the generated terahertz spectrum out towards 5 THz [31].

1.1.1 Optical Generation of Longitudinally Polarised Terahertz Radiation

Most of the progress achieved in the field of optical terahertz generation has been achieved with the generation of linearly polarised terahertz radiation. Many applications, such as spectroscopy, laser machining [32], laser tweezers [33], microscopy [34] and terahertz driven charged particle acceleration [7, 35], either require or would prefer a longitudinally polarised electric field component. All propagating electric fields contain a longitudinally polarised component, apart from azimuthally polarised radiation. However the longitudinally polarised component is generally negligible when compared to the transverse field. To obtain a pulse with a strong longitudinally polarised electric field component the pulse must have a transverse electric polarisation state with large spatial gradients, such as a radially polarised mode. Currently large-area PCAs appear to be the best candidates for being able to generate such a terahertz mode efficiently. This is due to their unique ability to tune the polarisation state simply by geometrically designing the electrodes.

Large-area PCAs capable of producing radially polarised radiation have been recently demonstrated, both with single gap [36, 37] and interdigitated [41–43] electrode structures. Whilst this idea has been shown to work and the desired polarisation state has been detected, via the polarisation sensitive detection method known as electro-optic detection, these methods generally are not able to produce large electric field strengths. To date all of these generation techniques have generated electric field amplitudes less than 30 V cm^{-1}.

Another possible method of optically generating terahertz radiation with strong longitudinally polarised electric field components include non-linear optical crystal

based methods. Currently this has been demonstrated using two different techniques. The first technique reported by Imai et al. [38] in 2012 involves cutting a crystal into different segments and then reassembling it such that each segment generates a linearly polarised component [38]. When all the linearly polarised components are combined in the far field a radially polarised beam is formed. Using this method Imai et al. [38] was able to generate a radially polarised terahertz beam. Both the transverse and longitudinally polarised field components were directly detectable as both a function of space and time. A peak longitudinally polarised electric field component of 30 V cm^{-1} was detected using this method however it is mentioned that replacing the GaP crystal with one that has a higher non-linear susceptibility could allow for this method to scale and potentially produce longitudinally polarised electric fields with higher amplitudes. A second technique was reported by Chang et al. [39] in 2007 and used the velocity mismatch which occurs between the pump laser and the terahertz radiation in a (001)-cut ZnTe crystal with a Yb-doped fibre amplifier [39]. In this case a Cherenkov cone of terahertz radiation was formed that trailed the optical pump radiation. Due to the symmetries involved in the crystal and pump beam polarisation state the generated radiation is symmetrical around the pump beam and thus generated a radially polarised beam. Again using this method Chang et al. [39] was able to measure both the transverse and longitudinally polarised electric field components as a function of both space and time, however this time a bolometer and terahertz polariser was used [39].

The final method of generating terahertz radiation with large longitudinally polarised electric field amplitude components to be discussed within this chapter is plasma generation in air. This generation technique takes an ultrafast optical laser with a high pulse energy and tightly focuses it in air. This ionises the air creating a plasma that is then manipulated in a variety of ways to generate terahertz radiation. These manipulation methods can be the pondermotive acceleration of electrons within the plasma and four-wave mixing of the optical pump beam in conjunction with its second harmonic to name a few [46–49]. By its very nature terahertz radiation generated by the pondermotive acceleration of electrons within a plasma is radially symmetrical and generates a radially polarised beam. However as of yet most applications of this generation technique have only used a linear polarised electric field component. Typically, these methods are able to generate transverse terahertz electric fields in the 100s kV cm^{-1} regime [13] and require lasers with very high pulse energies. Recently however there has been some interest in their ability to generate strong longitudinally polarised electric field components. Work carried out and published in 2013 by Minami et al. [40] reports the direct detection of the longitudinally polarised terahertz electric component generated via air-plasma generation. In this paper Minami et al. [40] reports that the peak longitudinally polarised terahertz electric field component was 1 kV cm^{-1} and that a 4.5 mJ 800 nm pump laser pulse was used [40].

As of yet the strongest optically generated longitudinally polarised terahertz electric field is 1 kV cm^{-1} and was generated air-plasma generation. However, it is

fair to assume that this could easily be scaled given a laser with higher pulse energies [40]. More surprisingly however is the lack of literature in the non-linear optical generation of terahertz radiation with strong longitudinally polarised electric field components within non-linear crystals. With the advent of the highly efficient optical rectification techniques within materials such as $LiNbO_3$ there seems to be a new avenue in the field of optical generation of terahertz radiation with strong longitudinal electric field components which has, as of yet, not been investigated.

1.2 Terahertz Based Charged Particle Acceleration

Accelerators utilising terahertz frequency radiation have a number of advantages over radio frequency based (RF) conventional accelerators. By using a higher frequency drive wave it is possible to surpass the breakdown limit found in conventional RF accelerators [41, 42]. It is also possible to have a much finer temporal control over the longitudinal dynamics of the charged particle bunch due to the shorter periods of the drive radiation [7]. As accelerators are increasingly being used in combination with ultrafast laser systems it is also advantageous to use drive radiation that is directly derived from a laser based source as this can provide much more stable and accurate synchronisation between the lasers being used and the charged particle bunches.

Recently the advances in ultrafast laser driven terahertz sources have enabled the idea of terahertz based electron acceleration to be realised. In 2012 Jamison et al. [7] reported the possibility of accelerating electron bunches using near single cycle terahertz pulses in free space [7]. Whilst in 2013 Wong et al. [43] reported theoretical calculations which suggested that near single cycle terahertz pulses, with the aid of a waveguide, would be able to accelerate electron bunches [43]. In 2014 Nanni et al. [42] showed experimental verification of Wong et al. [43] by accelerating electron bunches within a terahertz driven waveguide [42]. In this report Nanni et al. [42] use a lithium niobate based terahertz source to generate a linearly polarised near single cycle terahertz pulse. This pulse then propagated through a segmented half waveplate which converted the linearly polarised mode into a radially polarised mode. This radially polarised terahertz pulse was then coupled into a waveguide where it co-propagated with an electron bunch. In this report acceleration of 7 keV was reported with an accelerating gradient of 9.7 MVm^{-1}.

Other terahertz based acceleration concepts involving lithium niobate based waveguides which create propagating evanescent terahertz waves [44] and orthogonal metallic nano-tips [45] have also been demonstrated. In the lithium niobate waveguide concept relativistic protons are driven into a channel between two lithium niobate crystals as shown in Fig. 1.2a. Terahertz radiation is incident upon these crystals and propagates through creating evanescent waves which propagate across the surface at a velocity less than the speed of light. These evanescent waves create

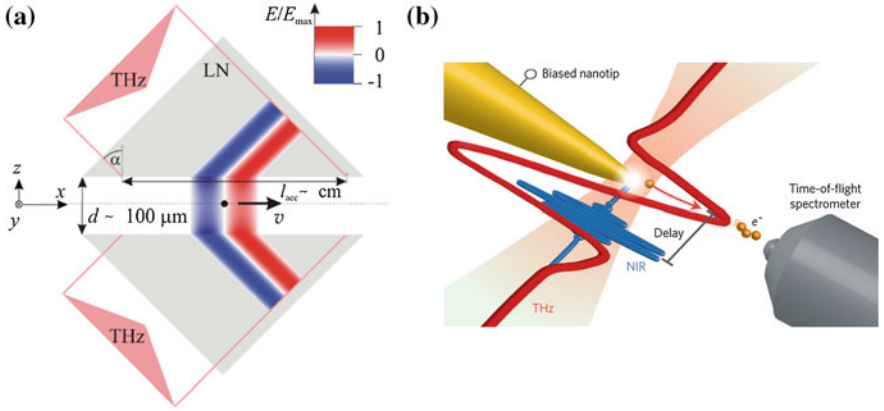

Fig. 1.2 Acceleration concepts proposed by **a** Palfalvi et al. [44] and **b** Wimmer et al. [45]

an accelerating gradient which then propagates along with the proton bunch enabling energy modulations to be imposed upon the bunch. There are two issues with this method, the high absorption and the large dispersion experienced by terahertz radiation propagating through $LiNbO_3$. The high absorption decreases the pulse energy of the terahertz radiation thus requiring the generation of higher pulse energies while the large dispersion distorts the electric field temporal profile. The latter effect removes one of the key advantages of using terahertz radiation for the acceleration of charged particle bunches, namely the near-single cycle electric field temporal profile. In the report by Wimmer et al. [45] published in 2014 an optical laser liberates electrons from a metallic nanotip. These electrons are then accelerated by a single cycle terahertz electric field which propagates orthogonally to the tip as shown in Fig. 1.2b. A time-of-flight spectrometer was then used to measure the acceleration undergone by the electrons as a result of the terahertz radiation. Electron energies on the order of 100 eV are measured by the time-of-flight spectrometer. As of yet all practical demonstrations of terahertz based acceleration use low energy non relativistic particle bunches. Scaling these techniques up to relativistic energies will enable techniques to be used more widely throughout the accelerator community as they will then be compatible with current conventional accelerator [7, 44].

1.3 Thesis Outline

Chapter 2 gives an overview of the theory used within this project. A derivation of the non-linear wave equation is presented along with a discussion of how this is utilised. Examples of how this theory extends to practical cases such as terahertz generation in ZnTe and MgO:SLN are also given. The theory of how other terahertz

generation techniques used such as the generation of terahertz radiation via the photoexcitation of large area photoconductive antennas (PCAs) is also presented. The fundamental concepts regarding charged particle acceleration are given including the requirements of the electromagnetic radiation providing the acceleration and the equations that govern the interaction. Devices used within this project such as various electronic terahertz detectors and are also described.

Chapter 3 gives an overview of the apparatus and equipment used within this project. The different laser systems used are listed along with their specifications and capabilities. The Accelerators and Lasers In Combined Experiments (ALICE) 25 MeV energy recovery linear accelerator which is based at the Daresbury STFC Laboratory is described along with some preliminary data obtained from experiments carried out on ALICE.

Chapter 4 describes a simulation that was developed to aid the design and understanding of the optical setups presented in Chaps. 5–7. The simulation used diffraction theory to take an arbitrary two-dimensional electric field distribution and propagate it through a number of optical elements to a two-dimensional output plane at a given distance away. Information such as the spatial distribution and temporal properties of the propagated electric field could be obtained. The effect of optical elements such as lenses and diffraction gratings could be investigated and their various properties optimised to produce the maximum desired output parameters. A derivation of the physics involved in this simulation are provided along with the reasoning behind the assumptions made and any limits these assumptions impose upon the applicability of the simulation.

Chapter 5 describes an experiment which was performed at the STFC Daresbury Laboratory using the ALICE accelerator. This experiment attempted to modulate the energy of a 25 MeV electron bunch via the co-propagation of terahertz radiation and a particle bunch. The terahertz frequency radiation used in this experiment was produced by a radially biased PCA that was pumped with a regenerative amplifier laser system. Alignment procedures and terahertz detection schemes are presented along with the results obtained. The detection optics, cameras and software developed are described along with the choices behind why the particular devices used were chosen.

Chapter 6 describes the characterisation of the radiation generated by a large-area PCA used within the experiment described in Chap. 6. Electro-optic detection was employed to detect the terahertz radiation and provided information regarding the temporal profile, polarisation state and spatial profile of the terahertz radiation. Electric field amplitudes were calculated for both the directly detected longitudinally polarised field and the transversely polarised field components.

Chapter 7 describes the design of a new terahertz longitudinally polarised terahertz radiation source. This source is based on optical rectification within MgO:SLN; a generation technique that has been shown in the literature to produce electric field amplitudes in excess of 10 MV cm^{-1}. As the technique presented only generated transversely polarised radiation a new geometrical generation technique was developed involving multiple crystals and the collection and combination of the radiation from these multiple crystals. Results from a preliminary proof-of-principle

experiment carried out using ZnTe crystals are presented along with the results obtained from a single crystal MgO:SLN generation scheme and finally the new multi-crystal generation scheme.

References

1. B.F. Spencer, M.J. Cliffe, D.M. Graham, S.J.O. Hardman, E.A. Seddon, K.L. Syres, A.G. Thomas, F. Sirotti, M.G. Silly, J. Akhtar, P. O'Brien, S.M. Fairclough, J.M. Smith, S. Chattopadhyay, W.R. Flavell, Chemically-specific time-resolved surface photovoltage spectroscopy: Carrier dynamics at the interface of quantum dots attached to a metal oxide. Surf. Sci. **641**, 320 (2015)
2. B.F. Spencer, D.M. Graham, S.J.O. Hardman, E.A. Seddon, M.J. Cliffe, K.L. Syres, A.G. Thomas, S.K. Stubbs, F. Sirotti, M.G. Silly, P.F. Kirkham, A.R. Kumarasinghe, G.J. Hirst, A.J. Moss, S.F. Hill, D.A. Shaw, S. Chattopadhyay and W.R. Flavell (2013) Time-resolved surface photovoltage measurements at n-type photovoltaic surfaces: Si(111) and ZnO $10\bar{1}0$, *Phys. Rev. B.* **88**, 195301
3. H. Owen, D. Holder, J. Alonso, R. Mackay, Technologies for delivery of proton and ion beams for radiotherapy. Int. J. Mod. Phys. A **29**, 1441002 (2014)
4. J.A. Clarke, D. Angal-Kalinin, N. Bliss, R. Buckley, S. Buckley, R. Cash, P. Corlett, L. Cowie, G. Cox, G.P. Diakun, CLARA conceptual design report. Journal of Instruments **9**, 5 (2014)
5. R. Ganter, SwissFEL *Conceptual Design Report*, Technical Report PSO Bsricht Nr 10-04 PSI, August 2015, ftp://ftp.psi.ch/psi/SwissFEL_CDR/SwissFEL_CDR_V20_23.04.12.pdf. Accessed July 2015 (Online)
6. E.L. Saldin, Terawatt-scale sub 10-fs Laser Technology- Key to Generation of GW-level Attosecond pulses in X-ray Free Electron Lasers. Optics Communications **237**, 35036127 (2004)
7. C. Varin, M. Piche, M.A. Porras, Acceleration of electrons from rest to GeV energies by ultrashort transverse magnetic laser pulses in free space. Phys. Rev. E **71**, 026603 (2005)
8. P. Fortin, M. Piche, C. Varin, Direct-field electron acceleration with ultrafast radially polarized laser beams: scaling laws and optimization. Journal of Physics B **43**, 025401 (2010)
9. L.J. Wong, F.X. Kartner, Two-Color-Laser-Driven Direct Electron Acceleration in Infinite Vacuum. Conference on Lasers and Electro-Optics, Baltimore **36**, 957–959 (2011)
10. S.P. Jamison, M.J. Cliffe, D.M. Graham, T. Thakker, B. Muratori, Y.M. Saveliev, R.J. Smith, W. R. Flavell, D.J. Holder, D. Newton and A. Wolski (2012) Phase space manipulation with laser-generated terahertz pulses, in *34th International Free Electron Laser Conference,* Japan
11. M. Bass, P.A. Franken, J.F. Ward, G. Weinreich, Optical Rectification. Phys. Rev. Lett. **9**, 446 (1962)
12. K.H. Yang, P.L. Richards, Y.R. Shen, Generation of Far-Infrared Radiation by Picosecond Light Pulses in $LiNbO_3$. Appl. Phys. Lett. **19**, 320 (1971)
13. B. Ferguson, X. Zhang, Materials for terahertz science and technology. Nat. Mater. **1**, 26 (2002)
14. G.L. Dakovski, B. Kubera, J. Shan, Localized terahertz generation via optical rectification in ZnTe. Optical Society of America B **22**, 1667 (2005)
15. P.C.M. Planken, H. Nienhuys, H.J. Bakke, T. Wenckebach, Measurement and calculation of the orientation dependence of terahertz pulse detection in ZnTe. Optical Society of America B **18**, 313 (2001)
16. G.K. Kitaeva, Terahertz generation by means of optical lasers. Laser Phys. Lett. **5**, 559 (2008)

17. F. Blanchard, L. Razzari, H.C. Bandulet, G. Sharma, R. Morandotti, J.C. Kieffer, T. Ozaki, M. Reid, H.F. Tiedje, H.K. Haugen, F.A. Hegmann, Generation of 1.5 μJ single-cycle terahertz pulse by optical rectificaiton from a large aperture ZnTe crystal. Opt. Express **15**, 13212 (2007)
18. T. Löffler, T. Hahn, M. Thomson, F. Jacob, H.G. Roskos, Lare-area electro-optic ZnTe terahertz emitters. Opt. Express **13**, 5353 (2005)
19. C. Vicario, C. Ruchert, C.P. Hauri, High field broadband THz generation in organic materials. J. Mod. Opt. **62**, 18 (2013)
20. M. Jazbinsek, B. Ruiz, C. Medrano and P. Gunter (2013) Broadband THz-wave generation with ogranic crystals OH1 and DSTMS, in *Conference on Lasers and Electro-Optics Europe*, Munich
21. C. Vicario, M. Jazbinsek, A.V. Ovchinnikov, O.V. Chefonov, S.I. Ashitkov, M.B. Agranat, C.P. Hauri, High efficiency THz generation in DSTMS, DAST and OH1 pumped by Cr:forsterite laser. Opt. Express **23**, 4573 (2015)
22. D.A. Bagdasarian, A.O. Makarian, P.S. Pogosian, Cherenkov radiation from a propagating nonlinear polarization wave. JETP Lett. **37**, 594 (1983)
23. D.H. Auston, K.P. Cheung, J.A. Valdmanis, D.A. Kleinman, Cherenkov Radiation from Femtosecond Optical Pulses in Electro-Optic Media. Phys. Rev. Lett. **53**, 1555 (1984)
24. J. Hebling, G. Almási, I.Z. Kozma, K. Jurgen, Velocity matching by pulse front tilting for large-area THz-pulse generation. Optical Express **10**, 1161 (2002)
25. A.G. Stepanov, J. Kuhl, I.Z. Kozma, E. Riedle, G. Almási, J. Hebling, Scaling up the energy of THz pulses created by optical rectification. Opt. Express **13**, 5762 (2005)
26. K.-L. Yeh, M.C. Hoffmann, J. Hebling, K.A. Nelson, Generation of 10 μJ ultrashort terahertz pulses by optical rectification. Appl. Phys. Lett. **90**, 171121 (2007)
27. J.A. Fülöp, L. Pálfalvi, S. Klingebiel, G. Almási, F. Krausz, S. Karsch, J. Hebling, Generation of sub-mJ terahertz pulses by optical rectification. Opt. Lett. **37**, 557 (2012)
28. D.H. Auston, K.P. Cheung, P.R. Smith, Picosecond photoconducting Hertzian dipoles. Appl. Phys. Lett. **45**, 284 (1984)
29. J.T. Darrow, X.-C. Zhang, D.H. Auston, Saturation Properties of Large-Aperture Photoconducting Antennas. IEEE J. Quantum Electron. **28**, 557 (1992)
30. P.K. Benicewicz, A.J. Taylor, Scaling of terahertz radiation from large-aperture biased InP photoconductors. Opt. Lett. **18**, 1332 (1993)
31. D. You, R.R. Jones, P.H. Bucksbaum, D.R. Dykaar, Generation of high-power sub-single-cycle 500-fs electromagnetic pulses. Opt. Lett. **18**, 290 (1993)
32. B. Budiarto, J. Margolies, S. Jeong, J. Son, J. Bokor, High-Intensity Terahertz Pulses at 1-kHz Repetition Rate. IEEE J. Quantum Electron. **32**, 1839 (1996)
33. F.W. Smith, A.R. Calawa, C.L. Chen, M.J. Manfra, L.J. Mahoney, New MBE buffer used to eliminate backgating in GaAs MESFETs. IEEE Journal on Electron Devices **9**, 77 (1988)
34. J. Lloyd-Hughes, E. Castro-Camus, M.D. Fraser, C. Jagadish, M.B. Johnston, Carrier dynamics in ion-implanted GaAs studing by simulation and observation of terahertz emission. Physical Review B **70**, 235330 (2004)
35. M. Meier, V. Romano, T. Feurer, Material processing with pulsed radially and azimuthally polarized laser radiation. Appl. Phys. A **86**, 329 (2007)
36. S.E. Skelton, M. Sergides, R. Saija, M.A. Lati, O.M. Marago, P.H. Jones, Trapping volume control in optical tweezers using cylinderical vector beams. Opt. Lett. **38**, 28 (2013)
37. D.P. Bliss, K.S. Youngworth, T.G. Brown, Dark-field imaging with cyliderical-vector beams. Appl. Opt. **45**, 470 (2006)
38. S. Payeur, S. Fourmaux, B.E. Schmidt, J.P. MacLean, C. Tchervenkov, F. Legare, M. Piche, J.C. Kieffer, Generation of a beam of fast electrons by tightly focusing a radially polarized ultrashort laser pulse. Appl. Phys. Lett. **101**, 041105 (2012)
39. S. Waselikowski, C. Fischer, J. Wallauer, M. Walther, Optimal plasmonic focusing on a metal disc under radially polarized terahertz illumination. New J. Phys. **15**, 075005 (2013)

40. M.J. Cliffe, A. Rodak, D.M. Graham, S.P. Jamison, Generation of longitudinally polarized terahertz radiation with field amplitudes exceeding 2 kV/cm. Appl. Phys. Lett. **105**, 1191112 (2014)
41. K. Kan, J. Yang, A. Ogata, S. Sakakihara, T. Kondoh, K. Norizawa, I. Nozawa, T. Toigawa, Y. Yoshida, H. Kitahara, K. Takano, M. Hangyo, R. Kuroda, H. Toyokawa, Radially polarized terahertz waves from a photoconductive antenna with microstuctures. Appl. Phys. Lett. **102**, 221118 (2013)
42. S. Winnerl, R. Hubrich, M. Mittendorff, H. Schneider, M. Helm, Universal phase relation between longitudinal and transverse fields observed in focused terahertz beams. New J. Phys. **14**, 103049 (2012)
43. S. Winnerl, B. Zimmermann, F. Peter, H. Schneider, M. Helm, Terahertz Bessel-Gaus beams of radially and azimuthal polarization from microstructured photoconductive antennas. Opt. Express **17**, 1571 (2009)
44. R. Imai, N. Kanda, T. Higuchi, Z. Zheng, K. Konishi, M. Kuwata-Gonokami, Terahertz vector beam generation using segmented nonlinear optical crystals with threefold rotation symmetry. Opt. Express **20**, 21896 (2012)
45. G. Chang, C.J. Davin, C. Liu, S.L. Williamson, A. Galvanauskas, T.B. Norri, Generation of radially polarized terahertz pulses via velocity-mismatched optical rectification. Opt. Lett. **32**, 433 (2007)
46. H. Hamster, A. Sullivan, S. Gordon, W. White, R.W. Falcone, Subpicosecond, Electromagnetic Pulses from Intense Laser-Plasma Interaction. Physical Review Letters **71**, 2725 (1993)
47. K.Y. Kim, J.H. Glownia, A.J. Taylor, G. Rodriguez, Terahertz emission from ultrafast ionizing air in symmetry-broken laser fields. Optics Express **15**, 4577 (2007)
48. J. Das, M. Yamaguchi, Terahertz wave excitation from preexisting air plasma. Optical Society of America B **30**, 1595 (2013)
49. L. Zhang, H. Zhong, C. Deng, C. Zhang, Y. Zhao, Terahertz wave polarization analyzer using birefrigent materials. Optics Express **17**, 20266 (2009)

Chapter 2
Theoretical Background

This chapter gives an overview of the theory used within this project. A derivation of the non-linear wave equation is presented along with a discussion of how this is utilised. Examples of how this theory extends to practical cases such as terahertz generation in ZnTe and MgO:SLN are also given. The theory of how other terahertz generation techniques used such as the generation of terahertz radiation via the photoexcitation of large area photoconductive antennas (PCAs) is also presented. The fundamental concepts regarding charged particle acceleration are given including the requirements of the electromagnetic radiation providing the acceleration and the equations that govern the interaction. Devices used within this project such as various electronic terahertz detectors and are also described.

2.1 Non-linear Wave Equation

Maxwell's equations explain how electromagnetic radiation changes as a function of time and space and are given by [1],

$$\nabla \overline{D}(\overline{x}, t) = 4\pi\rho, \tag{2.1}$$

$$\nabla \overline{B}(\overline{x}, t) = 0, \tag{2.2}$$

$$\nabla \times \overline{E}(\overline{x}, t) = -\frac{1}{c}\frac{\partial}{\partial t}\overline{B}(\overline{x}, t), \tag{2.3}$$

$$\nabla \times \overline{H}(\overline{x}, t) = \frac{1}{c}\frac{\partial}{\partial t}\overline{D}(\overline{x}, t) + \frac{4\pi}{c}\overline{J}(\overline{x}, t), \tag{2.4}$$

M.J. Cliffe, *Longitudinally Polarised Terahertz Radiation for Relativistic Particle Acceleration*, Springer Theses, DOI 10.1007/978-3-319-48643-7_2

where $\overline{D}(\bar{x},t)$ is the electric displacement vector, ρ is the density of free charge, $\overline{B}(\bar{x},t)$ is the magnetic field vector, $\overline{E}(\bar{x},t)$ is the electric field vector, c is the speed of light in a vacuum, t is time and $\overline{J}(\bar{x},t)$ is the current density. In free space there are no free charges and therefore $\rho = 0$ and $\overline{J} = 0$. The electric displacement vector, $\overline{D}(\bar{x},t)$, can be expressed in terms of $\overline{E}(\bar{x},t)$ by

$$\overline{D}(\bar{x},t) = \overline{E}(\bar{x},t) + 4\pi\overline{P}(\bar{x},t), \tag{2.5}$$

where $\overline{P}(\bar{x},t)$ is the polarisation vector and can be thought of as a localised value of $\overline{E}(\bar{x},t)$.

From these equations and assumptions, it is possible to derive the optical non-linear wave equation. First the curl of Eq. (2.3) is taken giving,

$$\nabla \times \nabla \times \overline{E}(\bar{x},t) = -\nabla \times \frac{1}{c}\frac{\partial}{\partial t}\overline{B}(\bar{x},t). \tag{2.6}$$

Interchanging the order of the spatial and temporal derivatives on the right hand side enables $\nabla \times \overline{B}$ to be replaced with $\frac{1}{c}\frac{\partial}{\partial t}\overline{D}(\bar{x},t) + \frac{4\pi}{c}\overline{J}(\bar{x},t)$ and also remembering that $\overline{J}(\bar{x},t) = 0$ gives the following expression,

$$\nabla \times \nabla \times \overline{E}(\bar{x},t) = -\frac{1}{c^2}\frac{\partial^2}{\partial t^2}\overline{D}(\bar{x},t). \tag{2.7}$$

It is now possible to replace $\overline{D}(\bar{x},t)$ with $\overline{E}(\bar{x},t)$ by using Eq. (2.5). This gives

$$\nabla \times \nabla \times \overline{E}(\bar{x},t) = -\frac{1}{c^2}\frac{\partial^2}{\partial t^2}\left[\overline{E}(\bar{x},t) + 4\pi\overline{P}(\bar{x},t)\right]. \tag{2.8}$$

Expanding the right hand side bracket and collecting the $\overline{E}(\bar{x},t)$ terms onto the right hand side yields,

$$\nabla \times \nabla \times \overline{E}(\bar{x},t) + \frac{1}{c^2}\frac{\partial^2}{\partial t^2}\overline{E}(\bar{x},t) = \frac{4\pi}{c^2}\overline{P}(\bar{x},t). \tag{2.9}$$

The vector identity $\nabla \times \nabla \times A = \nabla(\nabla \cdot A) - \nabla^2 A$ can now be applied to the first term in Eq. (2.9) where the assumption that the first term, $\nabla(\nabla \cdot A)$, is much smaller than the second term, $\nabla^2 A$, which is therefore neglected is applied. This then leaves Eq. (2.9) as,

$$-\nabla^2\overline{E}(\bar{x},t) + \frac{1}{c^2}\frac{\partial^2}{\partial t^2}\overline{E}(\bar{x},t) = \frac{4\pi}{c^2}\overline{P}(\bar{x},t). \tag{2.10}$$

In order to study the non-linear optical effects $\overline{P}$ is usually split into its linear and non-linear components, where $\overline{P} = \overline{P}^{(1)} + \overline{P}^{NL}$. $\overline{D}$ can also be split into its same linear and non-linear components. Using these definitions Eq. (2.10) becomes,

$$-\nabla^2\overline{E}(\overline{x},t) + \frac{\epsilon}{c^2}\frac{\partial^2}{\partial t^2}\overline{E}(\overline{x},t) = \frac{4\pi}{c}\overline{P}^{NL}(\overline{x},t), \tag{2.11}$$

where ϵ is the permittivity of the material through which the wave is propagating. From Eq. (2.11) it is possible to see how the non-linear polarisation acts as a source term for the generation of travelling waves. It is also possible to see how by setting the non-linear polarisation term to zero the solution to Eq. (2.11) takes the form of a propagating electromagnetic field with velocity $\frac{c}{\sqrt{\epsilon_0}}$ which is consistent with Maxwell's equations.

Currently Eq. (2.11) gives the wave equation with the nonlinear source term in the time domain. By applying the Fourier transform to $\overline{E}(\overline{x},t)$ and $\overline{P}^{NL}(\overline{x},t)$ it is possible to convert this into a wave equation with a nonlinear source term in the frequency domain

$$-\nabla^2\overline{E}(\overline{x},\omega) - \frac{\omega_n^2\epsilon(\omega_n)}{c^2}\overline{E}(\overline{x},\omega) = \frac{4\pi\omega_n^2}{c^2}\overline{P}^{NL}(\overline{x},\omega). \tag{2.12}$$

2.2 Non-linear Polarisation

The polarisation vector, $\overline{P}$, is a localised quantity that acts as a source term in the non-linear wave equation [2]. It is a measure of the dielectric polarisation density, with units of dipole moment per unit volume. The polarisation vector can be written as a Taylor series expansion,

$$\overline{P}(\overline{x},t) = \epsilon_0\left(\chi^{(1)}\overline{E}(\overline{x},t) + \chi^{(2)}\overline{E}(\overline{x},t)^2 + \chi^{(3)}\overline{E}(\overline{x},t)^3 + \ldots\right), \tag{2.13}$$

where $\overline{E}$ is the input electric field and $\chi^{(n)}$ are the n^{th} order susceptibilities which are properties of the material in which the interaction is taking place. For the process of terahertz generation within non-linear optical materials the second order non-linear susceptibility tends to dominate and so it is possible to write

$$\overline{P}(\overline{x},t) = \overline{P}^{(1)}(\overline{x},t) + \overline{P}^{(2)}(\overline{x},t). \tag{2.14}$$

Given the expression

$$\overline{P}^{(2)}(\overline{x},t) = \chi^{(2)}\overline{E}^2(\overline{x},t), \tag{2.15}$$

it is possible to express the generated second order polarisation term in the frequency domain by taking the Fourier transform of both $\overline{P}^{(2)}(\overline{x},t)$ and $\overline{E}^{2}(\overline{x},t)$ such that

$$\overline{P}^{(2)}(\overline{x},\omega)=\chi^{(2)}\int_{-\infty}^{\infty}\overline{E}(\overline{x},\Omega)\overline{E}(\overline{x},\omega-\Omega)d\Omega. \tag{2.16}$$

This now shows how the generated polarisation term in the frequency domain is the convolution of the optical input field.

2.3 Terahertz Generation

The term terahertz radiation generally refers to electromagnetic radiation that exists at frequencies within the range 0.1×10^{12} to 10×10^{12} Hz. The temporal properties of pulsed radiation within this frequency range make it ideal for the application to modulate the energy of relativistic particles. The generation of such radiation therefore is a key part of this work. Different generation techniques enable the possibility of tuning different physical properties of any generated terahertz radiation, each generation technique having its own individual positive points and difficulties. Within this section the different generation techniques relevant to this project is discussed. The theory behind how each method generates terahertz radiation is explained along with the positive and negative points related to each method with respect to the end goals of this project.

2.3.1 Optical Terahertz Generation

The generation of terahertz radiation within non-linear crystals is commonplace in many applications that use terahertz radiation. The physical process behind this generation technique is known as difference frequency mixing, or in certain special cases optical rectification. Optical rectification involves the non-linear reaction of a material to incident optical laser radiation. These generation techniques are second order non-linear effects and therefore can be described by the second order polarisation term [3],

$$\overline{P}_{3}^{(2)}(\overline{x},\omega)=\chi^{(2)}\overline{E}_{1}(\overline{x},\omega)*\overline{E}_{2}(\overline{x},\omega) \tag{2.17}$$

The generation of terahertz radiation relies on the process of difference frequency mixing such that

$$\overline{P}_3(\overline{x},\omega) = \chi^{(2)}\overline{E}_1(\overline{x},\omega)\overline{E}_2^*(\overline{x},\omega). \tag{2.18}$$

By defining $\overline{E}_1(\overline{x},\omega)$ and $\overline{E}_2^*(\overline{x},\omega)$ as,

$$\overline{E}_1(z,\omega) = A_1 e^{i(k_1 z)}, \tag{2.19}$$

$$\overline{E}_2^*(z,\omega) = A_2^* e^{-i(k_2 z)}. \tag{2.20}$$

Now using these expressions for E_1 and E_2 and placing them into Eq. (2.18) it is possible to obtain an expression of the form,

$$\overline{P}_3(\omega_3) = 2\chi^{(2)} A_1 A_2^* e^{i(k_1 - k_2)z}. \tag{2.21}$$

If the wave generated by polarisation term $P_3(\omega_3)$ is a travelling wave in the $+z$ direction then it should also be possible to express it as

$$\overline{E}_3(z,\omega_3) = A_3 e^{i(k_3 z)}. \tag{2.22}$$

Now by placing Eqs. (2.21) and (2.22) into the non-linear wave equation, Eq. (2.12),

$$\left[-\nabla^2 A_3 - 2ik_3\nabla A_3 + k_3^2 A_3 - \frac{\omega_3^2\epsilon(\omega_3)}{c^2}A_3\right]e^{i(k_3 z)} = \frac{8\pi\omega_3^2}{c^2}\chi^{(2)} A_1 A_2^* e^{i[(k_1-k_2)z]}. \tag{2.23}$$

Using the definition that $k_i = \frac{\sqrt{\epsilon(\omega_i)}\omega_i}{c}$ it is possible to see how the third and fourth terms within the first brackets cancel each other out. Also by defining the direction of propagation to only be allowed in the $+z$ direction it is possible to say $\nabla \approx \frac{\partial}{\partial z}$. The temporal term within the exponentials can also be cancelled from both sides and the exponential term can be dropped such that Eq. (2.23) now becomes,

$$\left[-\frac{\partial^2}{\partial z^2}A_3 - 2ik_3\frac{\partial}{\partial z}A_3\right]e^{ik_3 z} = \frac{8\pi\omega_3^2}{c^2}\chi^{(2)} A_1 A_2^* e^{i(k_1-k_2)z}. \tag{2.24}$$

A further approximation can now be made to this expression which is commonly known as the slowly varying envelope approximation (SVEA). The SVEA is valid for cases where the envelope of the pulse varies on larger lengths scales than the wavelength of the radiation. This approximation makes the assumption that the second order differential is much smaller than the first order differential i.e. in this case,

$$\left|\frac{\partial^2}{\partial z^2}A_3\right| \ll \left|k_3\frac{\partial}{\partial z}A_3\right|. \tag{2.25}$$

If this approximation is made and applied to the current wave equation expression then the first term in Eq. (2.24) can be neglected and Eq. (2.24) becomes,

$$\frac{\partial}{\partial z}A_3 = \frac{(i^2)8\pi\omega_3^2}{2ik_3c^2}\chi^{(2)}A_1A_2^*\frac{e^{i(k_1-k_2)z}}{e^{ik_3z}}, \tag{2.26}$$

which simplifies to

$$\frac{\partial}{\partial z}A_3 = \frac{i4\pi\omega_3}{c}\chi^{(2)}A_1A_2e^{i\Delta kz}, \tag{2.27}$$

where $\Delta k = k_1 - k_2 - k_3$ and is commonly called the wave vector mismatch. In order to obtain an expression such that A_3 is isolated the integral over z is performed on the right hand side such that Eq. (2.27) becomes

$$A_3 = \frac{i4\pi\omega_3}{c}\chi^{(2)}A_1A_2^*\int_0^L e^{i\Delta kz}dz, \tag{2.28}$$

where L represents the interaction length which is typically confined to the thickness of the non-linear material in which the interaction is taking place. Performing this integral leaves,

$$A_3 = \frac{i4\pi\omega_3}{c}\chi^{(2)}A_1A_2^*\left(\frac{e^{i\Delta kL}-1}{i\Delta k}\right). \tag{2.29}$$

It is common practice to analyse the output of the newly generated propagating wave in terms of its intensity which can be defined in terms of A_i as,

$$I_i = \frac{n_ic}{2\pi}|A_i|^2, \tag{2.30}$$

where the index i denotes the wave either 1, 2 or 3. Using this definition and applying it to Eq. (2.29) it is possible to write,

$$I_3 = \frac{n_3c}{2\pi}\frac{16\pi^2\omega_3^2}{c^2}\chi^{(2)^2}|A_1|^2|A_2^*|^2\left|\frac{e^{i\Delta kL}-1}{\Delta k}\right|^2. \tag{2.31}$$

The squared modulus can be re-expressed as a sinc function, described in Appendix A.1, such that Eq. (2.31) now becomes,

$$I_3 = \frac{n_38\pi\omega_3^2}{c}\chi^{(2)^2}I_1I_2\,\mathrm{sinc}^2\left(\frac{\Delta kL}{2}\right). \tag{2.32}$$

It can now be seen that the intensity of the newly generated wave is dependent upon the square of the non-linear material property $\chi^{(2)}$, and is linearly dependent

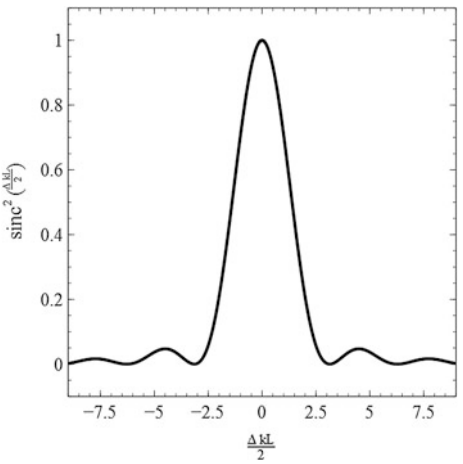

Fig. 2.1 $\sin c^2\left(\frac{\Delta kL}{2}\right)$ plotted as a function of $\frac{\Delta kL}{2}$ which represents the phase matching effects on the efficiency of difference-frequency generation

upon the product of the two input intensities I_1 and I_2. Currently this expression describes two monochromatic beams producing a third monochromatic beam with the frequency given by the difference in the input beam frequencies. This however can also be expanded such that only one input beam is present and both the input frequencies are contained within this one input beam. In this case the input beam must be have a large bandwidth such that the difference in frequencies contained within the beam are large enough to propagate. When this is true I_1 and I_2 can be thought of as different frequency components of the same beam. It can also be seen in Eq. (2.32) that the phase mismatch, described by Δk, is completely confined to the last sinc term. This phase mismatch can be thought of as an efficiency multiplier which physically limits the interaction length of the process. As can be seen in Fig. 2.1 which shows the phase mismatch term plotted as a function of efficiency, $\sin c^2\left(\frac{\Delta kL}{2}\right)$, the most efficient generation occurs when $\frac{\Delta kL}{2} = 0$. This can only be true when either Δk or L is zero, and since the non-linear interaction material thickness is required to be non-zero by definition Δk must therefore be zero to obtain a perfectly phase matched condition. Remembering the definition of $\Delta k = k_1 - k_2 - k_3$, it is often difficult to obtain perfect phase matching in any physical process, because the refractive index of materials generally increases as a function of frequency. For $\Delta k = 0$ to be true the following must also,

$$k_3 = k_1 - k_2 \tag{2.33}$$

which can also be expressed as,

$$n_3\omega_3 = n_1\omega_1 - n_2\omega_2, \tag{2.34}$$

where $\omega_3 \ll \omega_2 < \omega_1$ and therefore,

$$n_3 - n_2 = \frac{(n_1 - n_2)\omega_1}{\omega_3}. \tag{2.35}$$

Notice for materials that display normal dispersion $n_3 \gg n_2$ and so the left hand side must be negative, however $n_1 > n_2$ and so the right hand side must be positive. In the absence of negative angular frequencies Eq. (2.35) therefore implies that perfect phase matching cannot occur in materials which have normal dispersion around the frequency region of the interaction. It is however possible to obtain phase matching using Eq. (2.35) in materials that display anomalous phase matching, that is to say the refractive index decreases as a function of frequency. Another common way to obtain phase matching is to make use of the birefringence of a material, which enables electric fields polarised along different crystal axes to experience different refractive indices [2].

This condition adds a new limit onto the type of material that can be used for the generation of terahertz radiation within non-linear optical crystals; as well as having a strong $\chi^{(2)}$ term the crystal must also be birefringent such that it is possible to obtain phase matching between the pump laser and terahertz radiation.

2.3.1.1 Generation Within Zinc Telluride

Within this section an example of terahertz generation using a femtosecond laser within a zinc telluride (ZnTe) crystal is presented [4]. For this case the second order non-linear polarisation term can be re-written in the frequency domain as,

$$P_i^{(2)}(\Omega) = \sum_{j,k} \epsilon_0 \chi_{ijk}^{(2)} E_i(\omega) E_k^*(\Omega - \omega), \tag{2.36}$$

where Ω is the frequency of the generated wave and ω is the optical frequency. The indices ijk represent axes that lie along a Cartesian axis grid in the frame of the crystal. If Kleinman symmetry holds, which states that if the frequencies involved are much smaller than the lowest resonance frequency of the material system then the nonlinear susceptibility tensor is no longer dependent on frequency, then the indices must also be permutable [2]. Such a symmetry condition is true for the generation of terahertz radiation within ZnTe and so contracted notation can be used to help simplify the form of Eq. (2.36). Contracted notation invokes a new index l which combines the two last indices jk into a single index [2, 4]. The relation between l and jk can be seen in Table 2.1.

This then enables $\chi_{ijk}^{(2)}$ to be redefined as d_{il} where,

$$d_{il} = \frac{1}{2}\chi_{ijk}^{(2)}, \tag{2.37}$$

Table 2.1 Conversion between standard and contracted notation [2]

jk	11	22	33	23,32	31,13	12,21
l	1	2	3	4	5	6

and enables d_{il} to be expressed as a 3×6 matrix:

$$d_{il} = \begin{bmatrix} d_{11} & d_{12} & d_{13} & d_{14} & d_{15} & d_{16} \\ d_{21} & d_{22} & d_{23} & d_{24} & d_{25} & d_{26} \\ d_{31} & d_{32} & d_{33} & d_{34} & d_{35} & d_{36} \end{bmatrix}. \tag{2.38}$$

The generation of the polarisation term can now be written as,

$$\begin{bmatrix} P_x \\ P_y \\ P_z \end{bmatrix} = 2\epsilon_0 \begin{bmatrix} d_{11} & d_{12} & d_{13} & d_{14} & d_{15} & d_{16} \\ d_{21} & d_{22} & d_{23} & d_{24} & d_{25} & d_{26} \\ d_{31} & d_{32} & d_{33} & d_{34} & d_{35} & d_{36} \end{bmatrix} \times \begin{bmatrix} E_x E_x^* \\ E_y E_y^* \\ E_z E_z^* \\ 2E_y E_z^* \\ 2E_z E_x^* \\ 2E_x E_y^* \end{bmatrix}. \tag{2.39}$$

ZnTe is a crystal which exists within the $\bar{4}3m$ point group. This defines the symmetries which exist within the crystal structure and enables the d_{il} tensor to be simplified to,

$$d_{il} = \begin{bmatrix} 0 & 0 & 0 & d_{14} & 0 & 0 \\ 0 & 0 & 0 & 0 & d_{25} & 0 \\ 0 & 0 & 0 & 0 & 0 & d_{36} \end{bmatrix}, \tag{2.40}$$

where $d_{14} = d_{25} = d_{36}$. The electric field of the pump laser can be defined as,

$$E = E_0 \begin{bmatrix} \sin(\theta)\cos(\phi) \\ \sin(\theta)\sin(\theta) \\ \cos(\theta) \end{bmatrix}, \tag{2.41}$$

where θ is the polar angle and ϕ is the azimuthal angle and using these definitions and simplifications Eq. (2.36) now becomes,

$$\begin{bmatrix} P_x \\ P_y \\ P_z \end{bmatrix} = 2\epsilon_0 d_{14} E_0^2 \begin{bmatrix} 0 & 0 & 0 & 1 & 0 & 0 \\ 0 & 0 & 0 & 0 & 1 & 0 \\ 0 & 0 & 0 & 0 & 0 & 1 \end{bmatrix} \times \begin{bmatrix} \sin^2(\theta)\cos^2(\phi) \\ \sin^2(\theta)\sin^2(\phi) \\ \cos^2(\theta) \\ 2\sin(\theta)\cos(\theta)\sin(\phi) \\ 2\sin(\theta)\cos(\theta)\cos(\phi) \\ 2\sin^2(\theta)\sin(\phi)\cos(\phi) \end{bmatrix}, \tag{2.42}$$

which when simplified gives,

$$\begin{bmatrix} P_x \\ P_y \\ P_z \end{bmatrix} = 4\epsilon_0 d_{14} E_0^2 \sin(\theta) \begin{bmatrix} \cos(\theta)\sin(\phi) \\ \cos(\theta)\sin(\phi) \\ \sin(\theta)\sin(\phi)\cos(\phi) \end{bmatrix}. \tag{2.43}$$

As in Sect. 2.3.1 it is now common to express this in terms of an intensity. Using the same definition as given by Eq. (2.30) this now becomes,

$$I = \frac{2nc\epsilon_0^2 d_{41}^2 E_0^4 \sin^2(\theta)}{\pi} \left[4\cos^2(\theta) + \sin^2(\theta)\sin^2(2\phi)\right]. \tag{2.44}$$

Noticing that the only component of Eq. (2.44) that contains a ϕ dependence is the $\sin^2(2\phi)$ term it is clear that the intensity of the generated terahertz wave is maximised when this term is maximised. This is true when $\phi = n\frac{\pi}{4}$ where n is an odd integer, as can be seen from . Setting ϕ to $\frac{\pi}{4}$ enables Eq. (2.44) to be written such that it only depends upon θ,

$$I = \frac{2nc\epsilon_0^2 d_{41}^2 E_0^4}{\pi} \sin^2(\theta)\left[4 - 3\sin^2(\theta)\right]. \tag{2.45}$$

Given that θ is the polar angle, that being the angle between the [110] crystal axis and the laser polarisation, it can be seen from Eq. (2.45) and Fig. 2.3 the generated intensity is maximised when $\theta = 54°$. Therefore optimal terahertz generation will occur when the pump beam is polarised at 54° to the [110] crystal edge when incident upon the $(\overline{1}10)$ crystal surface. This can be said to be true for any crystal that has the same crystal symmetries as ZnTe, such as gallium phosphide (GaP). However for crystals that exhibit different symmetry properties, such as lithium niobate ($LiNbO_3$) this expression can change drastically. These different forms will be discussed in further chapters when relevant (Fig. 2.2).

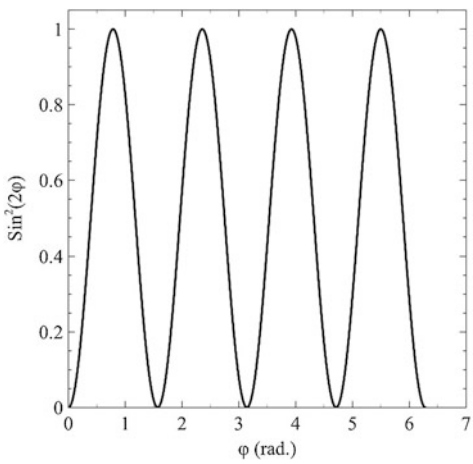

Fig. 2.2 Plot showing the generated terahertz dependence on the angle ϕ

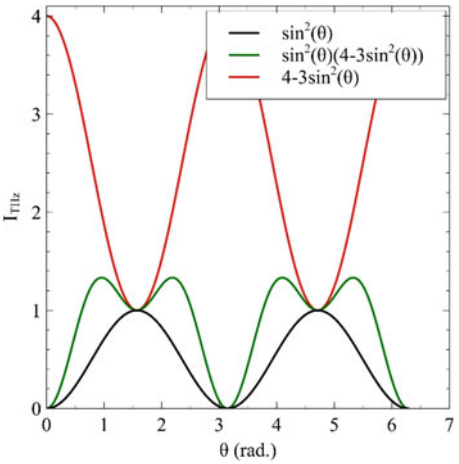

Fig. 2.3 Generated terahertz intensity as a function of the polar angle, θ

2.3.1.2 Generation Within Magnesium-Oxide-Doped Stoichiometric Lithium Niobate

Generation of terahertz radiation within magnesium-oxide-doped stoichiometric lithium niobate (MgO:SLN) differs from generation within ZnTe and GaP due to the different crystal properties, specifically symmetries. To investigate the generation within MgO:SLN it is possible to start with,

$$\begin{bmatrix} P_x \\ P_y \\ P_z \end{bmatrix} = 2\epsilon_0 \begin{bmatrix} d_{11} & d_{12} & d_{13} & d_{14} & d_{15} & d_{16} \\ d_{21} & d_{22} & d_{23} & d_{24} & d_{25} & d_{26} \\ d_{31} & d_{32} & d_{33} & d_{34} & d_{35} & d_{36} \end{bmatrix} \times \begin{bmatrix} E_x E_x^* \\ E_y E_y^* \\ E_z E_z^* \\ 2E_y E_z^* \\ 2E_z E_x^* \\ 2E_x E_y^* \end{bmatrix}, \tag{2.46}$$

to which the relevant crystal symmetries are applied. MgO:SLN has a 3 m crystal symmetry which means the d_{il} matrix can be expressed as,

$$d_{il} = \begin{bmatrix} 0 & 0 & 0 & 0 & d_{31} & d_{21} \\ d_{21} & -d_{21} & 0 & d_{31} & 0 & 0 \\ d_{31} & d_{31} & d_{33} & 0 & 0 & 0 \end{bmatrix}. \tag{2.47}$$

Experimental measurements of the non-zero values d_{21}, d_{31} and d_{33} have shown that d_{33} is much larger than d_{21} and d_{31} [2]. It is therefore possible to further simplify Eq. (2.47) by setting both $d_{21} \approx 0$ and $d_{31} \approx 0$, leaving,

$$d_{il} = \begin{bmatrix} 0 & 0 & 0 & 0 & 0 & 0 \\ 0 & 0 & 0 & 0 & 0 & 0 \\ 0 & 0 & d_{33} & 0 & 0 & 0 \end{bmatrix}. \tag{2.48}$$

Then, by using Eq. (2.48) and placing it into Eq. (2.46) it is possible to arrive at

$$\begin{bmatrix} P_x \\ P_y \\ P_z \end{bmatrix} = 2\epsilon_0 \begin{bmatrix} 0 & 0 & 0 & 0 & 0 & 0 \\ 0 & 0 & 0 & 0 & 0 & 0 \\ 0 & 0 & d_{33} & 0 & 0 & 0 \end{bmatrix} \times \begin{bmatrix} E_x E_x^* \\ E_y E_y^* \\ E_z E_z^* \\ 2E_y E_z^* \\ 2E_z E_x^* \\ 2E_x E_y^* \end{bmatrix}, \tag{2.49}$$

which when simplified gives,

$$\begin{bmatrix} P_x \\ P_y \\ P_z \end{bmatrix} = 2\epsilon_0 d_{33} \begin{bmatrix} 0 \\ 0 \\ E_z E_z^* \end{bmatrix}. \tag{2.50}$$

This is an important result as it states that in order to generate terahertz radiation the input beams must be linearly polarised along the z axis. It also states that any generated terahertz radiation will also be polarised along the same z axis.

The above result, Eq. (2.50), provides information regarding the required polarisation of the pump laser as well as the polarisation of the generated 2nd order polarisation term, $\overline{P}$. To investigate how this polarisation term forms a propagating wave the refractive indices at both the optical pump wavelength and the generated terahertz radiation wavelength must be obtained in order to perform a phase-matching calculation. The refractive index of MgO:SLN at 800 nm is 2.25 and at 0.1 mm is 4.96. The large difference in refractive indices means that the generated non-linear polarisation produces radiation which coherently adds to form a Cherenkov cone which trails the optical pump [5]. The angle of this cone defined as θ in Fig. 2.4 can be expressed as a function of the generated terahertz radiation refractive index and the optical pump refractive index through

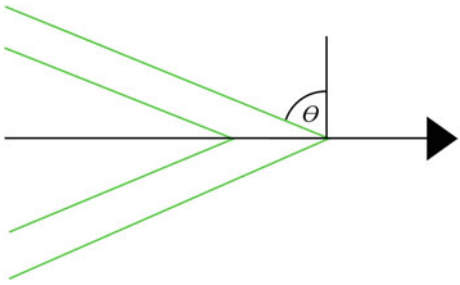

Fig. 2.4 Cherenkov cone formed inside MgO:SLN by an 800 nm laser beam (*black*). *Green lines* represent the generated wave fronts of the terahertz radiation at an angle of θ to the wave fronts of the optical generation beam (color figure online)

$$\tan(\theta) = -\frac{n_{THz}}{n_{opt}}\omega\frac{d\Theta}{d\omega}, \tag{2.51}$$

where n_{THz} is the terahertz refractive index of 4.96, n_{opt} is the optical refractive index of 2.25, θ is the angle of tilt and $\frac{d\Theta}{d\omega}$ represents the angular dispersion. This expression can be expressed solely as a function of the two refractive indices as,

$$\theta = \cos^{-1}\left(\frac{n_{opt}}{n_{THz}}\right). \tag{2.52}$$

When combined with the correct refractive index values a Cherenkov cone angle of 63.02° is obtained [6]. In order to obtain efficient and scalable generation the pulse front of the pump laser should be matched to this angle so that the generated radiation coherently adds to form a propagating pulse. This feature is known as a pulse front tilt (PFT) and is commonly produced via grating—imaging optical systems. When radiation undergoes dispersion, such as when it is incident upon a grating, different wavelengths travel different paths. This spectral dispersion means that the radiation rapidly becomes larger as the different spectral components become spatially separated. However in the near field of such a dispersive medium, whilst all components of the radiation are spatially overlapped, the difference in path length travelled by each spectral component gives rise to a propagating beam with a wave front that is tilted at a non-orthogonal angle to the propagation direction. An imaging system can then be used to image the plane at which the tilt exists to another more distant plane, thus providing a far field pulse front tilt, as can be seen in Fig. 2.5.

Equation (2.52) describes the tilt required inside the MgO:SLN for optimal generation to occur; however the actual tilt is generated externally by a lens and grating combination. Due to the effective length changes of the generation radiation caused by the refractive index of the material and any magnification caused by the imaging system the tilt generated externally will be different to the internal tilt. The pulse front tilt generated by a grating can be expressed as,

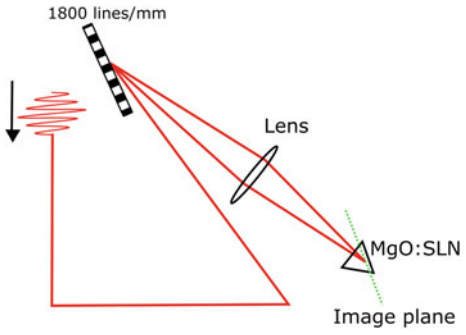

Fig. 2.5 Schematic diagram showing the collection and transport of optical radiation with a pulse-front-tilt from a grating to the image plane situated within a MgO:SLN crystal (color figure online)

$$\theta_g = \tan^{-1}\left(\frac{m\lambda}{d\ \cos(\phi)}\right). \tag{2.53}$$

In Eq. (2.53) θ_g represents the tilt generated by the grating, m is the diffraction order, λ is the wavelength of the optical pump, d is the number of groves per mm on the grating and ϕ is the diffraction angle which describes the angle at which the output radiation leaves the grating. Using geometry it is possible to convert the tilt angle required inside the crystal to an external tilt angle, which is the angle that would need to be generated by the grating. This conversion takes the form,

$$\tan(\theta_g) = n_{opt}\beta\ \tan(\theta), \tag{2.54}$$

where n is the refractive index of the material and β is the magnification of the pump beam induced by the imaging system. Therefore by combing Eq. (2.53) and Eq. (2.54) it is possible to express the required internal tilt as a function of optical system parameters,

$$\theta = \tan^{-1}\left[\frac{1}{n_{opt}\beta}\left(\frac{m\lambda}{d\ \cos(\phi)}\right)\right]. \tag{2.55}$$

As the required internal tilt is fixed at approximately 63° it is now possible to design an optical system that will provide the required tilt.

This tilt geometry dictates the physical shape of the crystal as the input surface is required to be perpendicular to the optical input beam and the output surface is required to be perpendicular to the generated terahertz radiation so as to reduce reflections in both cases. The geometry of the crystal can be seen in Fig. 2.6; here the red line denotes the optical input radiation and the green lines represent the generated radiation output. Angles θ_g and θ represent the external and internal angles respectively. In Fig. 2.6 the z-axis of the crystal is orientated perpendicular to the page and thus according to Eq. (2.50) the polarisation of both beams is required to be orientated along the same axis.

The terahertz radiation that is generated along the output surface of the $LiNbO_3$ is not produced with a uniform profile. This is due to three properties of the

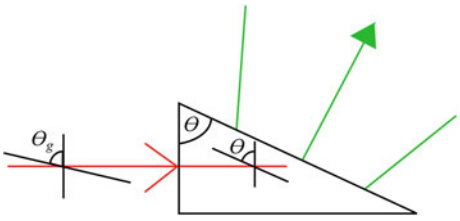

Fig. 2.6 Required geometrical shape of the MgO:SLN crystal, the *red line* denotes the optical pump beam, the *green lines* denote the generated terahertz radiation. The angle θ represents the internal tilt angle and angle θ_g represents the external tilt angle (color figure online)

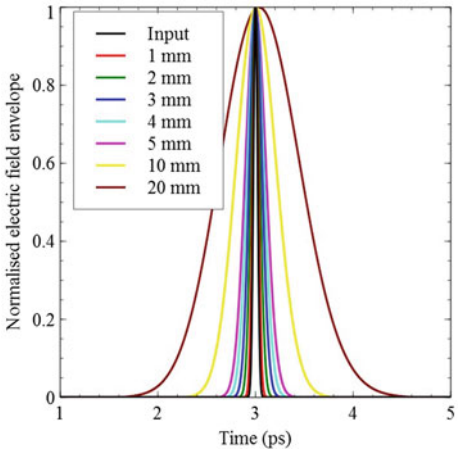

Fig. 2.7 Simulation showing the temporal dispersion induced onto an 800 nm optical pump laser passing through various thicknesses of MgO:SLN crystal

generation technique, firstly the spatial profile of the pump beam which typically does not have a uniform intensity profile. The second property relates to the geometry of the generation system. As can be seen from Fig. 2.6 different parts of the pump beam travel through different lengths of the $LiNbO_3$ crystal, therefore experiencing a different effective crystal length. The third factor which affects the terahertz profile on the output surface relates to the dispersion of the pump beam within the $LiNbO_3$ crystal. As $LiNbO_3$ is a highly dispersive medium within the 800 nm wavelength range and due to the spatially varying effective crystal thickness the pump beam has a transversely varying temporal profile. The effects of the dispersion on the temporal profile of the pump laser can been seen in Figs. 2.7 and 2.8. The FWHM values of the temporal profile in Fig. 2.8 is found by first fitting a Gaussian to the temporal profile and then using the FWHM value given from the Gaussian equation. This can cause errors if the pump profile does not have a

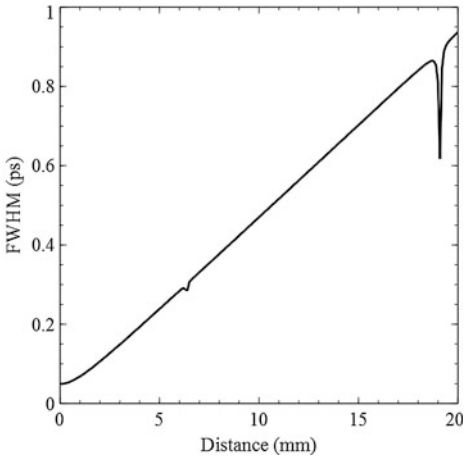

Fig. 2.8 Simulated FWHM temporal duration of a 50 fs input laser of wavelength 800 nm as a function of propagation distance through MgO:SLN

Gaussian shape. These errors manifest within Fig. 2.8 at around 6 and 19 mm and can be seen as the sharp negative peaks. Here a 50 fs 800 nm pulse is propagated through varying thicknesses of MgO:SLN. As can be seen the pulse width is broadened in time with the FWHM approaching 1 ps after 20 mm propagation. This can have a big effect on the generation efficiency as one side of the pulse will only propagate through less than 1 mm of MgO:SLN whereas the other side of the pulse could travel through up to 5 mm of MgO:SLN.

2.4 Terahertz Detection

Terahertz detection is typically more difficult than the detection of optical radiation. This is mainly due to the low photon energy of terahertz radiation. This low photon energy makes standard semiconductor-based detectors impractical as they rely on the photo-excitation of charge carriers from the valence band into the conduction band. This requires the energy of the photon to be greater than the band gap of the semiconductor and currently semiconductors used in detectors have band gaps larger than the terahertz photon energy. Due to this other forms of detection are required. These other forms typically fall into two categories, thermal and electro-optic. Within this section both of these detection forms are explained and investigated including their positive and negative attributes and typical uses.

2.4.1 Thermal Terahertz Detectors

Thermal detectors, as the name suggests, rely on the thermal properties of a material to detect radiation. When radiation is absorbed by a material energy is transferred from the radiation to the material, and as the material receives energy it heats up. Whilst thermal detectors are able to detect radiation in the terahertz frequency range they do have limitations. These limitations typically include high background noise, as they are sensitive to thermal radiation and a change in the surrounding temperature will cause a change in the background level. Also all forms of radiation transfer thermal energy to the detector and therefore all radiation absorbed by the detector contributes towards the outputted signal. The response times of thermal detectors is also typically very slow, on the μs time scales. This makes them impractical for applications that use ultrafast terahertz pulses, on the 100's fs timescale, to perform measurements that require good time resolution. These applications include terahertz waveform analysis and pump-probe style spectroscopic experiments. Due to their workings these detectors tend to be large in spatial size and thus are not suitable for experiments that require good spatial resolution;

however this aspect has seen progress with the advent of micro-bolometer arrays. These micro-bolometer arrays have been shown to produce terahertz images with spatial resolutions down to 50 μm [7]. There are three common thermal terahertz detectors which are the bolometer, Golay cell and pyro electric detectors.

2.4.1.1 Bolometer

A bolometer is a device which measures the power of incident radiation via the thermal transfer of energy to a material which has a temperature dependent electric resistance. Typically bolometers consist of an absorbing material, a transfer material and a thermal reservoir. Radiation is incident upon the absorbing material causing it to absorb energy from the radiation and heat up. This material is attached to the thermal reservoir via the transfer material. The thermal reservoir is kept at a constant low temperature. Therefore as the absorbing material heats up a temperature difference between the absorbing material and thermal reservoir is formed and heat energy therefore flows through the transfer material towards to thermal reservoir forming a thermal equilibrium. The transfer material therefore experiences a time dependent thermal change. The transfer material is typically chosen such that its resistance is highly dependent upon temperature. Therefore this temporally dependent thermal change is measured by monitoring the resistance of the transfer material.

To make the bolometer sensitive the temperature of the thermal reservoir must be kept cold and constant. Such bolometers are typically contained within a cooling chamber which contains liquid helium or liquid nitrogen. This typically limits their response time to the μs range as it is limited by the flow of thermal energy from the absorber to the thermal reservoir. They can however be extremely sensitive with commercially available units able to detect less than 1 nJ per of terahertz pulse energy. This makes bolometers the most sensitive type of thermal detectors for terahertz radiation [8, 9].

2.4.1.2 Golay Cell

A Golay cell is a thermal detector that uses the expansion and contraction of a material due to its temperature change. Typically it consists of a gas-filled enclosure with an absorbing material inside. As the absorbing material receives energy from the incident radiation it heats up, and this thermal energy is then dissipated to the surrounding gas. As the gas heats up it expands causing a membrane in the wall of the enclosure to expand and contact. This expansion and contraction is then detected either using an audio detector such as a microphone or a laser which monitors the surface position. The response time of a Golay cell is typically on the order of 10's of ms and is one of the slowest thermal detectors. However it is still sensitive and able to detect terahertz radiation with pulse energies down to the nJ

level. The sensitivity of a Golay cell is also not strongly dependent upon frequency, thus giving the Golay cell a very flat response over a broad range of frequencies. This makes the Golay cell good when trying to accurately calculate the pulse energy of an ultrafast broadband terahertz pulse [10].

2.4.1.3 Pyroelectric Detector

Pyroelectric detectors are the third type of commonly used thermal detector. They generally consist of a crystalline lithium tantalate material (CLT), an absorbing material and a set of electrodes. The radiation falls onto the absorbing material which converts the radiation energy into thermal energy. This thermal energy is then transferred onto the CLT. Crystalline lithium tantalate is a ferroelectric material and thus exhibits spontaneous electrical polarisation when below the Curie temperature. When the temperature of the CLT is altered the electrical polarisation rotates. Therefore by using electrodes to read of the electrical polarisation only in one axis the temperature change can be monitored. As the temperature change is as a direct result of the incident radiation heating up the absorbing material the signal produced by the electrodes is directly proportional to the incident radiation power. Again as with the other thermal detectors pyroelectric detectors have slow response times on the 100's μs timescale. However they do have a flat response to frequency which is only limited by the absorbing material. They are also able to be made into very small devices, on the 100's μm scale, providing the ability for good spatial resolution [11].

2.4.2 Electro-Optic Detection

Electro-optic detection is a common form of terahertz radiation detection. It involves mixing a near-infrared (NIR) laser with the terahertz radiation inside a non-linear optical material. The same, but reverse, non-linear physical process as used in the non-linear optical generation of terahertz radiation then causes information contained within the terahertz radiation to be transferred into the NIR laser pulse. This can then be detected using standard semiconductor style detectors.

The physics involved in transferring information from the terahertz electric field into the optical detection laser is the same as is involved in the optical generation of terahertz radiation as described in Sect. 2.3.1. Commonly-used detection crystals are ZnTe and GaP both of which display the same crystal structure and symmetry components [12]. For electro-optic detection however it is easier to think of the terahertz radiation as changing the relative permittivity of the material, effectively changing the refractive index of the material. The optical probe beam will therefore experience this change in refractive index and propagate accordingly [13–16].

The electric displacement vector can be linked to the electric field via

$$\begin{bmatrix} D_x \\ D_y \\ D_z \end{bmatrix} = \epsilon_0 \begin{bmatrix} \epsilon_x & 0 & 0 \\ 0 & \epsilon_y & 0 \\ 0 & 0 & \epsilon_z \end{bmatrix} \begin{bmatrix} E_x \\ E_y \\ E_z \end{bmatrix}, \tag{2.56}$$

where ϵ_n represents the square root of the refractive index along the axis n. In the case of a homogeneous material, where no birefringence is present, $\epsilon_x = \epsilon_y = \epsilon_z$. However for cases where birefringence is present $\epsilon_x \neq \epsilon_y \neq \epsilon_z$ can be true. To define a surface of constant energy density, the energy density must first be defined as $u = \frac{1}{2}\overline{E}\,\overline{D}$ [17]. Using this definition and Eq. (2.56) it is then possible to define such a surface as

$$\epsilon_0 u = \frac{D_x^2}{\epsilon_x} + \frac{D_y^2}{\epsilon_y} + \frac{D_z^2}{\epsilon_z}. \tag{2.57}$$

It is now clear that for a non-birefringent material the surface of constant energy density would take the form of a sphere and for a birefringent material it would take the form of an ellipse. Using the standard relationship between refractive index and ϵ_n, $n_n = \sqrt{\epsilon_n}$, and by defining a dimensionless vector along the direction of $\overline{D}$, $\overline{s} = \frac{\overline{D}}{\sqrt{2\epsilon_0 u}}$ it is possible to obtain the equation of the refractive index ellipsoid,

$$\frac{s_x^2}{n_x^2} + \frac{s_y^2}{n_y^2} + \frac{s_z^2}{n_y^2} = 1. \tag{2.58}$$

Now by defining a new tensor which is known as the impermeability tensor, $\overline{\overline{n}}$,

$$\overline{\overline{n}} = \overline{\epsilon}^{-1}, \tag{2.59}$$

the previous refractive index ellipsoid equation, Eq. (2.58), becomes,

$$\overline{s}\overline{\overline{n}}\overline{s} = 1. \tag{2.60}$$

Now these results can be taken and applied to a practical application such as terahertz detection in ZnTe with a 50 fs 800 nm laser beam. ZnTe has a cubic lattice structure and is isotropic. This means the impermeability tensor can be replaced by by the scalar quantity $\epsilon^{-1}\overline{I}$, where $\overline{I}$ is the identity matrix. When terahertz radiation is incident upon the ZnTe crystal the impermeability tensor becomes,

$$\overline{\overline{n}}(E_T) = \epsilon^{-1}\overline{I} + \chi^{(2)}\overline{E}_t. \tag{2.61}$$

This now converts the ellipsoid equation, Eq. (2.60), into an ellipsoid equation which depends upon the applied terahertz electric field,

$$\overline{\overline{sns}} = \sum_{i,j=x,y} \left(\epsilon^{-1} \delta_{ij} + \sum_{k=z} r_{ijk} E_{T,k} \right) s_x s_y = 1. \tag{2.62}$$

It is now possible to express this in contracted notation as previously explained in Sect. 2.3.1 and the same symmetries used for generation can be applied such that only one independent value of r_{ijk}, $r_{il} = r_{41} = r_{52} = r_{63}$, is present. This therefore enables the refractive index ellipsoid equation to be rewritten as,

$$\frac{1}{n_0^2}\left(s_x^2 + s_y^2 + s_z^2\right) + 2r_{41}\left(E_{T,x}s_y s_z + E_{T,y}s_x s_z + E_{T,z}s_x s_y\right) = 1. \tag{2.63}$$

This equation can now be transformed into the crystal axis frame. Typically ZnTe is cut in the (110) plane with both the terahertz radiation and optical probe radiation propagating perpendicular to this plane with their electric field vectors in the (110) plane. Defining a new co-ordinate system (l, m, n) with l lying along the $[\overline{1}10]$ direction and m lying along the [001] direction and allowing the terahertz radiation electric field vector to rotate around the l axis at an angle of α it is possible to express the terahertz electric field vector, $\overline{E}_T$ as,

$$\overline{E}_T = E_T \begin{bmatrix} -\cos\left(\frac{\alpha}{\sqrt{2}}\right) \\ \cos\left(\frac{\alpha}{\sqrt{2}}\right) \\ \sin(\alpha) \end{bmatrix} \tag{2.64}$$

In this geometrical setup with the ZnTe limitations applied this now leaves the refractive index ellipsoid equation as

$$\overline{sn}(E_T)\overline{s} = 1, \tag{2.65}$$

and the impermeability tensor as

$$\begin{aligned} \overline{n}(E_T) = \frac{1}{n_0^2} \begin{pmatrix} 1 & 0 & 0 \\ 0 & 1 & 0 \\ 0 & 0 & 1 \end{pmatrix} \ldots \\ + r_{41} E_T \begin{pmatrix} 0 & \sin(\alpha) & \cos\left(\frac{\alpha}{\sqrt{2}}\right) \\ \sin(\alpha) & 0 & -\cos\left(\frac{\alpha}{\sqrt{2}}\right) \\ \cos\left(\frac{\alpha}{\sqrt{2}}\right) & -\cos\left(\frac{\alpha}{\sqrt{2}}\right) & 0 \end{pmatrix}. \end{aligned} \tag{2.66}$$

The refractive index along each of the (x, y, z) axes can now be calculated using $n_n = 1/\sqrt{\lambda_n}$, where λ_n is the eigenvector which lies along either x, y or z. To calculate the eigenvectors first the eigenvalues must be calculated which are

$$\lambda_{x,y} = \frac{1}{n_0^2} - \frac{r_{41}E_T}{2}\left(\sin(\alpha) \pm \sqrt{1+3\cos^2(\alpha)}\right), \tag{2.67}$$

$$\lambda_z = \frac{1}{n_0^2} + r_{41}E_T \sin(\alpha). \tag{2.68}$$

From these the normalised eigenvectors are

$$S_{x,y} = \frac{1}{2}\sqrt{1 \pm \frac{\sin(\alpha)}{\sqrt{1+3\cos^2(\alpha)}}}\begin{bmatrix} \pm 1 \\ \mp 1 \\ \frac{2\sqrt{2}\cos(\alpha)}{\sqrt{1+3\cos^2(\alpha)+\sin(\alpha)}} \end{bmatrix}, \tag{2.69}$$

$$S_z = \frac{1}{\sqrt{2}}\begin{bmatrix} 1 \\ -1 \\ 0 \end{bmatrix}. \tag{2.70}$$

The refractive indices along each axis as a function of incident terahertz field strength are therefore,

$$n_x = n_0 + \frac{n_0^3 r_{41}E_T}{4}\left(\sin(\alpha) + \sqrt{1+3\cos^2(\alpha)}\right), \tag{2.71}$$

$$n_y = n_0 + \frac{n_0^3 r_{41}E_T}{4}\left(\sin(\alpha) - \sqrt{1+3\cos^2(\alpha)}\right), \tag{2.72}$$

$$n_z = n_0 - \frac{n_0^3 r_{41}E_T}{2}\sin(\alpha). \tag{2.73}$$

These refractive indices can be seen plotted in both the principal frame and the crystal frame in Fig. 2.9. Here both the terahertz and optical detection radiation propagate into the picture perpendicularly to both the [001] and [–110] axes. This direction has previously been denoted $S_z = \left(-\frac{1}{\sqrt{2}}, -\frac{1}{\sqrt{2}}, 0\right)$. The electric field

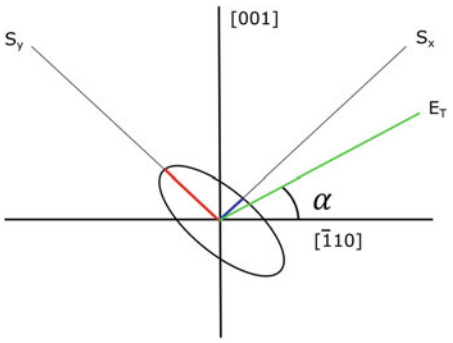

Fig. 2.9 Refractive index ellipsoid in both the crystal frame and the principal frame. n_x (*blue*) and n_y (*red*) are shown as well as the polarisation (*green*) of the applied terahertz field

vector of the optical detection radiation is fixed along the $[\bar{1}10]$ axis whilst the electric field vector of the terahertz is allowed to rotate azimuthally around [110]. The angle the terahertz electric field vector makes with the [–110] axis is denoted α in Fig. 2.9.

Taking all of the above described geometry into account the optical probe electric field experiences a phase change due to the difference in the two refractive indices, n_x and n_y of Γ, where,

$$\Gamma = \frac{\omega_o L}{c}\left(n_x - n_y\right), \tag{2.74}$$

where L is the crystal thickness and ω_o is the optical probe electric field angular frequency. Combining Eq. (2.74) with the refractive index equations described in Eqs. (2.71) and (2.72), it is possible to express the relative phase shift experienced by the optical probe as a function of applied terahertz electric field strength [18] as

$$\Gamma = \frac{\pi d}{\lambda_0} n_0^3 r_{41} E_T \sqrt{1 + 3\cos^2(\alpha)}. \tag{2.75}$$

The dependence of the relative phase shift experienced by the optical probe on the angle of the terahertz electric field orientation can be seen in Fig. 2.10. As can be seen from this figure the relative phase shift is maximised when the terahertz electric field is orientated with an α angle of 0°. This means that the maximum detectable signal will be obtained when both the optical detection electric field and the terahertz electric field are aligned with the $[\bar{1}10]$ axis.

Whilst the above describes how the optical probe is changed inside the detection crystal the information that can be extracted depends upon how the change in the

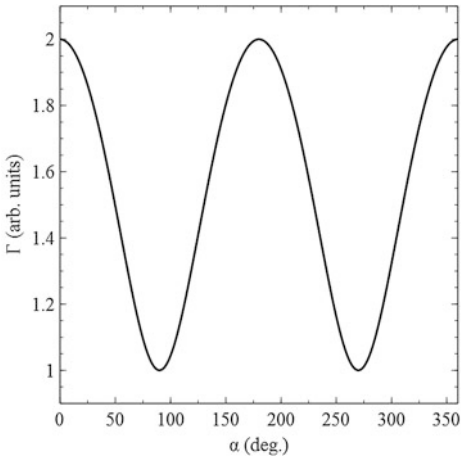

Fig. 2.10 Measured phase shift of an optical probe beam within a ZnTe detection crystal due to the presence of terahertz radiation as a function of the $[\bar{1}10]$ crystal angle α

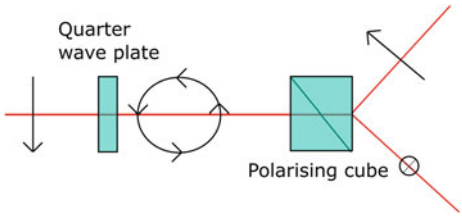

Fig. 2.11 Schematic diagram of the optical scheme for balanced detection, showing the linearly polarised input beam being converted into a circularly polarised beam and then two orthogonal linearly polarised beams

optical electric field is detected. Typically there are two main types of probe detection each enabling a different type of information regarding the terahertz field to be obtained. These two methods are balanced detection, cross-polarised detection.

2.4.2.1 Balanced Detection

Balanced detection uses a quarter wave plate, a polarising beam cube and a set of two photodiodes to convert the phase change experienced by the optical probe electric field into a difference in polarisation state. Each polarisation state is then detected by a separate photodiode. This can be seen in Fig. 2.11, where the optical probe is shown in red with the polarisation states shown in black at each part of the optical setup.

To analyse how the phase change converts to a detectable signal, Jones matrices are used to propagate the electric field through the optical components used [19]. By setting α to 0°, such that ZnTe crystal is orientated with its (110) surface aligned to the polarisation of the terahertz radiation and the optical probe laser the Jones matrix calculation for balanced detection becomes

$$\overline{E}_{out} = \overline{R}(-\phi)\overline{M}_w\overline{R}(\phi)\overline{R}(-\theta)\overline{M}_\Gamma\overline{R}(\theta)\overline{E}_{in}, \tag{2.76}$$

where $\overline{E}_{out}$ is the vector, $\begin{pmatrix} E_{x,out} \\ E_{y,out} \end{pmatrix}$, representing the output of the system, $\overline{R}(\theta)$ is a rotation matrix equal to $\begin{pmatrix} \cos(\theta) & -\sin(\theta) \\ \sin(\theta) & \cos(\theta) \end{pmatrix}$, $\overline{M}_w$ is the quarter wave plate matrix equal to $\begin{pmatrix} e^{\frac{i\pi}{4}} & 0 \\ 0 & e^{-\frac{i\pi}{4}} \end{pmatrix}$, $\overline{M}_\Gamma$ is the matrix which represents the phase rotation induced by the terahertz electric field and is equal to $\begin{pmatrix} e^{i\Gamma} & 0 \\ 0 & e^{-i\Gamma} \end{pmatrix}$ and $\overline{E}_{in}$ is the input optical detection electric field vector. The measured signal, $\Delta I/I_0$, output by a

lock-in amplifier is a measure of $\left|E_{x,out}\right|^2 - \left|E_{y,out}\right|^2$. This now allows for the measured signal to be expressed as a function of the phase rotation induced by the terahertz radiation such:

$$S = \frac{\Delta I}{I_0} = \sin(\Gamma). \tag{2.77}$$

Applying the small angle approximation and using Eq. (2.75) the following equation can be written

$$E_{THz} = \frac{\Delta I}{I_0} \frac{\lambda}{2\pi n^3 r_{41} L}, \tag{2.78}$$

where λ is the optical detection optical field wavelength, ΔI represents the change in the photodiode signals as measured by the lock-in amplifier, I_0 is 2 times the photodiode level with no terahertz radiation present (again as measured by the lock-in amplifier), n is the refractive index of the optical detection radiation inside the detection crystal, r_{41} is the electro-optic co-efficient of the detection crystal and L is the crystal thickness. Equation (2.78) represents the terahertz electric field strength inside the detection crystal. Additional factors can be added to account for losses in the terahertz radiation due to reflections and losses as well as calibration factors to account for errors in devices used. Adding these factors in (2.78) gives,

$$E_{THz} = \frac{\Delta I}{I_0} \frac{\lambda}{2\pi n^3 r_{41} L} TC, \tag{2.79}$$

where T represents the transmission coefficient of the detection material and C represents correction factors applied to account for errors in any measuring devices. This equation, Eq. (2.79), now describes the terahertz electric field strength external to the detection crystal as measured by balanced detection [20].

2.4.2.2 Crossed-Polarised Detection

Crossed-polarised detection uses similar optics to the previously described balanced detection, however the quarter wave plate is replaced with a half wave plate. The half wave plate is set such that in the absence of terahertz radiation the probe beam is linearly polarised such that it exits the polarising prism through one of its arms. This can be described by the following Jones Matrix calculation,

$$\overline{E}_{out} = \overline{R}(-\phi)\overline{M}_w\overline{R}(\phi)\overline{R}(-\theta)\overline{M}_\Gamma\overline{R}(\theta)\overline{E}_{in}, \tag{2.80}$$

where all the elements are the same as for balanced detection apart from M_w which now represents a half wave plate. A detector is then used to detect radiation that

exits the polarising cube through the fully extinguished output arm. When terahertz radiation is present the phase rotation induced within the ZnTe crystal causes some radiation to exit the polariser through the, previously extinguished, arm of the polarising cube. This radiation is then incident upon the detector. Using balanced detection the measurable signal could be defined as $S = \left|\overline{E}_{out,x}\right|^2 - \left|\overline{E}_{out,y}\right|^2$ whereas now the measurable signal is defined as simply $S = \left|\overline{E}_{out,x,y}\right|^2$. Using Eq. (2.76) it is possible to derive an expression for the terahertz field strength as a function of the measured signal,

$$S = \frac{1}{2} E_0 e^{-\frac{i3}{4}\pi}(-2i \sin \Gamma), \tag{2.81}$$

where E_0 is the intensity of the probe laser on the ZnTe surface. When combined with Eq. (2.75) this leaves

$$S = \frac{1}{2} E_0 e^{-\frac{i3}{4}\pi}\left(-2i \sin\left(\frac{\pi d}{\lambda_0} n_0^3 r_{41} E_T\right)\right). \tag{2.82}$$

Whilst this detection system is not as sensitive as balanced detection it does enable spatial mapping of the terahertz radiation to be performed. This spatial mapping can be achieved by using a two dimensional CCD camera which images the ZnTe crystal surface. The phase rotation imposed onto the optical probe beam only occurs when in spatial areas where the probe beam overlaps with terahertz radiation.

2.5 Photoconductive Antenna Generation

Photoconductive antennas (PCAs) are common sources of pulsed terahertz radiation. A PCA consists of a semiconducting material with a set of electrodes attached to the surface. This semiconducting material is held under a high electrical bias field via a voltage which is applied to the electrodes. The antenna is photoexcited by an ultrafast laser with photons that have a larger energy than the bandgap, thus liberating charge carriers from the valence band into the conduction band. Whilst in the conduction band the charge carriers are able to accelerate under the applied electrical bias field. Maxwell's equations state that an accelerating charge will emit radiation. This is the principle underlying mechanism that allows terahertz radiation to be generated from PCAs. The charge carriers continue to accelerate in the conduction band until they drop back down into the valence band. The time that the charge carriers remain in the conduction band is called the recombination lifetime and is wholly governed by the semiconductor material properties.

The two processes that govern the length of time that the charge carriers can accelerate for are interband scattering and screening. Interband scattering as the

name suggests describes the process through which charge carriers collide and scatter off other carriers and defects within the material. Having collisions within the conduction band reduces the mean free path of the electrons. This in turn can help to broaden the bandwidth of the generated terahertz pulse, as it effectively shortens generated radiations temporal profile. For the scattering process to be dominant or have a noticeable effect their must exist a very large electron density within the conduction band or a large number of defects within the material. Screening describes a process through which the electric field created by the non-uniform spatial density of charge carriers effects their acceleration due to the applied bias field. This can be seen in Fig. 2.12, where the red dots represent the holes and the blue dots represent electrons. As can be seen the electrons and holes are initally attracted towards the positivly and negativly charged electrodes respectivley. This causes a build up of electrons and holes around these electrodes in turn producing a large charge carrier density, and along with that a large electric field. This electric field causes the charge carriers to attempt to spread out, effectivly slowing or stopping their motion towards the electrode. This reduces the duration of the charge carriers acceleration and therefore increases the bandwidth of the generated terahertz radiation.

Generally, these recombination lifetimes are much larger than 100 fs and contribute towards the temporal structure of the generated terahertz pulse. Due to the recombination lifetime generally being much longer than that of the temporal duration of the excitation laser pulse, which is typically on the order of 30–100 fs, and temporal tuning imposed by the excitation laser is smeared out. This makes PCAs unsuitable for applications that require temporal tuning of the terahertz radiation imposed by the excitation laser radiation.

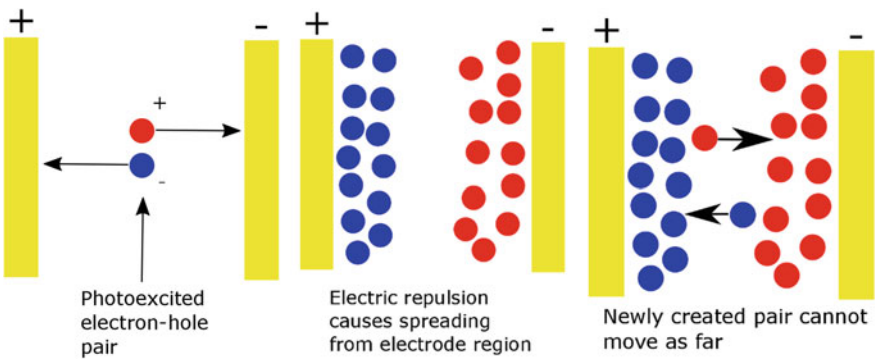

Fig. 2.12 Schematic diagram showing the effects of screening. Here the *blue circles* represent electrons whilst the *red circles* represent holes. As can be seen a build-up of negatively charged electrons exists around the +ve electrode whilst a build-up of positively charged holes exist around the −ve electrode

The electric field of the generated radiation can be expressed as [21]

$$\frac{\partial^2}{\partial y^2}E(\omega) + \frac{\omega}{c^2}\epsilon_0 E(\omega) = -i\omega\mu_0 J(\omega), \tag{2.83}$$

where $E(\omega)$ is the terahertz electric field, ω is the angular frequency and $J(\omega)$ is the current surge across the PCA. This expression is valid as long as the antenna has an aperture much larger than the wavelength of the generated terahertz radiation and the bias field across the antenna is uniform. A final condition that the terahertz field strength is much smaller than that of the applied bias field is also required as this description does not account for interactions between the liberated charges and generated terahertz radiation [21].

The current surge across the wafer as a function of time, $J(t)$, can be expressed by the non-equilibrium distribution of the free carriers within the antenna. This takes the form

$$J(t) = \frac{\hbar e}{4\pi^3}\int k_z\left[\frac{f_e}{m_e} - \frac{f_h}{m_h}\right]dk, \tag{2.84}$$

where e is the charge of an electron, k_z is the momentum vector of the charge carrier resolved into the z direction, f_e and f_h are the distribution of the free electrons and holes antenna respectively and m_e and m_h are the effective masses of the electrons and holes respectively. Making the assumption that $m_e \ll m_h$ enables the second term within the bracket to be ignored leaving,

$$J(t) = \frac{\hbar e}{4\pi^3}\int \frac{k_z f_e}{m_e}dk. \tag{2.85}$$

In order to further calculate the form of $J(t)$ the form of f_e must be approximated. This can be done by assuming a Boltzmann distribution of carriers, which takes the form,

$$\frac{\partial}{\partial t}f_e + \left(\frac{\hbar k}{m_e}\frac{\partial}{\partial r} + \frac{e}{\hbar}\frac{\partial}{\partial k}\right)f_e = -\Gamma(f_e - f_{eo}) + \Phi \mathrm{f}_e + G(t)\frac{\pi^2\delta(k-k_0)}{k_0^2}, \tag{2.86}$$

where Γ is the recombination rate, Φ is the inverse lifetime and $G(t)$ is the generation rate. The generation rate describes the flux of photons that have an energy larger than the semiconductor band gap and are incident upon the surface of the antenna. By considering the quantities that describe the laser pulse such as the intensity, I_0, the group velocity, v_0, and temporal duration, Δ, as well as the quantities that govern semiconductor-laser interaction such as absorption, α, and reflectivity, R, the generation rate can be expressed as [21],

$$G(t) = \frac{\alpha(1-R)I_0}{\hbar\omega_0} e^{\alpha y} e^{-\frac{t}{2\Delta^2}}. \tag{2.87}$$

Now by using Eq. (2.85) it is possible to express $J(t)$ in the frequency,

$$J(\omega) = \frac{e}{m_e} E_0[\Phi(k_0 - i\omega)]^{-1}[\Gamma(k_0) + \Phi(k_0) - i\omega]^{-1} G(\omega). \tag{2.88}$$

The Fourier transform of Eq. (2.87) can be taken yielding an expression which describes the generation rate in the frequency domain:

$$G(\omega) = \frac{\alpha(1-R)I_0}{\hbar\omega_0} e^{-\alpha y} e^{\frac{\omega^2\Delta^2}{2}} e^{\frac{i\omega}{2\Delta^2}}. \tag{2.89}$$

The above expression can now be used to form an expression for the terahertz electric field generated by the PCA in the frequency domain,

$$\begin{aligned} E(\omega) = &-\sqrt{\frac{\mu_0}{\epsilon_0}} A(\omega) \left[1 - \frac{i\omega(n+n_0)}{\alpha c}\right]^{-1} \\ &\times \frac{2n\left[1 - \frac{i\omega(n_0+n_e)}{\alpha e}\right]}{n+n_e^2} e^{\frac{i\omega n d}{c}} \left[1 - r^2 e^{\frac{i2\pi d\omega}{c}}\right]^{-1}, \end{aligned} \tag{2.90}$$

where $n_0 = \frac{c}{v_0}$, $n = \sqrt{\epsilon}$ and $n_e = \sqrt{\epsilon_0}$ and represent the refractive indices inside and outside the wafer respectively and $r = n - n_e/n + n_e$. The variable $A(\omega)$ contains the excitation radiation parameters and can be expressed as follows,

$$A(\omega) = \frac{\frac{e^2}{m_e} E_0(1-R)I_0\Delta}{\hbar\omega_0} \tau\tau_p e^{-\frac{\omega^2\Delta^2}{2}} (1 - i\omega\tau)^{-1} \left(1 - i\omega\tau_p\right)^{-1}, \tag{2.91}$$

where τ and τ_p represent the inverse lifetime, Φ and the inverse relaxation lifetime, Γ, respectively [21].

2.6 Longitudinally Polarised Radiation

Typically the electric fields of a propagating electromagnetic field in free space, light, are thought of as only having transversely polarised components. This means that the electric field lines point orthogonally to the direction of the propagation of the electromagnetic field. This, however, is not completely correct as all forms of free space propagating electromagnetic radiation, apart from azimuthally polarised radiation, have electric fields with longitudinally polarised components, i.e. electric

field components that are orientated in the direction of the propagating electromagnetic field. This can be seen by analysing

$$\nabla \cdot \overline{E}(x, y, z) = \rho_f, \tag{2.92}$$

where $\overline{E}(x, y, z)$ is an electric field in Cartesian spatial co-ordinates (x, y, z) and ρ_f is the density of free charges in the space occupied by the field. As this is a field propagating in free space, ρ_f can be set to zero. Therefore Eq. (2.13) states that the total spatial gradient of the electric field is zero, this means that the field lines cannot begin or end leaving two possible options. The first is that the field carries on to an infinite spatial extent and the second is that the field lines loop round and in doing so create a component of the field that points in the direction of propagation.

To investigate the form of the longitudinally polarised electric field component Eq. (2.92) can be rearranged by splitting $\overline{E}(x, y, z)$ and ∇ into their orthogonally polarised components i, j and k such that,

$$\frac{\partial}{\partial x}\hat{i}E(x, y, z) + \frac{\partial}{\partial y}\hat{j}\overline{E}(x, y, z) + \frac{\partial}{\partial z}\hat{k}E(x, y, z) = 0. \tag{2.93}$$

where i, j and k lie along the x, y and z axes respectively. Rearranging for the longitudinal component, k, subsequently yields,

$$E_k(x, y, z) = -\int_{-\infty}^{\infty} \nabla_{\perp} E_{\perp}(x, y, z)dz + C(x, y), \tag{2.94}$$

where $\perp$ denotes the linear combination of i and j and $C(x, y)$ is an unknown constant due to the integration. This constant however does not vary in z and so for pulsed radiation it can be said to be zero. This is because for pulsed radiation $E_k(x, y, z)$ and $E_{\perp}(x, y, z)$ must be zero at some z and for this to be true $C(x,y)$ must also be zero at that z and because it does not vary in z must therefore be zero for all z.

As can be seen from Eq. (2.94) the longitudinally polarised electric field component depends strongly upon the spatial gradient of the transversely polarised electric field component and in fact is maximised when the spatial gradient of the transversely polarised electric field component is maximised. This attribute is in fact apparent in electromagnetic modes with strong transverse gradients. Modes such as the radially polarised Laguerre-Gaussian 01 (LG01*) mode contain strong spatial gradients on axis and strong longitudinal fields have been observed on the axis of such modes [20]. Effects such as the tight focusing of radiation can also increase the amount of the electric field that can be resolved into the longitudinal direction. Again this has been observed in both complex modes with strong transverse gradients as well as simple standard Gaussian beams [22].

2.7 Acceleration of Charged Particles

A charged particle is a particle that is able to interact with an electromagnetic field. Within this section the acceleration of charged particles by external electromagnetic fields is discussed. For simplicity only electrons are considered, and assumed to be a point-like particle with no spatial dimension. To examine how an electron is influenced by an external electromagnetic field two properties of the electron must first be defined. Firstly its charge; the charge of the electron determines the strength of the interaction between an electromagnetic field and the electron. Secondly the electron mass is describes as resistance of the electron to a change in velocity.

In Newtonian physics the mass of a particle is constant and independent of velocity or acceleration. This is commonly referred to as the rest mass of the particle and for an electron denoted m_e. To describe the acceleration of an electron first one must be able to define its position in space. This is done in Cartesian co-ordinates and defined as a vector $\bar{x}$. Following this the velocity of the particle can be defined as $\bar{v}$ where

$$\bar{v} = \frac{\partial \bar{x}}{\partial t}. \tag{2.95}$$

Newton's first law of motion states that the velocity of a particle will remain constant unless an external force acts upon the particle. Momentum, $\overline{P}$, is now introduced as a quantity which describes how much force is needed to change the velocity of a particle and can be expressed as [23]

$$\overline{P} = m_e \bar{v}. \tag{2.96}$$

Newton's second law of motion now defines the force, $\overline{F}$, as [23]

$$\overline{F} = \frac{\partial \overline{P}}{\partial t}. \tag{2.97}$$

To understand how the force applied to a particle relates to a change in its velocity two quantities are introduced, the first being kinetic energy, $\overline{E}_k$, and the second being work done which is the change in kinetic energy, $\Delta\overline{E}_k$. The work done to a particle by a force can be described as [23]

$$\Delta\overline{E}_k = \int \overline{F} d\bar{x}. \tag{2.98}$$

By assuming that the mass of a particle is not a function of its velocity, which for now can be assumed, and by defining $\overline{E}_k = 0$ when $\bar{v} = 0$ the kinetic energy of a particle can be written as

$$\overline{E}_k = \frac{1}{2} m_e \overline{v}^2. \tag{2.99}$$

The act of placing a charged particle into a static electromagnetic field with potential energy $\overline{U}$ enables the exchange of energy between the particle and field. The sum of the kinetic energy and potential energy must always be constant and is defined as the total energy, $\overline{E}$. Noting that the field is static, i.e. $\frac{\partial \overline{U}}{\partial t} = 0$, it is possible to express the potential energy as a function of the work done,

$$\nabla \overline{E}_k = -\frac{\partial \overline{U}}{\partial \overline{x}}. \tag{2.100}$$

Here it is now possible to decompose the vectors onto the three Cartesian co-ordinate axes such that,

$$E_{k,x} = \frac{\partial}{\partial x} U_x, \tag{2.101}$$

$$E_{k,y} = \frac{\partial}{\partial y} U_y, \tag{2.102}$$

$$E_{k,z} = \frac{\partial}{\partial z} U_z. \tag{2.103}$$

Commonly it is attractive to accelerate a particle in one direction. It can be seen from the above equations that in order to do so the potential of the field must therefore be orientated in that direction. For instance taking z to be the desired direction of electron beam propagation it can be seen that the accelerating potential must also lie along the z axis.

2.7.1 Relativistic Motion

As described above charged particles can be described by three quantities, their position and velocity at a fixed time $(\overline{x}, \overline{v}, t)$. In Newtonian physics the amount of energy needed to accelerate a particle from $E_{k,z}(t = 1)$ to $E_{k,z}(t = 2)$ is not dependent upon the initial kinetic energy. This, whilst being a good approximation at low energies, does not hold for high energies when the velocity of the particle becomes a noticeable proportion of the speed of light. In such cases the mass of a particle is no longer independent of the velocity, but in fact can be expressed as a function of it,

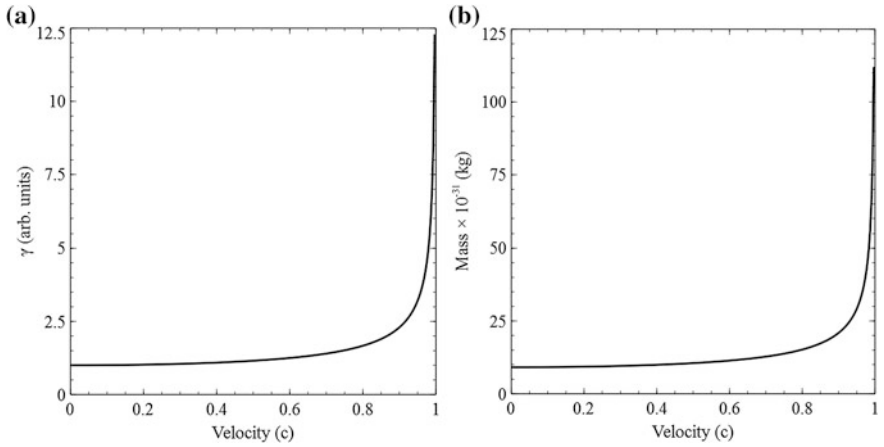

Fig. 2.13 Simulations produced to show **a** γ as a function of velocity and **b** the mass of an electron as a function of velocity

$$m = \gamma m_e, \tag{2.104}$$

where γ is a dimensionless quantity which describes the velocity of a particle as a fraction of the speed of light and can be expressed as

$$\gamma = \frac{1}{\sqrt{(1-\beta^2)}}, \tag{2.105}$$

where

$$\beta = \frac{v}{c}. \tag{2.106}$$

The relationship between γ and v can be seen in Fig. 2.13a. As can be seen in Fig. 2.13b for low velocities, velocities less than approximately half the speed of light, the mass of an electron remains constant and does not change appreciably as a function of velocity. However when the velocity of the electron approaches c its mass rapidly starts to increase tending towards infinity.

Whilst this does not change the relationship between force and momentum it does change the definition of momentum such that now,

$$\overline{P} = \gamma m_e \overline{v}. \tag{2.107}$$

Noticing now that as the velocity of the electron approaches c its momentum increases with respect to the velocity of the electron. Therefore the energy of the particle must be defined as

$$E = \gamma m_e c^2. \tag{2.108}$$

The kinetic energy is now the total energy minus the rest energy, $m_e c^2$, of the electron,

$$E_k = m_e c^2(\gamma - 1). \tag{2.109}$$

2.7.2 Acceleration Within an Electromagnetic Field

To analyse how an electron is accelerated by an electromagnetic field the change in momentum is calculated instead of the velocity. This is because in the relativistic regime there is very little change in the velocity of an electron where as there is a large change in the energy of an electron. The change in momentum over time is expressed as

$$\frac{\partial \overline{P}}{\partial t} = -q_e(\overline{E} + \overline{v} \times \overline{B}), \tag{2.110}$$

where

$$\overline{P} = \gamma mc\beta. \tag{2.111}$$

The change in γ which relates to the velocity of the particle is given as

$$\frac{\partial \gamma}{\partial t} = -\frac{q_e}{m_e c^2}\overline{v} \cdot \overline{E}, \tag{2.112}$$

As previously described an electron will be accelerated in the direction of the electric field. Therefore for co-linear acceleration with a propagating field the electric field radiation should have a strong on-axis component. Such components are present in modes such as radially polarised modes and Hermite-Gaussian TEM_{01} (HG01) modes. The electric field from a HG01 mode can be expressed in terms of its transverse, r, and longitudinal, z, field components as

$$E_r = \frac{4E_0\omega_0 r}{\sqrt{2\omega^2(z)}} e^{\left(-\frac{r^2}{\omega^2(z)}\right)} \sin(\phi), \tag{2.113}$$

$$E_z = \frac{4E_0\omega_o}{\sqrt{2}k\omega^2(z)} e^{\left(-\frac{r^2}{\omega^2(z)}\right)} \left[\left(1 - \frac{2r^2}{\omega^2(z)}\right)\cos\phi - \frac{2zr^2}{Z_R\omega^2(z)}\sin\phi\right]. \tag{2.114}$$

If we assume that the electrons being accelerated are on axis, i.e. are positioned at $r = 0$, then $E_r = 0$ and the accelerating field becomes,

$$E_z = \frac{4E_0\omega_o}{\sqrt{2}k\omega^2(z)}\cos\phi. \tag{2.115}$$

This can now be used in conjunction with Eq. (2.110) such that it becomes

$$\frac{\partial \overline{P}_z}{\partial t} = -q_e\left(\frac{4E_0\omega_o}{\sqrt{2}k\omega^2(z)}\cos\phi + \overline{v}\times\overline{B}\right), \tag{2.116}$$

and as we are now only considering on-axis acceleration in the z direction the magnetic field becomes zero leaving,

$$\frac{\partial \overline{P}_z}{\partial t} = -q_e\left(\frac{4E_0\omega_o}{\sqrt{2}k\omega^2(z)}\cos\phi\right). \tag{2.117}$$

Equation (2.112) now also becomes

$$\frac{\partial \gamma_z}{\partial t} = -\frac{q_e}{m_e c^2}v_z \cdot \frac{4E_0\omega_o}{\sqrt{2}k\omega^2(z)} \tag{2.118}$$

These two equations describe the on-axis longitudinal acceleration of a relativistic electron by a radially polarised electric field. The change in the momentum of the electron as a function of time describes how much the particle is accelerated over a given time period whilst the change in γ_z describes change in the energy and velocity of the particle over a given time period. Whilst both these quantities are linked and can provide the same information they are commonly used in different ways to obtain different information about the acceleration of a particle.

2.7.3 *Acceleration with Terahertz Radiation*

Typically electron bunches have temporal profiles on the order of 0.5–10 ps and are accelerated using radio frequency electromagnetic radiation. Radio frequency electromagnetic radiation typically has temporal periods on the 10's ns scale. This mismatch in temporal periods makes it very difficult to perform fine temporal tuning of the longitudinal profile of the electron bunch. It would therefore be attractive to use radiation with a much shorter period to perform fine temporal tuning of the longitudinal profile, providing the ability to produce ultrashort electron bunches and electron bunches with unique longitudinal profiles. Such bunches would be very useful in fields such as pump-probe spectroscopy, synchronisation and particle therapy.

Whilst radiation with extremely small temporal periods, such as optical radiation, would be ideal for the fine temporal tuning of relativistic electron bunches the fact that the period is much less than the longitudinal profile of the electron bunch causes a new problem. This problem involves the phase slippage of the particle bunch relative to the modulation radiation; as they co-propagate the electron bunch travels slightly slower than the modulating radiation. This causes the electron bunch to slip through many cycles of the modulating radiation meaning it experiences, on average, as many positive field areas as it does negative field areas essentially providing zero net modulation.

Electromagnetic radiation with periods similar to that of the electron bunch, 0.5–10 ps, such as terahertz radiation does not present either of these problems. The temporal profile of terahertz radiation is short enough that fine temporal adjustments to the longitudinal profile of the electron bunch can be carried out. In fact depending on the generation source these temporal manipulations can be directly imposed by a pump optical laser and if a laser driven terahertz source is chosen this inherently enables sub 10 fs electron beam—laser beam synchronisation. However its temporal period is not so short as to enable electron bunches to co-propagate and experience a number of positive and negative cycles. Electron bunches with typical energies of approximately 25 MeV are able to co-propagate with a terahertz pulse centred around 0.3 THz for approximately 1 m before they fall half a cycle out of phase [24]. This length only increases as the electron bunch energy increases and for the same energy is much higher than the 30 μm coherence length which would be achievable with 800 nm optical radiation.

Whilst terahertz radiation appears to be an obvious answer to being able to provide fine scale longitudinal energy modulation to relativistic electron bunches, only in the last few years have terahertz sources capable of producing useable field strengths being developed. Sources able to produce terahertz field electric strengths in excess of 500 $kVcm^{-1}$ are required for noticeable and useful energy modulation of relativistic bunches. These sources must also have a unique and complex polarisation state allowing them to have an on-axis strong longitudinally polarised electric field component. As of now such a source has not been developed; however the individual components required have. It would therefore be important to further investigate the development of such a source which is the main aim of this work.

References

1. D.J. Griffiths, *Introduction to electrodynamics* (Prentice Hall, New Jersey, 1999)
2. R.W. Boyd, *Nonlinear Optics* (Academic Press, 2003)
3. J.D. Jackson, *Classical Electrodynamics*, 3rd edn. (John Wiley & Sons, 1999)
4. S. Casalbuoni, H. Schlarb, B. Schmidt, P. Schmuser, B. Steffen and A. Winter, Numerical studies on the electro-optic detection of femtosecond electron bunches. Phys. Rev. Spec. Top. Accelerators Beams **11**, 072802 (2008)
5. J. Hebling, G. Almäsi, I.Z. Kozma, Velocity matching by pulse front tilting for large-area THz-pulse generation. Opt. Express **10**, 1161 (2002)

6. H. Hirori, A. Doi, F. Blanchard, K. Tanaka, Single-cycle terahertz pulses with amplitudes exceeding 1 MV/cm generated by optical rectification in $LiNbO_3$. Appl. Phys. Lett. **98**, 091106 (2011)
7. J. Oden, J. Meilhan, J. Lalanne-Dera, J. Roux, F. Garet, J. Coutaz, F. Simoens, Imaging of broadband terahertz beams using an array of antenna-coupled microbolometers operating at room termperature. Opt. Express **21**, 4817 (2013)
8. S. Cherednichenko, A. Hammar, S. Bevilacqua, A room temperature bolometer for terahertz coherent and incoherent detection. IEEE Trans. Terahertz Sci. Technol. **1**, 395 (2011)
9. F. Simoens, *THz Bolometer Detectors* (Springer, 2013)
10. L. Fernandes, P. Kaufmann, R. Marcon, A.S. Kadaka, A. Marun, R. Godoy, E.C. Bortolucci, M.B. Zakia and J. A. Diniz, Photometry of THz radiation using Golay cell detector, in *General Assembly and Scientific Symposium, 2011 XXXth URSI*, Istanbul, 2011
11. W.J. Stillman, M.S. Shur, Closing the gap: plasma wave electronic terahertz detectors. J. Nanoelectron. Optoelectron. **2**, 209 (2007)
12. C. Winnewisser, P. Uhd Jepsen, M. Schall, V. Schyja, H. Helm, Electro-optic detection of THz radiation in LiTaO3, LiNbO3 and ZnTe. Appl. Phys. Lett. **70**, 3069 (1997)
13. G. Gallot, J. Zhang, R.W. McGowan, T.- I. Jeon, D. Grischkowsky, Measurements of the THz absorption and dispersion of ZnTe and their relevance to the electro-optic detection of THz radiation. Appl. Phys. Lett. **74**, 3450 (1999)
14. A. Leitensotorfer, S. Hunsche, J. Shah, M.C. Nuss, W.H. Knox, Detectors and sources for ultrabroadband electro-optic sampling: experiment and theory. Appl. Phys. Lett. **74**, 1516 (1999)
15. S. Park, M.R. Mellock, A.M. Weiner, Comparison of terahertz waveforms measured by electro-optic and photoconductive sampling. Appl. Phys. Lett. **73**, 3184 (1998)
16. N. Yasumatsu, S. Watanabe, Precise real-time polarization measurement of terahertz electromagnetic waves by a spinning electro-optic sensor. Rev. Sci. Instr. **83**, 023104 (2012)
17. S. Casalbuoni, H. Schlarb, B. Schmidt, P. Schmuster, B. Steffen and A. Winter, *Numerical studies on the electro-optic sampling of relativistic electron bunches* (DESY, TELSA Report, 2005)
18. D.A. Walsh, M.J. Cliffe, E.W. Snedden, D.M. Graham, W.A. Gillespie and S.P. Jamison, Role of misalignment-induced angular chirrp in the electro-optic detection of THz waves. Opt. Express **22**, 12028 (2014)
19. Z. Gui-hua and W. Ya-min, Study of jones matrix of the birefringent crystal, in *Symposium on Photonics and Optoelectronics, 2009. SOPO 2009*. (Wuhan, 2009)
20. M.J. Cliffe, A. Rodak, D.M. Graham and S. P. Jamison, Generation of longitudinally polarized terahertz radiation with field amplitudes exceeding 2 kV/cm. Appl. Phys. Lett. **105**, 1191112 (2014)
21. V.N. Trukhin, A.V. Andrianov and N. N. Zinov'ev, Generation of terahertz radiation by a photoconductive antenna. Acta. Phys. Pol. A **113**, 921 (2008)
22. S. Winnerl, R. Hubrich, M. Mittendorff, H. Schneider and M. Helm, Universal phase relation between longitudinal and transverse fields observed in focused terahertz beams. New J. Phys. **14**, 103049 (2012)
23. J.R. Taylor, *Classical Mechanics*. (University Science Books, 2004)
24. S.P. Jamison, M.J. Cliffe, D.M. Graham, T. Thakker, B. Muratori, Y.M. Saveliev , R.J. Smith, W.R. Flavell, D.J. Holder, D. Newton and A. Wolski, Phase space manipulation with laser-generated terahertz pulses, in *34th International Free Electron Laser Conference*, Japan (2012)

Chapter 3
Experimental Apparatus

This chapter gives an overview of the apparatus and equipment used within this project. The different laser systems used are listed along with their specifications and capabilities. The Accelerators and Lasers In Combined Experiments (ALICE) 25 MeV energy recovery linear accelerator which is based at the Daresbury STFC Laboratory is described along with some preliminary data obtained from experiments carried out on ALICE.

3.1 Laser Systems

Laser systems were key instruments involved in all of the experiments carried out within this project. One of the main laser systems used was a regenerative amplifier based laser system. The laser system provided up to 2 mJ of pulse energy at a repetition rate of up to 1 kHz. The radiation generated by this system was centred on a wavelength of 800 nm and had a pulse width of 45 fs. The regenerative laser system consist of three separate sections, the pump, oscillator and regenerative cavity. The pump laser used within this system was a Q-switched intra-cavity doubled diode-pumped solid state laser (DPSS). The DPSS laser used neodymium-doped yttrium lithium fluoride (Nd:YLF) as its gain material to produce radiation centred on a wavelength of 1053 nm. This radiation was frequency doubled to produce 20 mJ of pulsed radiation at a 1 kHz repetition rate with a duration of 250 ns centred at a wavelength of 527 nm. The oscillator used within this laser system was a titanium sapphire (Ti:Sapph) crystal mode-locked laser. It was pumped by a separate frequency doubled DPSS laser which produced 4.7 W of radiation with a wavelength of 532 nm. The oscillator produced a train of sub-15 fs pulses with a repetition rate of 81.25 MHz, the average power generated by this

M.J. Cliffe, *Longitudinally Polarised Terahertz Radiation for Relativistic Particle Acceleration*, Springer Theses, DOI 10.1007/978-3-319-48643-7_3

laser was 400 mW. The regenerative amplifier combined both the oscillator and the pump radiation inside a *z*-shaped cavity. Before entering the cavity the oscillator beam first passed through a Faraday isolator. This isolator only allowed radiation to propagate through in one direction, preventing any back reflections from being transmitted back into the oscillator. The oscillator beam then passed through a set of gratings which added a spectral chirp onto the pulses. This increased the oscillator radiation pulse duration, lowering the peak power, which was required to avoid material damage inside the regenerative amplifier cavity. The stretched pulses then passed through a Pockels cell which only allowed 1 in every 81,250 pulses to pass through, enabling the oscillator pulse train to be synchronised to the 1 kHz DPSS pump laser. These pulses then enter the regenerative amplifier cavity. Within this cavity the pulses make multiple passes through the Ti:Sapph gain material each time being amplified further. A second Pockels cell was situated within the cavity and after a pulse had made a certain number of cavity round-trips redirected the pulse out of the cavity. Once out of the cavity the amplified pulses passed through a third Pockels cell that enabled the output repetition rate to be varied. The pulses were then expanded in size using a set of lenses which acted as a Galilean beam expander. Once expanded the pulses entered into a compressor. This compressor removed the spectral chirp that was previously imposed and compressed the pulse duration down to 50 fs. A schematic diagram of the chirped-pulse regenerative amplifier laser cavity can be seen in Fig. 3.1.

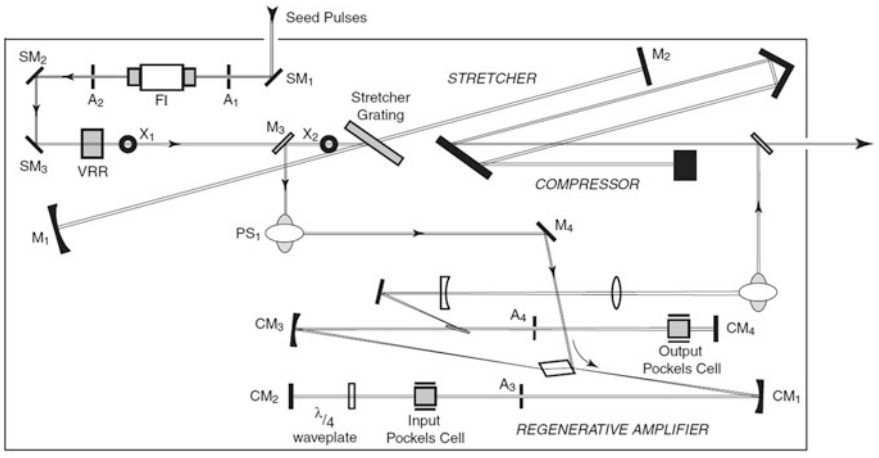

Fig. 3.1 Schematic diagram of a chirped-pulse regenerative amplifier laser cavity. F1 represents a faraday isolator, $A_{1,2,3,4}$ represent alignment apertures, $SM_{1,2}$ are the seed mirrors and the VRR is the vertical retro-reflector [1]

3.2 Large Area Photoconductive Antenna

Experiments carried out within this project commonly required a high power, laser driven, pulsed terahertz source. For many of these experiments a large area photoconductive antenna was used. Within this section the workings of such antenna will be detailed along with how it was used, built, designed and works. The theory behind how a photoconductive antenna generates terahertz radiation can be found in Sect. 2.5 of this thesis.

There were two types of large area photoconductive antenna used within this project. One produced linearly polarised terahertz and the other produced radially polarised terahertz radiation. They both consisted of 75 mm diameter semi-insulating gallium arsenide (SI-GaAs) wafers to which electrodes were attached. A high electrical voltage was applied to the electrodes and they were subsequently photo-excited using a regenerative amplifier laser system. The photo-excitation pulses typically consisted of 1.8 mJ of energy per pulse with a temporal duration of 50 fs and a central wavelength of 800 nm. Due to the laser used these pulses could be applied at a maximum repetition rate of up to 1 kHz. However due to the power supply used to provide the voltage pulses to the electrodes, terahertz radiation generation was limited to repetition rates of 250 Hz.

The wafer was housed in a polytetrafluoroethylene (PTFE) enclosure which had two holes cut into it as seen in Fig. 3.2. One hole allowed for the pump beam to photo-excite the wafer and the second allowed for the forward travelling generated terahertz radiation to leave. The power supply used to generate the high voltage pulse which was applied to the electrodes consisted of three main parts. The first was a $\pm$ 5 V laboratory power supply, the second was the trigger receiver box and the

Fig. 3.2 Radially biased large area photoconductive antenna housed in its PTFE enclosure

third was the high voltage section. The high voltage section consisted of a coil pack from a car and was able to transform the 5 V direct current (DC) laboratory supply into a 180 kV pulse. This was triggered by a trigger supplied by the laser and entered into the triggering electronics. When this trigger flipped the voltage pulse was applied to the electrodes. Wired in parallel was a high resistance potential divider that divided the voltage by a factor of 4000 enabling it to be monitored on an oscilloscope.

As previously stated the two types of wafer produced terahertz radiation with two polarisation states, linear and radial. This was achieved by altering the electrode geometry of the wafer. Due to the way the terahertz radiation is generated, accelerating a photo-excited charge under an electrical bias field, the polarisation of the generated terahertz radiation will always be in the direction of the charges acceleration, or in the direction of the applied bias voltage. By exploiting this property of the photoconductive antenna complex polarisation states could be easily generated.

In order to generate linearly polarised terahertz radiation electrodes which consisted of horizontal aluminium foil strips were used and were applied with adhesive to the surface of the antenna. The electrodes created an electric bias field pattern that had electric field lines running horizontally across the surface of the wafer, and remained approximately parallel to each other. This meant that the photo-excited electrons situated within the conduction band would accelerate along these field lines and generate terahertz radiation polarised in a vertical near uniform state. This antenna was used for a number of experiments, including the testing of electro-optical detection schemes due to the simplicity of the polarisation state of the generated terahertz radiation. In typical experimental setups it was able to produce peak terahertz electric field strengths on the order of 10 $kVcm^{-1}$ when focused to a 5 mm $1/e^2$ spot. The antenna in this configuration was able to generated terahertz radiation with a near single cycle, near unipolar temporal structure with temporal durations on the order of 300 fs. A unique and interesting feature of the radiation generated by this antenna was the near unipolar temporal structure. This is mostly due to the large aperture of the antenna and is not found on most other commercially available photoconductive antennas which are typically much smaller in size.

The second antenna was able to generate radially polarised terahertz radiation by exploiting the same physics as above. The electrode geometry on this antenna consisted of an outer annular electrode and central hemispherical electrode and this is described in further detail in Chap. 6.

3.3 Accelerators and Lasers in Combined Experiments (ALICE)

The ALICE accelerator is a superconducting linear accelerator based at the STFC laboratory Daresbury. ALICE is an energy recovery linear accelerator and its construction was completed in 2010. ALICE was designed, built and is used to both

produce radiation and interact electron bunches with externally generated electro-magnetic radiation. Equipment such as a free electron laser undulator and coherent transition radiation (CTR) foils situated around the accelerator beam pipe allow for the generation of many types of radiation such as mid-infrared and terahertz. A picture the ALICE injection line can be seen in Fig. 3.3 and a schematic view can be seen in Fig. 3.4.

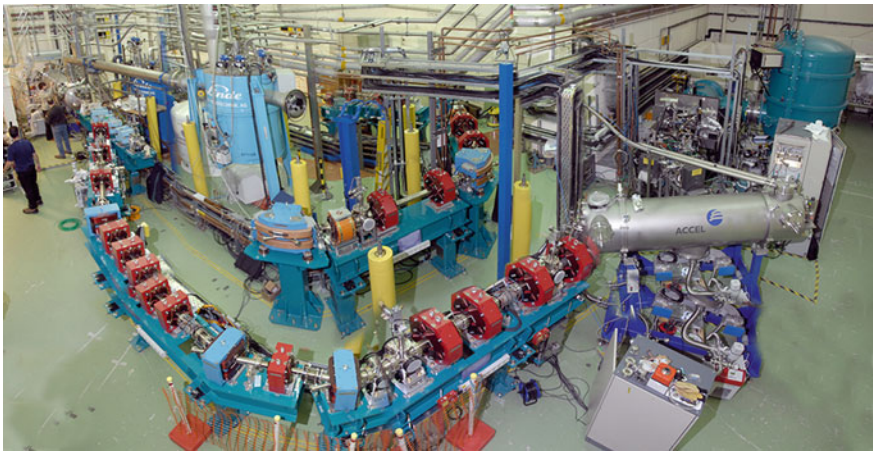

Fig. 3.3 Photograph of the ALICE accelerator based at STFC Daresbury Laboratory

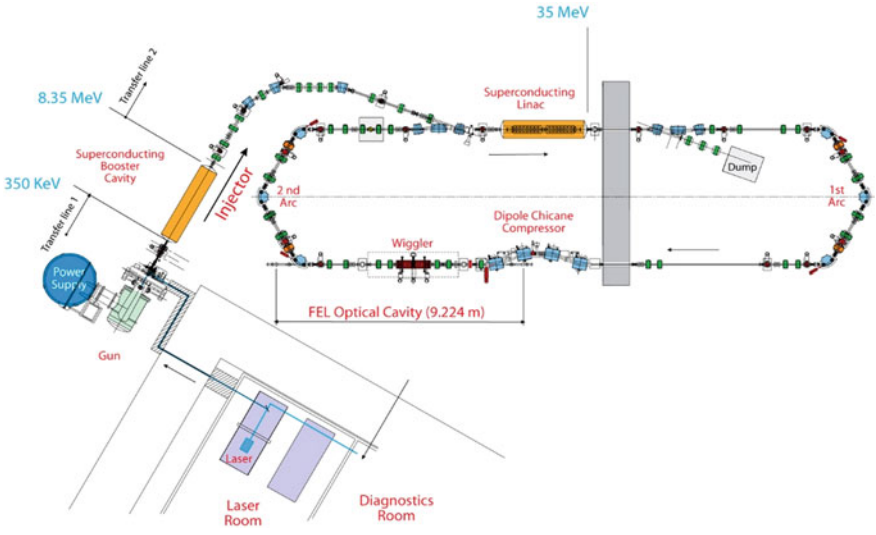

Fig. 3.4 Schematic diagram of the ALICE accelerator

3.3.1 Accelerator Beam Line

The electron beam in the ALICE accelerator is generated by a copper photocathode that is photo-excited by a laser. The laser is an 81.25 MHz mode-locked oscillator with a 1 μm output wavelength. The output is frequency doubled to form a beam with a 532 nm wavelength radiation, this doubled radiation has a FWHM temporal duration of 28 ps. This beam is then transported to the cathode where it liberates electrons. The FWHM spot size of the laser on the cathode is 4.1 mm and can be tuned. The cathode is made from copper and has a measured quantum efficiency of approximately 4%. The electrons, once liberated, are accelerated by the electron gun which consists of a DC voltage. The DC voltage of the gun is 230 kV but this can be increased to 350 kV with the aid of high voltage ceramic inserts. The electrons are then accelerated by the booster which accelerates the electrons to relativistic energies of around 8.35 MeV. These electrons are then transported into the main ring. The first element in this ring that the electrons encounter is the superconducting energy recovery cavity, this cavity operates at 1.3 GHz and accelerates the electron bunch up to a maximum energy of 35 MeV. The electrons then travel around the accelerator past the radiation injection point, which is used to inject modulating radiation such as terahertz or near-infrared radiation. The electrons then enter a dispersive region, which consists of a chicane shaped beam line through which the electrons pass. This dispersive region can be used to temporally compress or stretch the electron bunch. This dispersive region can also be used as an energy spectrometer if a screen is placed in the centre. After the dispersive region the electron bunch passes through a free electron laser (FEL) cavity which consists of a series of alternating magnets which make the electron beam oscillate in the transverse dimension. After this element the electron beam passes through radiation injection stage two and the coherent transition radiation generation point, after which it returns to the superconducting cavity.

The electron bunch temporal structure consists of two parts, the micro structure and the macro structure, both of these structures can be tuned by adjusting the injection laser repetition rate. The maximum micro bunch repetition rate is 81.25 MHz with a maximum macro bunch repetition rate of 10 Hz. The electron bunches have a maximum charge of 80 pC with a compressed bunch length less than 1 ps.

When the beam re-enters the superconducting cavity the electron beam dynamics are set up such that it is π out of phase with any newly injected bunch. This enables the cavity to take energy from the old beam and give it to the new beam, this is called energy recovery. The effects of energy recovery can be seen in Fig. 3.5, here Fig. 3.5b shows the power draw of the main accelerating cavity with energy recovery system disabled whilst Fig. 3.5a shows the power draw of the main accelerating cavity with the energy recovery system enabled. As can be seen when the system is enabled the amount of power drawn by the cavity is significantly reduced [2]. The old beam then passes through cavity and is directed down an exit beam line into a beam dump.

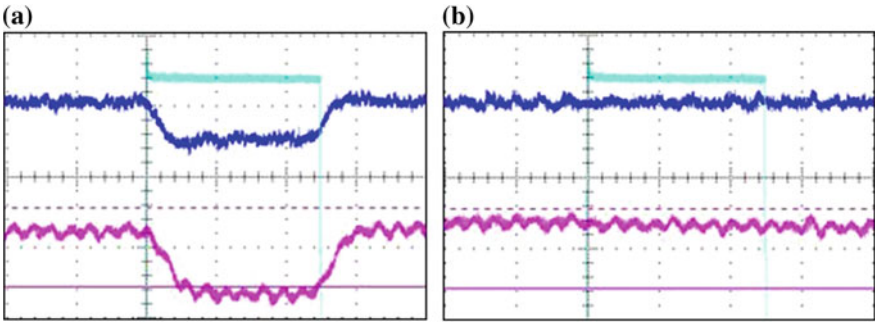

Fig. 3.5 Screen captures of from an oscilloscope showing the power draw (*y-axis*) from the main accelerating cavity for when **a** the energy recovery system is disabled and **b** when the energy recovery system is enabled

References

1. S. Physics, *Spitfire Pro User's Manual*, 330A Rev C, (2006)
2. STFC, ALICE Commisssionong, STFC, Dec 2008. [Online]. Available: http://www.stfc.ac.uk/ASTeC/Alice/36050.aspx. Accessed 2015

Chapter 4
Radiation Propagation Simulation

This chapter describes a simulation that was developed to aid the design and understanding of the optical setups presented in Chaps. 5–7. The simulation used diffraction theory to take an arbitrary two-dimensional electric field distribution and propagate it through a number of optical elements to a two-dimensional output plane at a given distance away. Information such as the spatial distribution and temporal properties of the propagated electric field could be obtained. The effect of optical elements such as lenses and diffraction gratings could be investigated and their various properties optimised to produce the maximum desired output parameters. A derivation of the physics involved in this simulation are provided along with the reasoning behind the assumptions made and any limits these assumptions impose upon the applicability of the simulation.

4.1 Introduction

A simulation for propagating two-dimensional (2D) (x, y) electric field amplitude grids over a distance z was created to help design optical setups for terahertz generation. This simulation was designed and implemented within MATLAB. Inputs to the simulation take the form of any arbitrary 2D electric field distribution with any arbitrary bandwidth and spectral profile. The outputs produced by the simulation include the three-dimensional (3D) electric field profile along with the spectral and temporal profile. Using this simulation it is possible to propagate the electric fields through a number of optical elements such as spherical and cylindrical lenses, diffraction gratings and other dispersive optical elements.

M.J. Cliffe, *Longitudinally Polarised Terahertz Radiation for Relativistic Particle Acceleration*, Springer Theses, DOI 10.1007/978-3-319-48643-7_4

4.2 Theory

The simulation has the following three main components: a linear propagation routine which describes the main propagation code which propagates an electric field, $E(x, y, 0)$, from an initial source plane to an final output plane $E(x, y, z)$; optical elements which describe how optical components such as lens, waveplates and gratings are added into the simulation and a longitudinal calculation which describes how the longitudinal fields are calculated from the propagated transverse fields.

4.2.1 Linear Propagation

The linear propagation section of the simulation was based on the Fresnel diffraction integral. The simulation takes an input electric field distribution grid,

$$f(x_i, y_i, z = 0, \omega) \tag{4.1}$$

and propagates it to form an electric field distribution on a grid

$$f(x_s, y_s, z, \omega). \tag{4.2}$$

The Fresnel diffraction integral is defined as [1]

$$f(x_s, y_s, z, \omega) = \frac{z}{i\lambda} \iint_{source} f(x_i, y_i, 0, \omega) \frac{e^{ikr}}{r^2} dx_i dy_i, \tag{4.3}$$

where (x_s, y_s) is the output grid, (x_i, y_i) is the input grid, $r = \sqrt{(x_s - x_i)^2 + (y_s - y_i)^2 + z^2}$, z is the propagation distance, λ is the wavelength of the radiation being propagated, k is the wavenumber and ω is the angular frequency. A pictorial description of Eq. (4.3) can be seen in Fig. 4.1. In this figure an element on the output plane can be seen as being dependent on every point from the input plane as is described by Eq. (4.3). Equation (4.3) can be simplified for some propagation systems such that the integral over the source plane is analogous to a Fourier transform of this plane. The assumptions and limits of such a simplification are discussed later in this section. This Fourier transform greatly increases the speed of the computation and so it is desirable to use it whenever possible.

In order to simplify Eq. (4.5) it is useful to define a new quantity R_s^2 which describes the projected distance from each input point to each output point and is described as:

$$R_s^2 = (x_s - x_i)^2 + (y_s - y_i)^2. \tag{4.4}$$

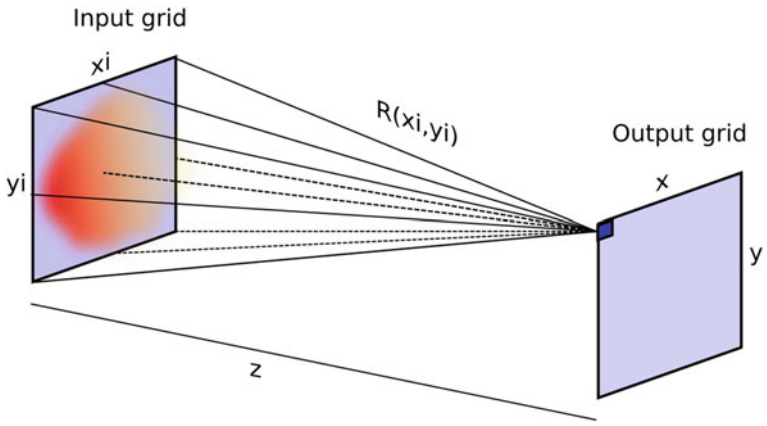

Fig. 4.1 Pictorial view of the Fresnel integral showing how a point on the output grid depends upon all the points from the input grid

It is then possible to redefine the Taylor expansion of r, which takes the form

$$r = z\left[1 + \frac{(x_s - x_i)^2 + (y_s - y_i)^2}{2z^2} - \frac{\left((x_s - x_i) + (y_s - y_i)^2\right)^2}{8z^4} + \cdots\right], \tag{4.5}$$

in terms of R_s^2, such that it becomes

$$r = z\left[1 + \frac{R_s^2}{2z^2} - \frac{R_s^4}{8z^4} + \cdots\right]. \tag{4.6}$$

In certain cases it is possible to negate the third order, and therefore any higher order, terms as long as they are much smaller than a complex exponential period such that

$$\frac{kR_s^4}{8z^4} \ll 2\pi, \tag{4.7}$$

If this condition is fulfilled then it is possible to remove the third, and any higher, order terms such that r can now be written as

$$r = z + \frac{R_s^2}{2z}. \tag{4.8}$$

A second simplification can also be made if it can be assumed that the propagation distance is much less than the wavelength of the radiation being propagated, $z \ll \lambda$. If this can be shown to be true then it is possible to say that $r \approx z$ and therefore Eq. (4.3) becomes

$$E(x_s, y_s, z, \omega) = \frac{e^{ikz}}{i\lambda z} \iint\limits_{source} E(x_i, y_i, 0, \omega) e^{\frac{ikR_s^2}{2z}} dx_i dy_i. \tag{4.9}$$

By expanding R_s in Eq. (4.9) an expression which takes the form

$$E(x_s, y_s, z, \omega) = \frac{e^{ikz}}{i\lambda z} \iint\limits_{source} E(x_i, y_i 0, \omega) e^{\frac{ik}{2z}\left(x_i^2 + y_i^2\right)} e^{\frac{ik}{2z}\left(x_s^2 + y_s^2\right)} e^{-\frac{ik}{z}(x_i x_s + y_i y_s)} dx_i dy_i, \tag{4.10}$$

is obtained.

By examining this expression it is now possible to see that many of the terms inside the integral no longer depend on x_i or y_i. It is therefore possible to remove these terms from the integral, leaving

$$E(x_s, y_s, z, \omega) = \frac{e^{ikz}}{i\lambda z} e^{\frac{ik}{2z}\left(x_s^2 + y_s^2\right)} \iint\limits_{source} E(x_i, y_i, 0, \omega) e^{\frac{ik}{2z}\left(x_i^2 + y_i^2\right)} e^{-\frac{ik}{z}(x_s x_i + y_s y_i)} dx_i dy_i. \tag{4.11}$$

This expression now allows us to take a two-dimensional electric field map, $E(x_\mathrm{i}, y_\mathrm{i})$ at a position $z = 0$ and angular frequency ω and propagate it to a plane a distance z away. This produces an electric field map $E(x_\mathrm{s}, y_\mathrm{s})$ at position $z = z$ and angular frequency ω.

4.2.2 Focusing Beams

Focusing is an important part of this simulation and must therefore be modelled within the propagation. Consider a collimated beam of radiation incident upon a lens, as shown in Fig. 4.2, with focal length f. Sections of the beam which exist at

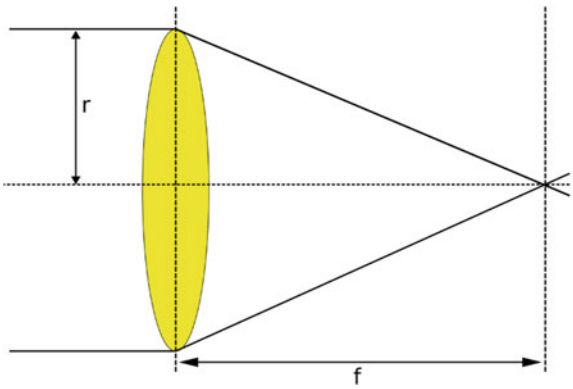

Fig. 4.2 Diagram showing a collimated beam incident upon a biconvex lens with focal length f

different transverse locations will travel through different thickness of the lens material. This will cause the beam to come to a focus at a position $z = f$. In order to simulate the effect of focusing, a radially dependent phase delay is imposed upon the source plane such that the new source plane becomes

$$E_{in}(x_i, y_i, \omega) = E(x_i, y_i)\mathrm{e}^{i\Phi(x_i, y_i, \omega)}, \tag{4.12}$$

where $E(x_\mathrm{i}, y_\mathrm{i})$ is the input electric field distribution and $\Phi(x_\mathrm{i}, y_\mathrm{i}, \omega)$ is the phase delay as a function of input grid position and angular frequency [1]. The electric field distribution is not frequency-dependent as it is assumed that the input beam is collimated and therefore all frequencies have the same spatial profile. It is however contained within the phase delay as a relative path length travelled through the material depends upon the refractive index, which in turn is a function of frequency. This effectively adds a time delay onto the input grid as a function of input grid position. To calculate the phase delay as a function of position it is first useful to define it in terms of the extra thickness the beam will propagate through due to the lens and the refractive index

$$\Phi(x_i, y_i, \omega) = \delta k D(x_i, y_i). \tag{4.13}$$

Here δk represents the difference in wavenumber inside and outside the lens due to the refractive index difference and can be defined as $\delta k = n_\mathrm{i} k - k$ where k is the wavenumber and n is the refractive index inside the lens. $D(x_\mathrm{i}, y_\mathrm{i})$ is the extra thickness travelled through the material as a function of position. Using these definitions and Eq. (4.13) it is possible to write

$$\Phi(x_i, y_i, \omega) = (nk - k)D(x_i, y_i). \tag{4.14}$$

As well as redefining δk it is also possible to redefine $D(x_\mathrm{i}, y_\mathrm{i})$ and write it as a function of the radius

$$D(x_i, y_i) = 2\left(\sqrt{R_c^2 - r^2} - \sqrt{R_c^2 - r_0^2}\right), \tag{4.15}$$

where R_c is the radius of curvature, r is the position on the input grid as defined by $\sqrt{x^2 + y^2}$ and r_0 is the radius of the lens. Assuming a thin lens approximation it is possible to say that $R_c \gg r_0$ such that Eq. (4.15) becomes

$$D(x_i, y_i) = \frac{r_0^2 r^2}{R_C}. \tag{4.16}$$

Using Eq. (4.16) and placing it into Eq. (4.14) it is possible to write

$$\Phi(x_i, y_i, \omega) = \frac{k(n-1)\left(r_0^2 - r^2\right)}{R_C}. \tag{4.17}$$

It is generally more useful to think in terms of focal length, f, as opposed to the radius of curvature, therefore by using the relationship between f and R_C

$$f = \frac{R_c}{2(n-1)}, \tag{4.18}$$

it is possible to express $\Phi(x_i, y_i, \omega)$ in terms of focal length as

$$\Phi(x_i, y_i, \omega) = \frac{k}{2f}\left(r_0^2 - r^2\right). \tag{4.19}$$

Notice that r_0 is a constant with respect to its position on the input grid. It therefore adds a constant phase delay onto the whole beam and will not affect the focusing. It can therefore be neglected leaving

$$\Phi(x_i, y_i, \omega) = -\frac{k}{2f}r^2. \tag{4.20}$$

By substituting Eq. (4.20) into Eq. (4.12) it is now possible to add a focusing effect into the simulation. The new input plane therefore becomes

$$E_{in}(x_i, y_i, \omega) = E(x_i, y_i)\mathrm{e}^{-\frac{ik}{2f}r^2}. \tag{4.21}$$

The effect of this radially varying phase delay can be seen in Fig. 4.3. Figure 4.3a shows an input plane that does not have the radially varying phase delay imposed and Fig. 4.3b shows the same input plane but with a radially varying

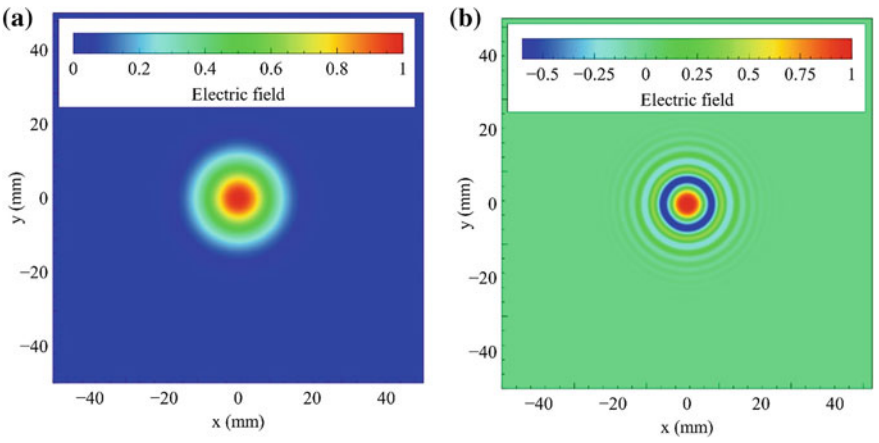

Fig. 4.3 Simulated Gaussian input beams of frequency 0.5 THz, **a** shows the input plane with no focusing whilst **b** shows the electric field input plane with a radially varying phase delay that mimics the focusing effect of a 75 mm lens as calculated from Eq. (4.21)

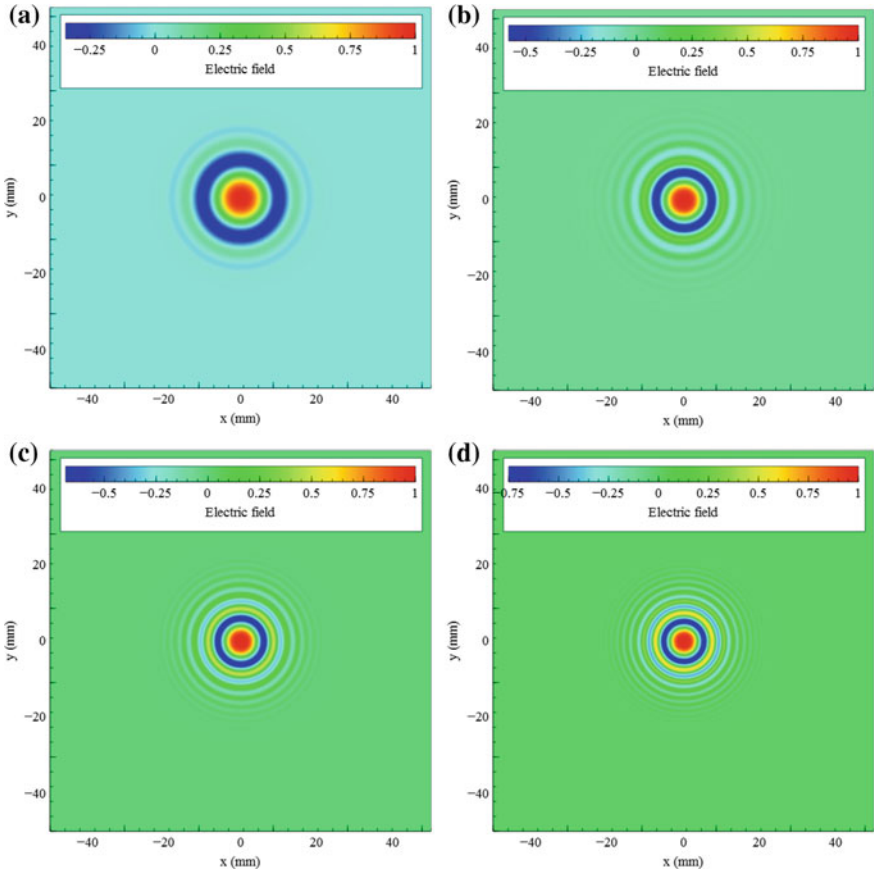

Fig. 4.4 Gaussian electric field input planes calculated from Eq. (4.21) displaying the focusing effect for frequencies. **a** 0.2 THz, **b** 0.4 THz, **c** 0.6 THz and **d** 0.8 THz

phase delay. In this figure both beams have a frequency of 0.5 THz and the focusing effect mimics that of a 75 mm lens.

The radially varying oscillation which is seen in Fig. 4.3b as negative and positive annular rings superimposed onto the input Gaussian give rise to the focusing effect of the beam when propagated. This radially varying oscillation depends upon both the focal length and the frequency of the input wave as described in Eq. (4.21). Figure 4.4 shows how this radially varying oscillation period changes and gets shorter as the frequency of the beam increases. This implies that the beam focuses to a smaller spot at higher frequencies. This effect is expected as radiation with higher frequencies and hence longer wavelengths have smaller diffraction-limited spot sizes.

By propagating these input planes over a range of z such that $z = f \pm \delta z$ where f is the focal length and $2\delta z$ is the propagation range the effects of focusing can be

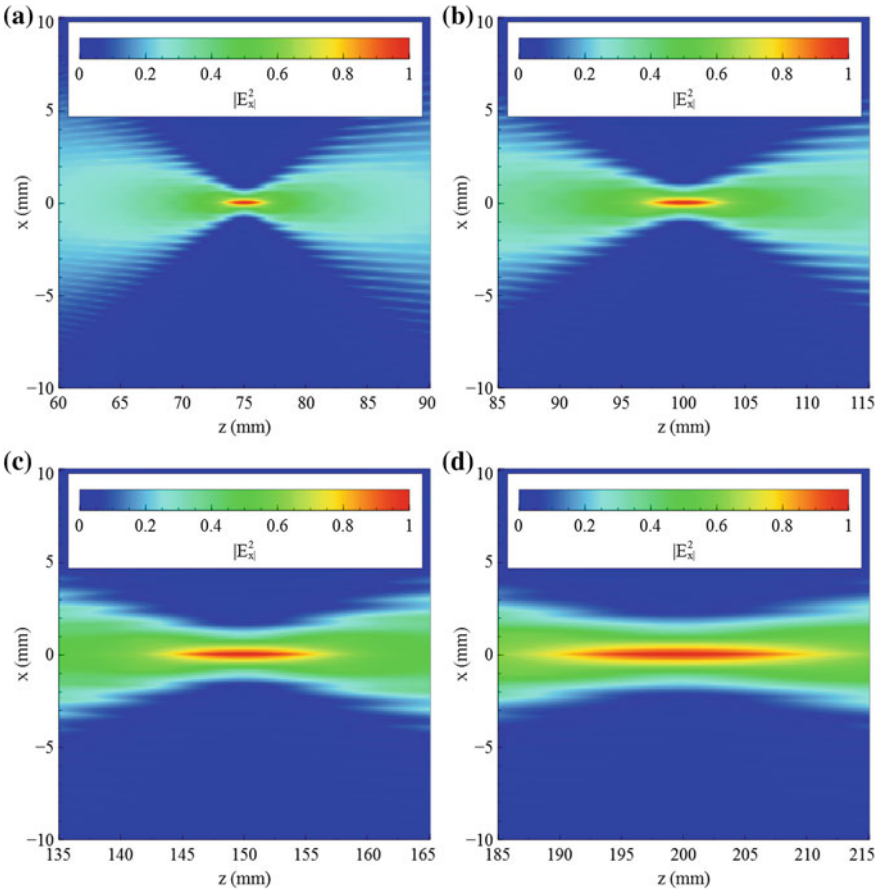

Fig. 4.5 Simulated modulus of the electric field squared of propagated Gaussian beams of single frequency, using Eq. (4.11), with different focal lengths. **a** $f = 75$ mm, **b** $f = 100$ mm, **c** $f = 150$ mm and **d** $f = 200$ mm. All results are normalised to their local maxima and are propagated from the same input plane

easily seen. Figure 4.5 shows this effect for a single frequency of 0.5 THz and varying focal lengths. A single frequency beam was chosen to display this effect as it enables the full shape of the propagating beam to be displayed as if it were a continuous wave beam. All of the data in this figure were normalised to the maxima of the individual data sets. As can be seen all the beams focus to their expected positions, which is at a location of $z = f$. Shorter focal lengths produced smaller transverse spot sizes at their focal positions but the rate of change of the beam diameter changes more rapidly as a function of z; this is expected and predicted by Gaussian optics.

4.2.3 Adding a Bandwidth

Whilst Eq. (4.11) allows the propagation of an electric field distribution over a distance z it does so only for an individual frequency. For this simulation to provide useful results pulsed radiation must also be simulated. In order to do this a bandwidth or spectral range must be introduced. The temporal shape of a pulse is related to its spectral bandwidth through

$$E(x_s, y_s, z = 0, t) = \int_{-\infty}^{\infty} B(\omega) E(x_s, y_s, z = 0, \omega) \mathrm{e}^{i\omega t} d\omega, \tag{4.22}$$

where $E(x_s, y_s, z = 0, \omega)$ is the normalised electric field in the frequency domain, t is a temporal offset, $E(x_s, y_s, z = 0, t)$ is the electric field in the time domain and $B(\omega)$ is a bandwidth-shaping function.

By performing the linear propagation routine, Eq. (4.11), for a range of angular frequencies and summing over all frequencies as described in Eq. (4.22) it is possible to obtain a result which describes the propagation of pulsed radiation. As Eq. (4.22) is analogous to a Fourier transform the shape of the temporal profile will take the form of the Fourier transform of the spectral shape. For that reason the bandwidth-shaping function is added as this allows for the electric field at each frequency to be weighted with respect to the electric field at other frequencies hence changing the spectral distribution of the pulse. The bandwidth-shaping function is chosen to take the form

$$B(\omega) = \omega^2 \mathrm{e}^{\frac{-\omega^2}{A^2}} \tag{4.23}$$

where ω is the angular frequency and A is a constant which can be tuned to help match the propagated spectrum to real world results.

If the bandwidth-shaping function were not applied then the spectral shape of the input electric field would contain sharp cut-offs. This leads to a distorted, unrealistic temporal profile that does not mimic the profile of the terahertz radiation that is being simulated. This can be shown by taking a radiation source with a 3 THz bandwidth, not applying the bandwidth-shaping function, Fig. 4.6a, and examining the corresponding temporal profile, shown in Fig. 4.6b. As can be seen the temporal profile looks distorted and contains temporal oscillations before and after the pulse, a direct result of Fourier transforming the sharp edge shown in the spectrum.

Taking the same parameters but adding in the bandwidth-shaping function allows for a much more realistic propagation result as can be seen in Fig. 4.7. Figure 4.7 shows the spectral and temporal shape of the propagated pulse with the bandwidth shaping

function applied. For the data shown in Fig. 4.7 A was initially set to 0.1 and in order to compare how sensitive the spectral and temporal profiles were to variations of A, pulses were then propagated with a range of A values. These data can be seen

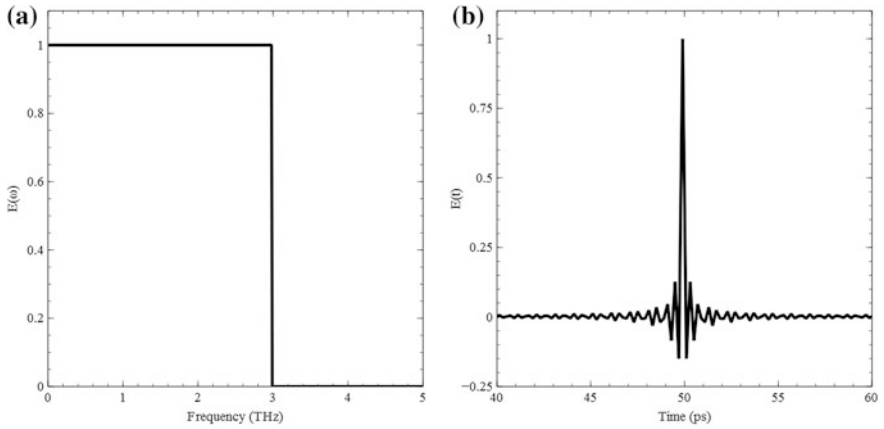

Fig. 4.6 **a** Spectral and **b** temporal electric field profiles for a 3 THz bandwidth radiation source with no spectral shaping applied

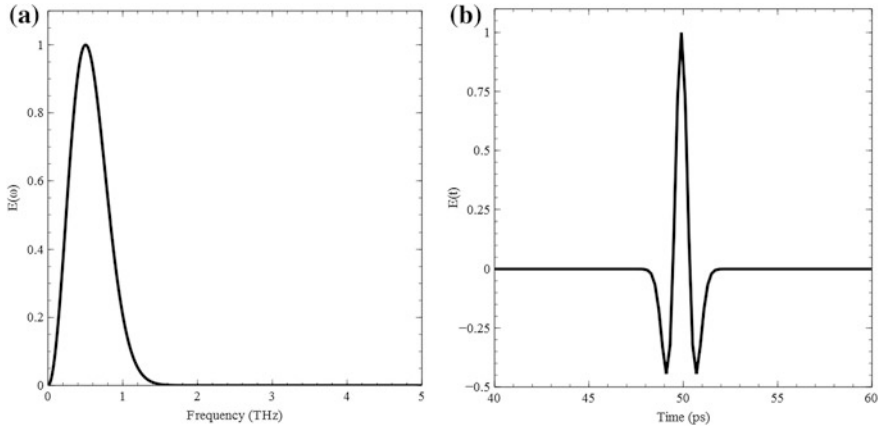

Fig. 4.7 Simulated (**a**) spectral and (**b**) temporal profiles of a 3 THz bandwidth electric field with the bandwidth-shaping function applied

in Fig. 4.8. As these plots show both the spectral width and spectral centre can be tuned. As the spectral width is increased the temporal duration is reduced. By tuning this value it is possible to choose a spectrum that corresponds to a pulse with the desired temporal profile.

Performing the propagation of and sum over multiple frequencies produces a result with a pulse-like structure as seen in Fig. 4.9. Here a Gaussian beam with an initial $1/e^2$ waist of 15 mm was propagated through a 75 mm lens. A bandwidth of 0.3–1 THz was used for this calculation with a spectral bandwidth-shaping A value of 2. The spectral shape can be seen in the inset graph of Fig. 4.9. As can be seen

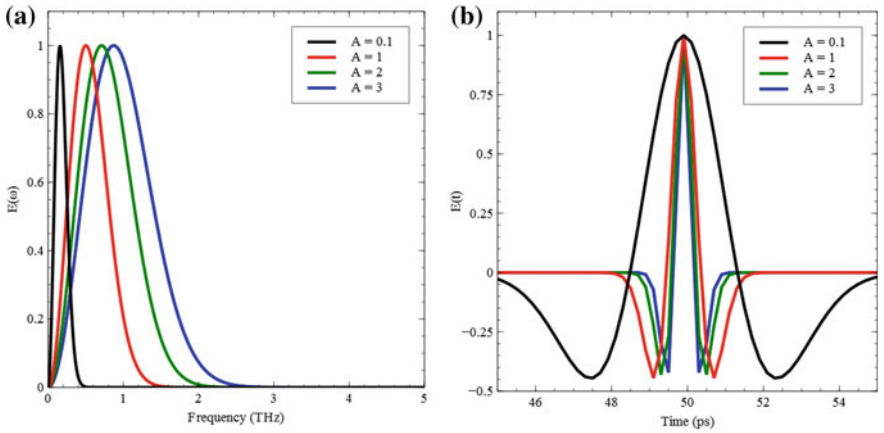

Fig. 4.8 **a** Spectral and **b** temporal profiles of 3 THz bandwidth electric fields with the bandwidth-shaping function applied as a function of A

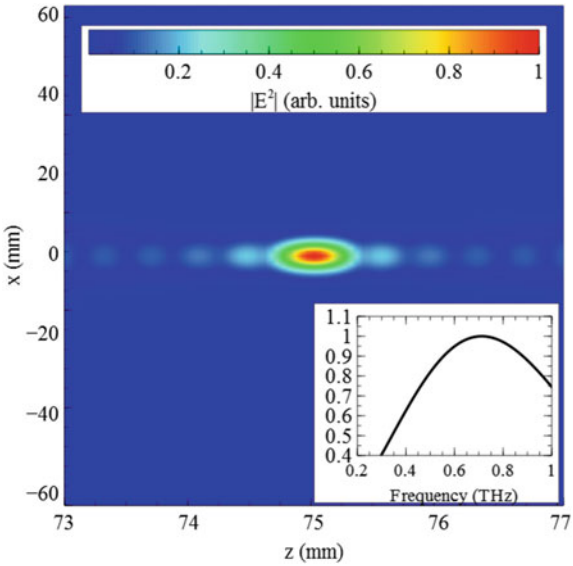

Fig. 4.9 Simulated propagated electric field intensity focused with a simulated 75 mm focal length lens and a bandwidth of 0.3–1 THz. Inset plot shows the spectral bandwidth used along with the spectral shape

the pulse only exits longitudinally around the focal plane. Oscillations that exist at positive and negative z values around the main pulse are mathematical artefacts that are due to the discretisation of the frequency array. These can be minimised by using a finer bandwidth array with more points; however this results in a slower calculation and more input planes have to be propagated.

4.2.4 Adding Complex Input Beams

To simulate cases that are useful for this project complex input beams must be considered, for instance two cases that are of particular use are the co-propagation of multiple beams and the propagation of complex modes such as the Laguerre-Gaussian 01 mode. In the case of the co-propagation of multiple beams the input plane is set such that two Gaussian profiles with spatial offsets are added together,

$$E_{in} = E_0\left[\mathrm{e}^{\frac{-(x_i-x_0)^2}{2\sigma_{x_0}^2}} + \mathrm{e}^{\frac{-(y-y_0)^2}{2\sigma_{y_0}^2}}\right] + E_1\left[\mathrm{e}^{\frac{-(x_i-x_1)^2}{2\sigma_{x_1}^2}} + \mathrm{e}^{-\frac{(x_i-x_1)^2}{2\sigma_{x_1}^2}}\right], \tag{4.24}$$

where σ_{n_x} represents the $\frac{1}{e^2}$ width of beam number x in dimension n. It is possible to vary the relative polarity of the beams by adjusting the sign of E_n. By adjusting the values of σ_{n_x} and n_x, which represent the width and offset respectively, it is possible to simulate to beams with a variety of shapes and sizes. Figure 4.10 shows the input plane for various beam sizes and spatial offsets. The beams have opposite polarities. All of the input beams shown in Fig. 4.10 have the same pulse energies as can be seen by showing that the spatial integral of the electric fields for all the pulses are equal, such that

$$C = \int\int E_1 dxdy = \int\int E_2 dxdy = \int\int E_3 dxdy = \int\int E_4 dxdy \tag{4.25}$$

holds true for all the electric fields shown, where C is an arbitrary constant value.

When propagated these input planes display different characteristics and shapes as expected. These plots can be seen in Fig. 4.11, where the input planes have been propagated through a lens of focal length 75 mm to a z distance of 75 mm. The same bandwidth and bandwidth shaping function employed in Fig. 4.9 have been used. Input planes which provide a larger numerical aperture focus to smaller spot size and have a smaller Rayleigh range. Again the oscillations in front of and behind the main pulse are numerical artefacts due to the discretisation of the frequency array. Figure 4.11 shows the absolute value of the electric field squared; this removes any phase information from the beam and only shows the envelope of the field. In order to view the phase information the real part of the propagated function must be plotted. Plots with the phase information shown can be seen in Fig. 4.12. Here the positive values represent the field pointing in the positive x direction whereas the negative values represent the field pointing in the negative x direction. As can be seen in these images the polarity flip imposed upon the input plane remains in the propagated beam. This is expected and important when trying to create a beam with a strong transverse gradient.

As well as multiple Gaussian input beams other more complex modes can also be propagated using this simulation. One such mode that is of particular interest to this work is the Laguerre-Gaussian 01 mode. This mode is commonly referred to as a radially polarised beam as the transversely polarised component of such a mode

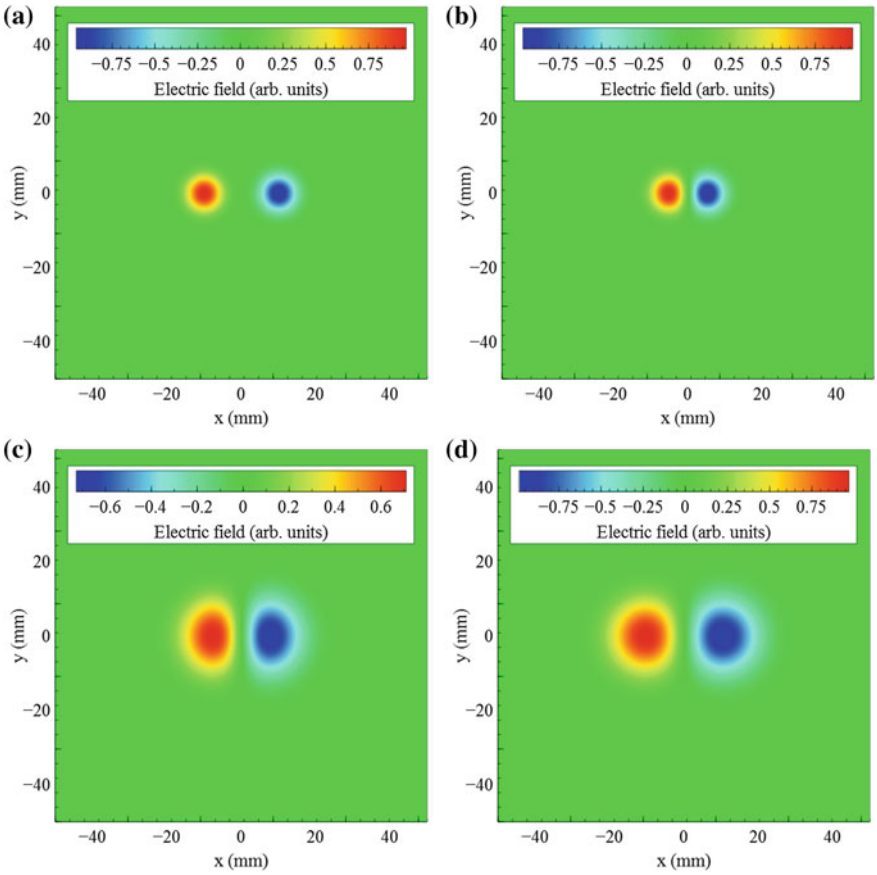

Fig. 4.10 Calculations of various input electric fields showing two Gaussian beams of opposite polarity with various size and offset properties **a** $\sigma = 5$ mm $x_o = 10$ mm, **b** $\sigma = 5$ mm $x_o = 5$ mm, **c** $\sigma = 10$ mm $x_o = 5$ mm, **d** $\sigma = 10$ mm $x_o = 10$ mm

always points in the direction of the radius and the beam as a whole is radially symmetrical. A general Laguerre-Gaussian beam can be described as

$$E(r, \phi, z) = \frac{CL}{\omega(z)} \left(\frac{r\sqrt{2}}{\omega(z)} \right)^{|l|} e^{-\frac{r^2}{\omega^2(z)}} e^{-\frac{ikr^2}{2R(z)}} e^{il\phi} e^{-[i(2p+|l|+1)\zeta(z)]}, \tag{4.26}$$

where $E(r, \phi, z)$ is the electric field distribution in cylindrical co-ordinates [2]. Cylindrical co-ordinates are useful to describe a Laguerre-Gaussian mode as it is symmetric in this frame. C and L are constants for each mode number, $\omega(z)$ is the beam waist at position z, $R(z)$ is the radius of curvature and $\zeta(z)$ is the Gouy phase

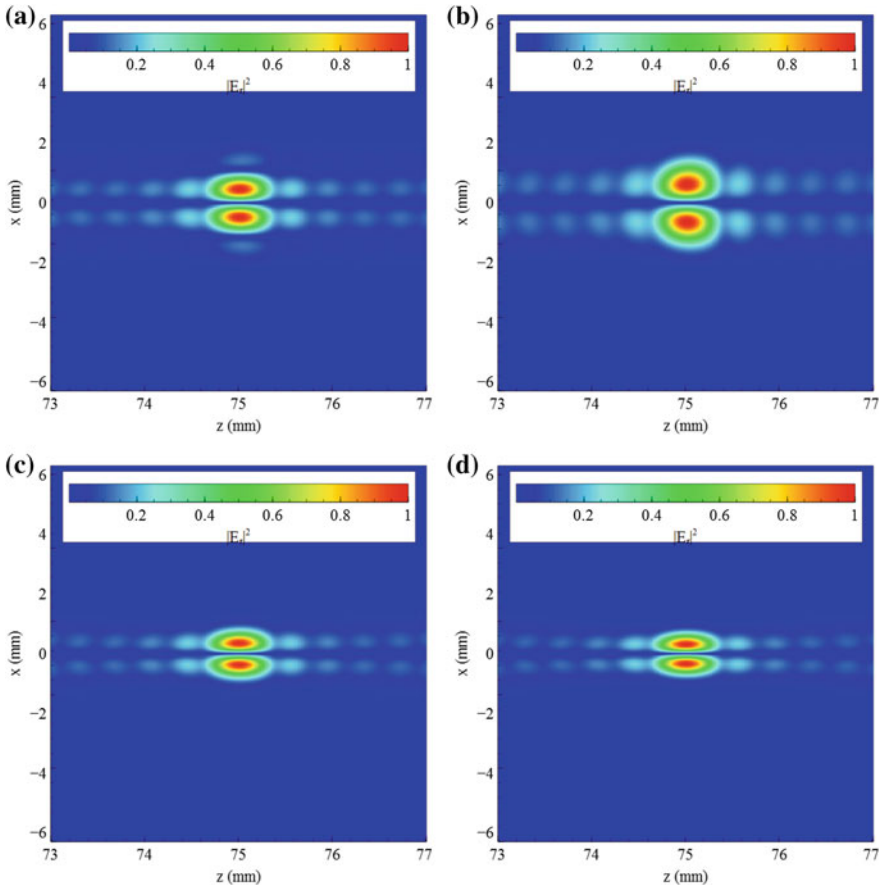

Fig. 4.11 Squared moduli of the propagated electric fields after passing through a lens with a focal length of 75 mm. **a** $\sigma = 5$ mm $x_o = 10$ mm, **b** $\sigma = 5$ mm $x_o = 5$ mm, **c** $\sigma = 10$ mm $x_o = 5$ mm, **d** $\sigma = 10$ mm $x_o = 10$ mm where σ is the e^{-2} width of the beam and x_0 is the distance between the two beams

shift term. Using Eq. (4.26) it is possible to create a radially polarised two-dimensional input field that takes the form [2, 3]

$$E(r, \phi, z) = \frac{1}{\omega(z)} e^{\frac{r^2}{\omega(z)^2}} \left(\frac{2r^2}{\omega(z)^2} \right) e^{i\phi} e^{-2i\zeta(z)}. \tag{4.27}$$

Notice that this represents a field distribution which is polarised in the radial dimension whereas the simulation described above requires a field polarised in either x or y. In order to make this compatible with the simulation the distribution is

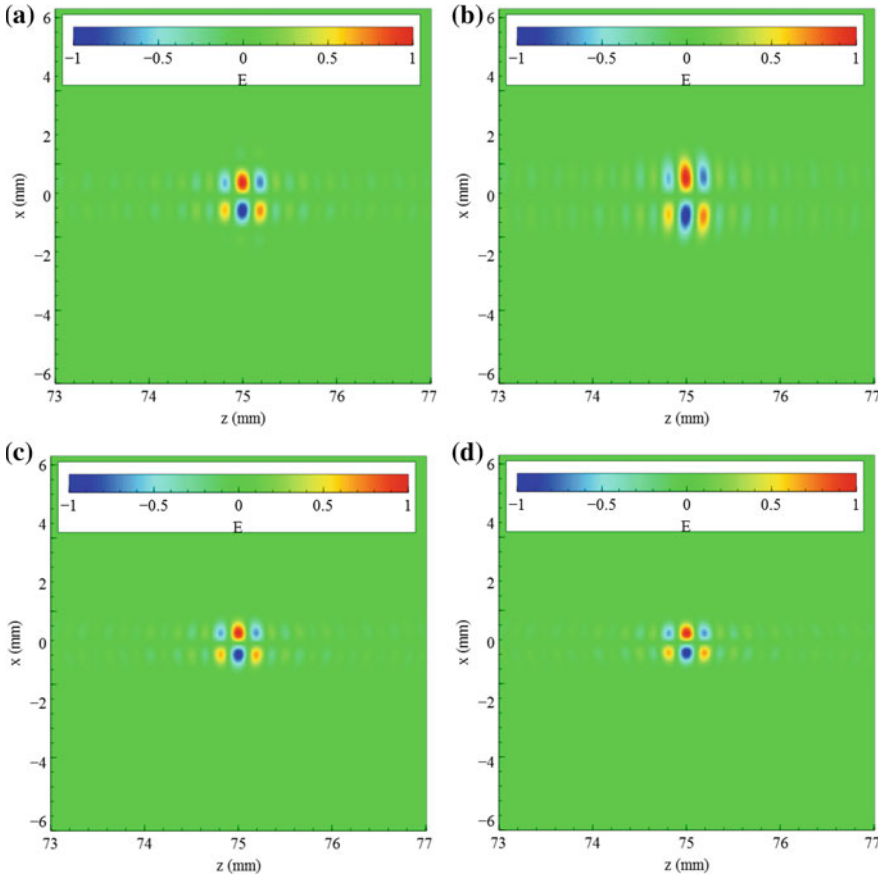

Fig. 4.12 Propagated electric fields shown in Fig. 4.1 with the phase information for each beam included. **a** $\sigma = 5$ mm $x_o = 10$ mm, **b** $\sigma = 5$ mm $x_o = 5$ mm, **c** $\sigma = 10$ mm $x_o = 5$ mm, **d** $\sigma = 10$ mm $x_o = 10$ mm

resolved into its two linearly polarised components. Each polarisation component is then propagated separately and then recombined once propagated to form the resultant beam. The two input planes, one for the x-polarised and one for the y-polarised component, can be seen in Fig. 4.13. These input planes once propagated using the same spectral properties and focal lengths as used above can be seen in Fig. 4.14. Figure 4.14a shows a propagated Laguerre-Gaussian 01 beam with an input waist of 10 mm whilst Fig. 4.14b shows the same beam propagated but with a 20 mm waist. As can be seen the beam with the larger initial spot size focuses to a tighter waist.

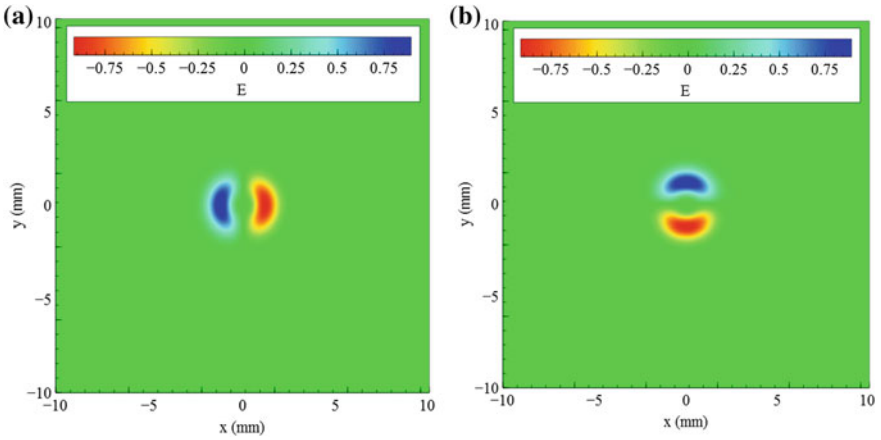

Fig. 4.13 Input electric field distribution as a function of x and y for a Laguerre-Gaussian 01 mode showing the x-polarised (**a**) and y-polarised (**b**) components

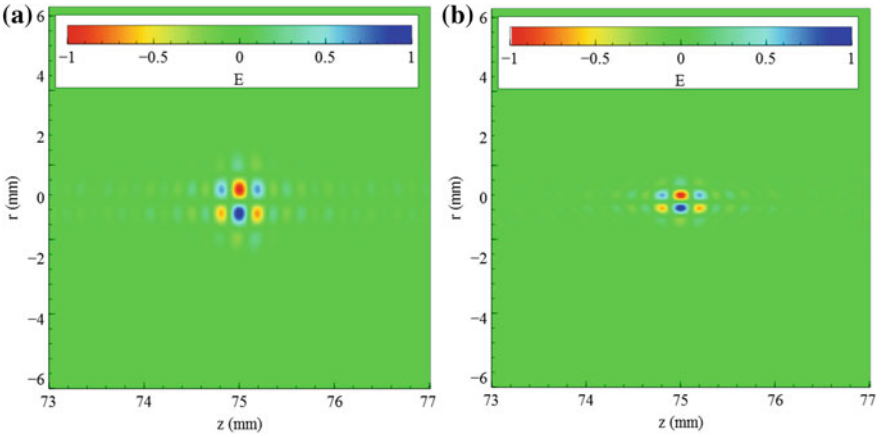

Fig. 4.14 Propagated electric fields of the Laguerre-Gaussian 01 mode with different input transverse sizes. **a** 10 mm and **b** 20 mm. Both figures show the focusing with a 75 mm focal length lens

4.3 Calculating the Longitudinal Component

The propagation simulation propagates an electric field component over a distance z, it was chosen to propagate a transversely polarised component. However the longitudinal component is also important and so must be calculated from the transverse field component. The longitudinal field, $E_z(x, y, z)$, is related to the transverse field, $E_r(x, y, z)$, through Maxwell's divergence equation

$$\nabla \cdot \bar{E}(x, y, z) = 0, \tag{4.28}$$

where

$$\nabla = \left(\bar{x} \frac{\partial}{\partial x} + \bar{y} \frac{\partial}{\partial y} + \bar{z} \frac{\partial}{\partial z} \right) \tag{4.29}$$

and

$$\bar{E}(x, y, z) = E_z(x, y, z) + E_x(x, y, z) + E_y(x, y, z). \tag{4.30}$$

Splitting Eq. (4.28) into its vector components yields

$$\left(\frac{\partial}{\partial x} E_x(x, y, z) + \frac{\partial}{\partial y} E_y(x, y, z) + \frac{\partial}{\partial z} E_z(x, y, z) \right) = 0. \tag{4.31}$$

Combining the transverse field components, $E_x(x, y, z)$ and $E_y(x, y, z)$, into a single variable $E_r(x, y, z)$ and defining $\nabla_\perp = \frac{\partial}{\partial x} + \frac{\partial}{\partial y}$ yields

$$\frac{\partial}{\partial z} E_z(x, y, z) + \nabla_\perp E_r(x, y, z) = 0, \tag{4.32}$$

which when rearranged and integrated over z gives

$$E_z(x, y, z) = - \int_{z=0}^{z} \nabla_\perp E_r(x, y, z) dz + \zeta(\mathrm{x}, \mathrm{y}), \tag{4.33}$$

where $\zeta(x, y)$ is a constant of integration that does not depend upon z. As this simulation typically deals with pulsed radiation $\zeta(x, y)$ can be said to be zero. For pulsed radiation there are places in z where every field component, including E_z, is equal to zero. At these points $\zeta(x, y)$ must also equal zero, and because it does not vary in z it must also be $0 \, \forall \, z$. This now leaves a final expression which can be used to calculate the longitudinal electric field from the transverse electric field

$$E_z(x, y, z) = - \int_{0}^{z} \nabla_\perp E_r(x, y, z) dz. \tag{4.34}$$

As the simulation produces outputs that take the form $E_x(x, y, z)$ and $E_y(x, y, z)$, Eq. (4.34) must be converted such that it is compatible with the simulation. To do this the equation is discretised, such that the continuous integration over space becomes a discrete sum over the elements, and converted into a summation such that

$$E_z(x, y, z) = - \sum_{n=1}^{\infty} \left[\frac{\partial}{\partial x} E_x(x, y, z_n) + \frac{\partial}{\partial y} E_y(x, y, z_n) \right]. \tag{4.35}$$

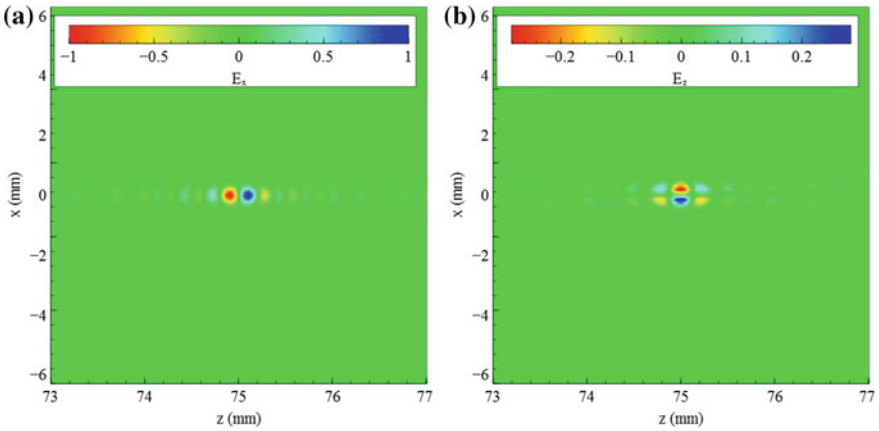

Fig. 4.15 **a** Propagated transversely-polarised electric field from a Gaussian beam propagated through a lens $f = 75$ mm. **b** The corresponding longitudinal field

Using this expression to calculate the longitudinal field produced by a propagated transverse field yields the results shown in Fig. 4.15. Here a Gaussian transversely polarised input plane has been propagated through a 75 mm lens and its corresponding longitudinal field calculated. As can be seen the longitudinal field exists at spatial locations where the transverse field exhibits a gradient. The same calculation can be performed for any input plane, for instance Fig. 4.16 shows the longitudinal field produced for an input plane of two Gaussians with a 10 mm horizontal offset and 20 mm width and the same propagation values. As can be seen in this figure the longitudinal field is much higher as the transverse gradient is much larger in the centre. It also exists on axis where the transverse gradient is strongest.

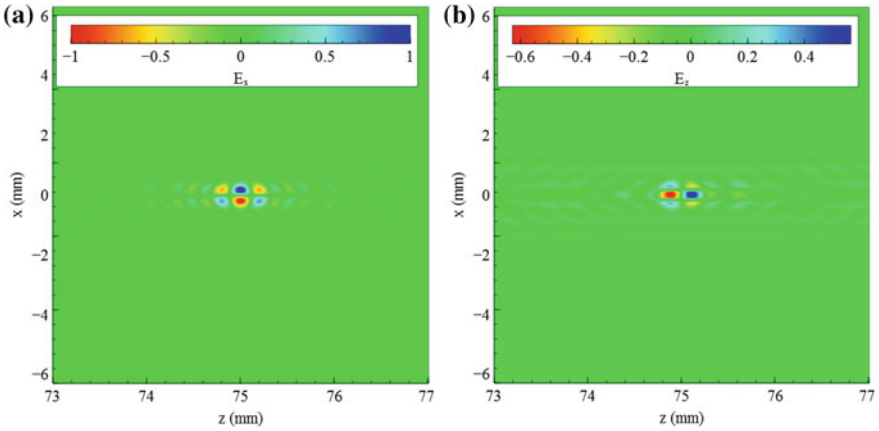

Fig. 4.16 **a** Propagated transversely-polarised electric fields from two Gaussian beams of opposite polarity propagated through a lens of $f = 75$ mm. **b** The corresponding longitudinal field

4.4 Simulation Structure

In order to write a simulation which propagated electromagnetic radiation as described above the mathematics had to be converted into MATLAB code. A description as to how this was done can be seen in Appendix A.2. A flow chart showing how the code operated can be seen in Fig. 4.17. Here the data flow is

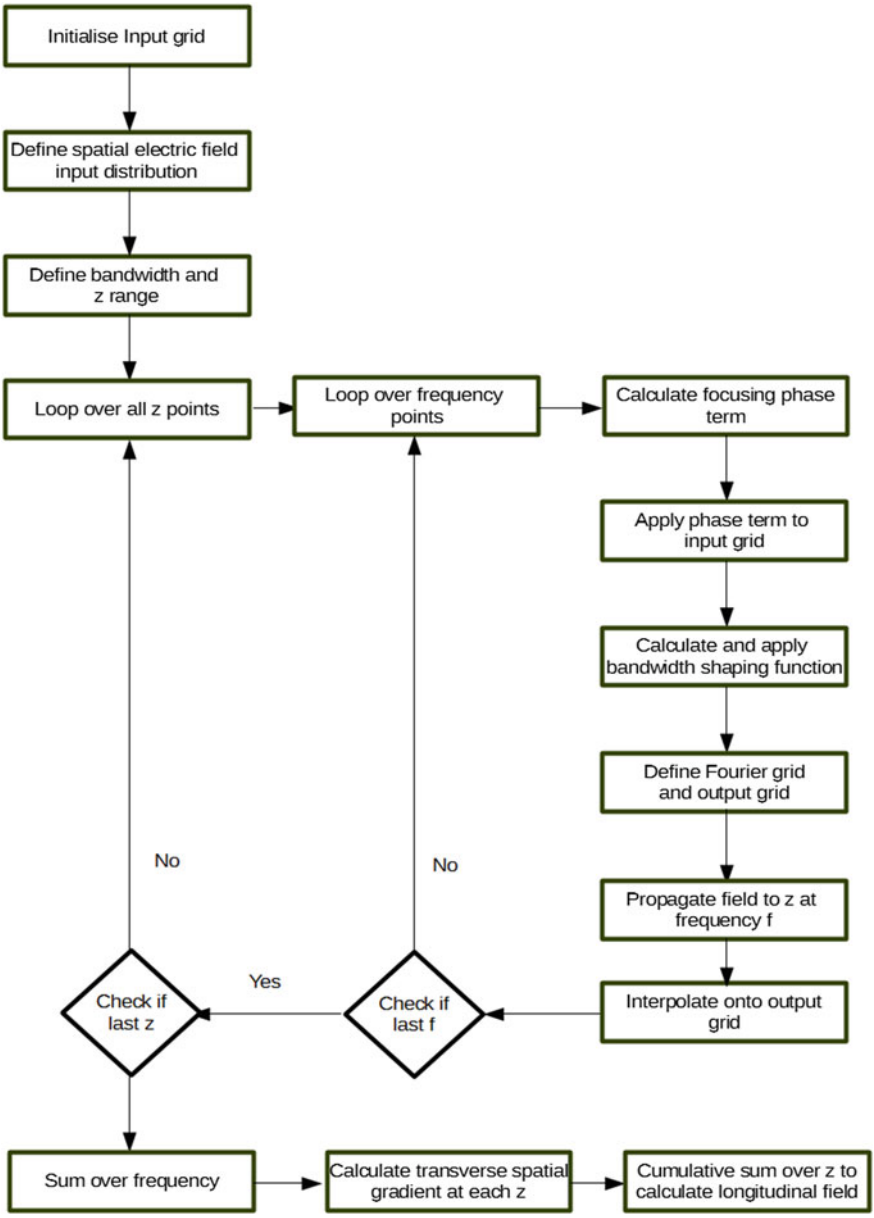

Fig. 4.17 Flow chart showing the organisational flow of the simulation

shown as well as any major operations performed. Decisions are also shown and defined as well as any outputs provided by the simulation. In Fig. 4.17 it is possible to see how all the inputs, such as electric field profile and bandwidth, are entered into first the *z-range* loop which internally contains the bandwidth loop. The order in which different calculations are performed within this group can also be seen, i.e. calculating the focusing phase term, calculating the bandwidth-shaping function etc. The order in which external operations performed, such as summing over the frequency components and calculating the longitudinal electric field from the transverse, can also be seen.

4.5 Simulation Applications

The radiation propagation simulation has many potential applications. In this work it has been applied to support a number of experiments including the design of terahertz propagation optics and the generation of strong longitudinally polarised terahertz electric fields. The first application of this simulation was to compare the longitudinal to transverse field ratios for different input planes. The aim was to help design a system to maximise the longitudinal field for a given radiation source. The most common mode that is used when attempting to generate a longitudinally polarised field component is the Laguerre-Gaussian 01 mode. This is because it has strong transverse field gradients in the centre which maximise the field component orientated in the longitudinal direction. When designing a source to generate a longitudinally polarised field component it is therefore useful to compare such a source to the longitudinally polarised field component generated by a comparable Laguerre-Gaussian 01 mode. Figure 4.18 shows the calculated peak longitudinal to transverse field ratios for a two Gaussian beam input (TG), as described in Sect. 4.2.4, and a Laguerre-Gaussian 01 beam input for a number of focal lengths ranging from 75 to 300 mm. The red points on the plot represent the peak longitudinal to peak transverse field ratios for a Laguerre-Gaussian 01 beam whilst the black points show the same data taken for a TG input. A reciprocal focal length fit has been applied to both data sets which provides a good match to the data points obtained from the simulation. The errors in the focal length dimension have been taken as systematic errors derived from the discretisation of z in the simulation. As can be seen from Fig. 4.18 the Laguerre-Gaussian 01 beam produces field components which much higher longitudinal to transverse ratios than the TG beam input, however the TG beam input is still able to produce longitudinal fields with 40% of the peak transverse fields when focused tightly by a 75 mm lens. The exact values in this figure are specific to the exact input parameters such as beam input size and as such should only be used to compare beams of comparable input sizes.

As well as comparing different beam modes this simulation can also be used to compare beams of the same mode with different parameters such as spot size, separation and bandwidth. Figure 4.19 shows TG input planes propagated through

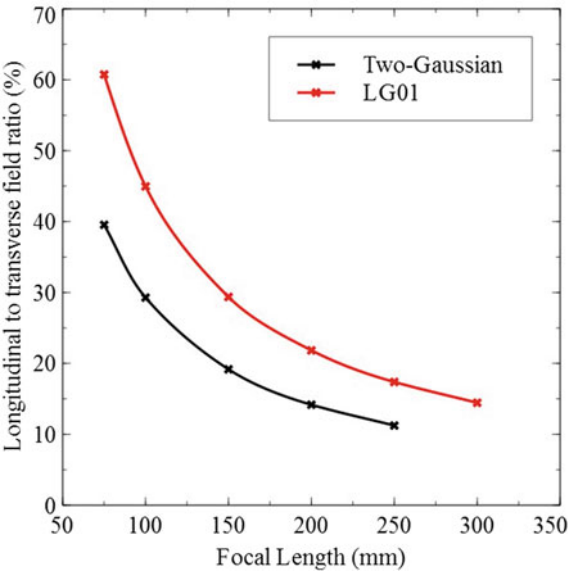

Fig. 4.18 Longitudinal to transverse field ratio versus focal length for various input modes (*red*) Laguerre-Gaussian 01 mode and (*black*) TG input

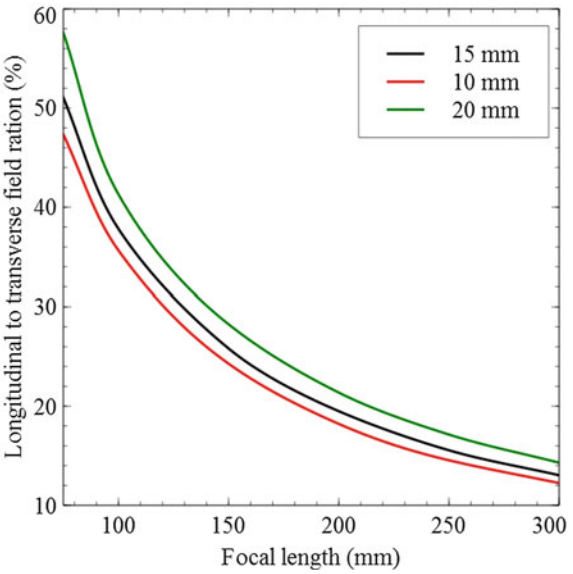

Fig. 4.19 Longitudinal to transverse field ratios as function of focal length for a variety of TG input beam sizes, in each of these plots both of the Gaussian input beams have the same size

different lenses of varying focal lengths. This figure shows the focusing of beams with varying separation (10, 15 and 20 mm) and compares how the input separation affects the longitudinal to transverse field ratio. The spot size and bandwidth remained constant within this figure, with each spot having an e^{-2} width of 15 mm. As can be seen there is a $1/f$ trend throughout all the data presented above and the

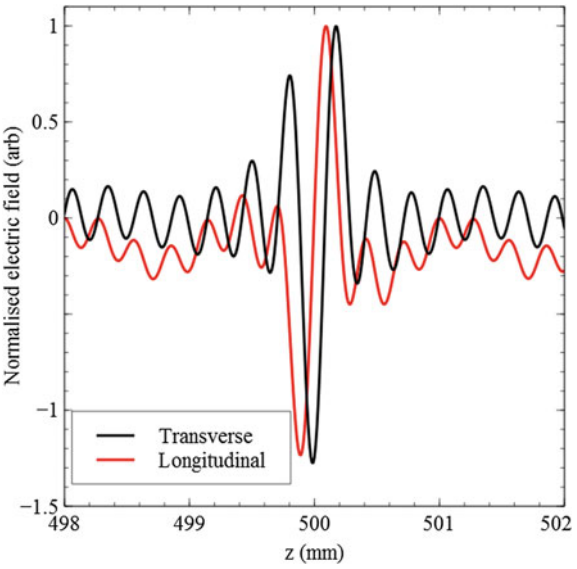

Fig. 4.20 Longitudinal spatial profile comparison of the longitudinal (*red*) and transverse (*black*) field components for a focused TG input plane with a focal length of 500 mm, a spatial offset of 10 mm and a Gaussian width of 15 mm

longitudinal to transverse field ratio varies inversely with the focal length. As expected the larger the input separation the stronger the focusing and so the higher the longitudinal to transverse field ratio.

Longitudinal and transverse spatial profiles of both the transverse and longitudinal polarisation states can also be investigated and analysed. Figure 4.21 shows spatial profiles of the longitudinal and transverse electric field components taken at at a longitudinal position of $z = f$. Figure 4.21c shows line outs taken from a propagated TG input plane through a 300 mm focal length lens. As can be seen the spatial profiles are very distinct and have different shapes. The transverse spatial profile consists of two main peaks, centred off axis, whilst the longitudinal profile consists of one main peak centred on axis. This is as expected for a propagated mode of this type. Two side lobe peaks are present in the longitudinal profile which are due to the spatial gradients that exist on the edge of the transverse profile. It is also possible to see from this figure the longitudinal component has a smaller width than that of the transverse component. This feature can be very important for certain applications, such as high resolution spectroscopy and non-linear optics. Figure 4.20 shows the longitudinal spatial profile of the longitudinally-polarised and transversely-polarised components. As can be seen the longitudinal field profile lags behind the transverse field by half a cycle; this is expected and explained in the theory section of this thesis and is also noted by Winnerl et al. [4]. Another difference that can be seen in this figure is the difference in oscillatory shape. The longitudinal field can be seen as having a bipolar single cycle shape, whereas the transverse field can be seen as having a near single cycle shape with two small peaks either side of the main peak. These two smaller peaks are of opposite sign to

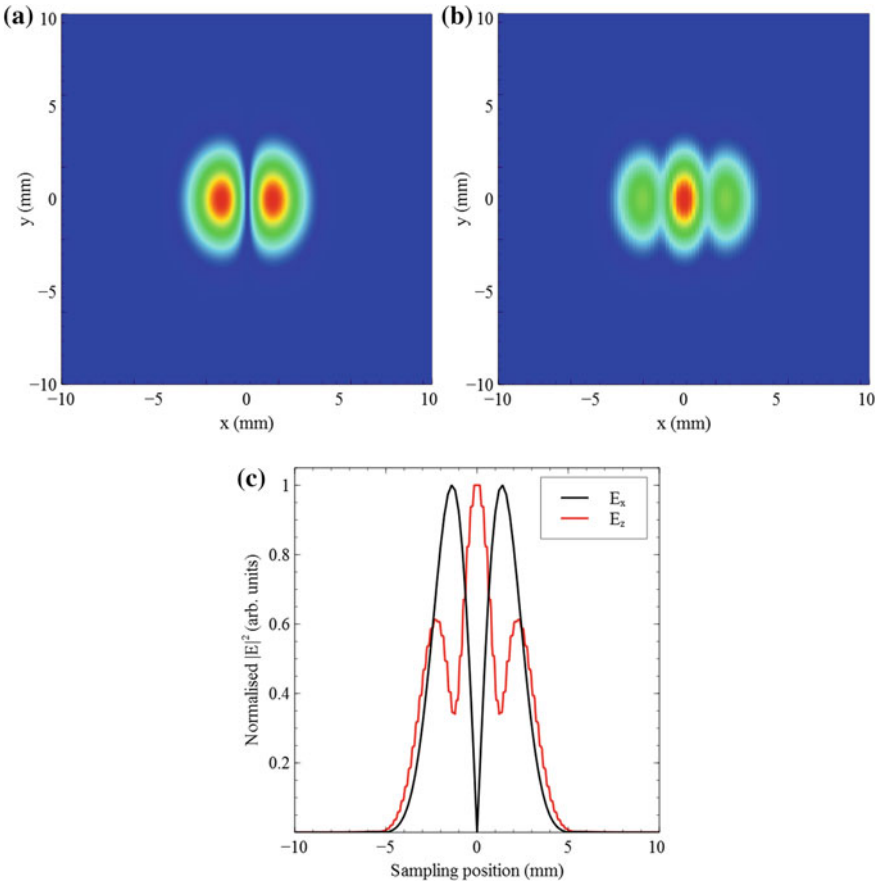

Fig. 4.21 Transverse spatial profiles of the longitudinal and transverse fields taken from their relative local maxima, each normalised to their local maxima: **a** shows the spatial profile of the transversely polarised field component and **b** shows the spatial profile of the longitudinally polarised field component. **c** Shows lineouts of **a**, **b** with the *red line* showing the longitudinal field component and the *black line* showing the transverse field component. For all these plots the sampling position of 0 mm defines the centre of the *x*-axis

the main peak. The oscillations before and after the main pulse in the longitudinal direction are due to the discretisation of the frequency array.

Along with focusing effects and longitudinally polarised component calculations other expected aspects of propagating electro-magnetic radiation can also be seen within the simulation results. These features include temporal profiles and the Gouy phase shift of a focusing beam. The Gouy phase shift describes the 180° phase shift that is experienced by propagating radiation that passes through a focus. To observe this effect within the simulation results a standard Gaussian pulse was propagated through a lens with a focal length of 100 mm. The pulse was then temporally

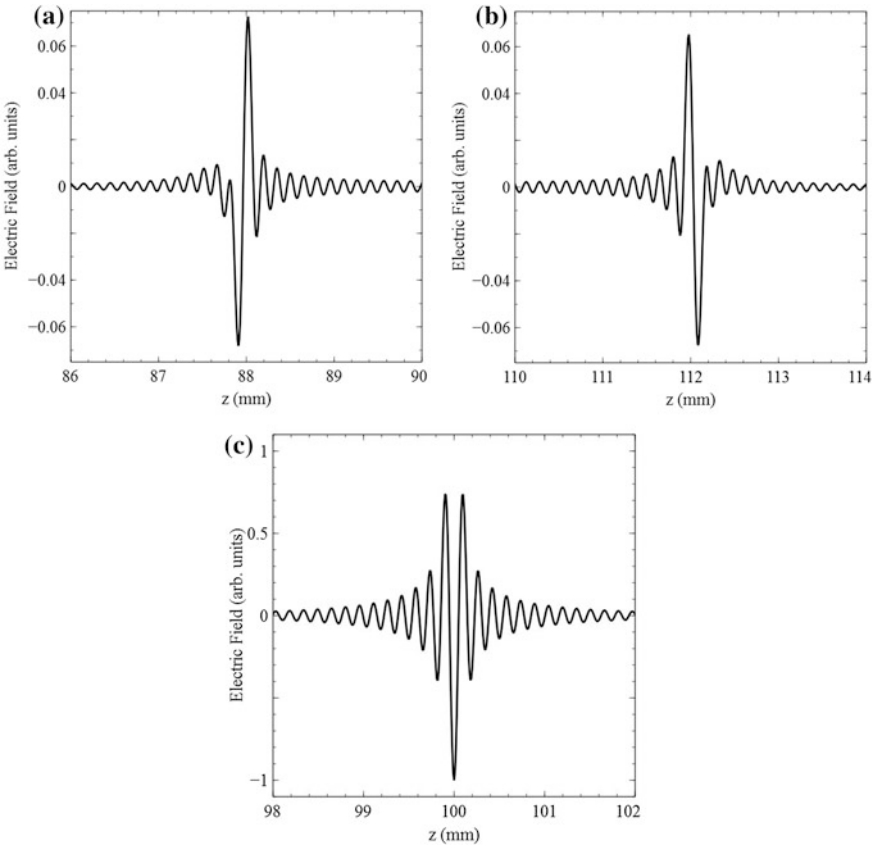

Fig. 4.22 Temporal profiles of a focusing pulse, focal length 100 mm, of electro-magnetic radiation with a Gaussian spatial profile: **a** shows the temporal profile behind the focus, **b** ahead of the focus and **c** at the focus

shifted to 12 mm behind and 12 mm ahead of the focal point and the temporal profiles compared. This can be seen in Fig. 4.22, here (a) shows the temporal profile of the pulse 12 mm behind the focus (b) shows the temporal profile of the pulse 12 mm ahead of the focus and (c) shows the temporal profile of the pulse at the focus. As can be seen by comparing plots (a) and (b) the phase of the two pulses has advanced by 180°, in (a) the main pulse oscillation has a negative spike followed by a positive spike whilst in (b) the main pulse oscillation has a positive spike followed by a negative spike. In (c) it is clear that the temporal profile of the pulse is partway between a bipolar pulse with the phase shown in (a) and a bipolar pulse with the phase shown in (b). This is all as expected and is an interesting output from the simulation.

4.6 Conclusion

In conclusion a radiation propagation simulation has been presented that has been designed, written and tested. The theory behind the simulation, as well as any approximations or assumptions made has been explained in detail. Different elements of the simulation have been detailed and explained including focusing, simulating a broadband beam and how to design a complex input plane. The ability to generate longitudinally polarised electric fields with field strengths comparable to (40% of) the transversely polarised electric fields through the mixing of multiple linearly polarised beams has been demonstrated. Key features of focusing beams such as the Gouy phase shift have been shown to exist within this simulation. Comparisons between the longitudinally polarised electric field in the focal plane of a Laguerre-Gaussian 01 mode and the longitudinally polarised electric field in the focal plane of two linearly polarised Gaussian beams have been made. It was found that, whilst being lower, the longitudinally polarised electric field generated in the focal plane of two linearly polarised Gaussian beams is comparable to that of the longitudinally polarised electric field generated in the focal plane of a similar Laguerre-Gaussian 01 beam.

References

1. S. Casalbuoni, B. Schmidt and P. Schmuser, Far-infrared transition and diffraction radiation, in *TESLA Report* (DESY, 2005)
2. A.A. Tovar, Production and propagation of cylinderically polarized Laguerre-Gaussian laser beams. Opt. Soc. Am. A **15**, 2705 (1998)
3. S.A. Kennedy, M.J. Szabo, H. Teslow, J.Z. Porterfield and E.R.I. Abraham, Creation of Laguerre-Gaussian laser modes using diffractive optics. Phys. Rev. A **66**, 043801 (2002)
4. S. Winnerl, R. Hubrich, M. Mittendorff, H. Schneider and M. Helm, Universal phase relation between longitudinal and transverse fields observed in focused terahertz beams. New J. Phys. **14**, 103049 (2012)

Chapter 5
ALICE Energy Modulation Induced by Terahertz Radiation (AEMITR)

This chapter describes an experiment which was performed at the STFC Daresbury Laboratory using the ALICE accelerator. This experiment attempted to modulate the energy of a 25 MeV electron bunch via the co-propagation of terahertz radiation and a particle bunch. The terahertz frequency radiation used in this experiment was produced by a radially biased PCA that was pumped with a regenerative amplifier laser system. Alignment procedures and terahertz detection schemes are presented along with the results obtained. The detection optics, cameras and software developed are described along with the choices behind why the particular devices used were chosen.

5.1 Introduction

Terahertz radiation exists with electric field oscillations on the sub-picosecond period. Ultra-broadband near single cycle pulse terahertz radiation therefore consist of a propagating electric field oscillation with a period on the 100's of femtosecond timescale. Current accelerators use radio frequency electromagnetic radiation, with temporal periods of the electric field on the μs to ns scale. This, without the use of complex high harmonics, makes it difficult to provide temporal manipulation of the electron bunch below these time scales. As near-infrared laser radiation has electric field temporal periods on the femtosecond timescale its use would enable temporal tuning of an electron bunch on an ultrafine temporal scale. This frequency range however has a problem as it is unable to remain in phase with a particle bunch travelling less than the speed of light for more than a few μm's. Terahertz radiation however, with its electric field period on the 100's femtosecond scale enables the ability to temporal modulate an electron bunch on a much finer scale that that of radio frequency electromagnetic radiation whilst still remaining in phase with the near-speed of light particle bunch for up to 1 m [1]. The temporal properties of ultra-broadband near single cycle terahertz radiation coupled with the ability to

M.J. Cliffe, *Longitudinally Polarised Terahertz Radiation for Relativistic Particle Acceleration*, Springer Theses, DOI 10.1007/978-3-319-48643-7_5

generate 10's MV cm^{-1} field strengths using commercially available laser-driven generation solutions makes it an ideal candidate for applications that require ultrashort electron bunches or electron bunches with complex temporal profiles [2]. Another key reason for wanting to implement a terahertz driven electron beam energy modulation system is synchronisation. As the terahertz is derived directly from a laser pulse using such a technique enables the synchronisation of the electron bunch to the drive laser to femtosecond levels. This is very important when performing experiments that require the electron beam, or radiation generated by the electron beam, to be synchronised to an external laser [1].

The aims of this experiment were therefore to generate a radially polarised terahertz source with strong a longitudinal field component and inject this radiation into the electron beam line such that it co-propagates with the electron bunch. After this interaction any energy modulation imposed onto the electron bunch must be detectable. To detect any energy modulation a screen is placed inside a dispersive chicane to form an energy spectrometer. This screen was then imaged onto a single photon intensified charge-coupled device (CCD) camera. The energy spread of the electron bunch was then monitored and compared with bunches that have not co-propagated with the terahertz radiation present.

5.2 Experimental Setup

This experiment involved a large collaboration and therefore the experimental setup was broken down into a number of work packages. The first was terahertz generation which dealt with how the terahertz radiation was generated, all of the equipment and any radiation transport systems involved. The second was the terahertz injection and interaction region, involving the in situ terahertz diagnostic systems. The third and final was the electron beam diagnostics and included the setup involved in detecting any energy modulation imposed upon the electron beam.

5.2.1 Terahertz Generation

This experiment requires the terahertz radiation to have a number of specific properties. Firstly it is required to have a strong longitudinal electric field component, so the most ideal mode to therefore use would be a radially polarised mode. Second the terahertz radiation should have a high electric field strength and be near single cycle. The terahertz radiation generation system used in this experiment was therefore a large area photoconductive antenna (PCA). The large area PCA consisted of a semi-insulating gallium arsenide (SI-GaAs) wafer. This wafer was circular and had a diameter of 75 mm and was held under a high electric bias field by the use of two electrodes, one annular and one central hemispherical. When the wafer was photo-excited by an ultrafast laser pulse with photon energy greater than

the bandgap of the SI-GaAs material charge carriers are photo-excited into the conduction band. Whilst in the conduction band the charge carriers accelerate along the electric bias field lines, thus generating radiation which is polarised in the direction of charge carrier acceleration. This therefore generates a radially polarised terahertz electric field, which propagates from the wafer into the far field. As well as being able to obtain the correct polarisation state a PCA was also chosen due to the high electric field strengths and near single cycle electric field shape that have been reported in the literature by a number of authors, most notably You et al. [3].

The PCA was photo-excited by a regenerative amplifier laser system, which produced radiation pulses with a central wavelength of 800 nm and a FWHM temporal duration of 50 fs. The output pulse energy of this laser system was up to 1.8 mJ at a repetition rate of 1 kHz. This laser system was situated outside of the accelerator hall and the PCA generation system was situated inside the accelerator hall with more than 20 m of path length between the two. An imaging transport system was therefore designed that enabled the transportation of the laser beam into the acceleration hall and to the PCA generation system. This transportation system required the focusing of the pump laser beam, which would cause temporal distortions due to plasma generation within air. The beam transportation was therefore carried out inside a vacuum pumped beam line. Apertures and targets were used before and after the vacuum beam line to aid alignment. Occasionally optics within the vacuum section moved during the evacuation of the beamline, and in these cases the pump laser beam could be realigned using the mirrors outside of the vacuum section using the apertures and targets to make sure the pump laser beam returned to its original propagation path.

To enable optimal generation the entire area of the PCA should be filled, this is for two reasons. First to ensure that the pump laser fluence is far away from saturation i.e. the number of photons is much more than the number of photo-excited charge carriers and secondly to increases the effective numerical aperture and therefore make the focusing tighter and increase the proportion of the electric field vector that points in the longitudinal direction within the focal plane. In order to completely fill the PCA the pump laser beam is expanded via a plano-concave lens of focal length −75 mm. This expanded beam was then refocused through the antenna a large 3-inch diameter lens with focal length 900 mm. Due to the incident beam on the focusing lens being divergent this makes the effective focal length longer such that the radiation came to a focus at a plane 1.4 m away from the lens.

Focusing radiation has a curved wavefront effective creating a radially varying time delay across the transverse face of the pulse. This therefore creates a radially varying photoexcitation region on the antenna though which the terahertz radiation is generated in temporally varying concentric rings [1, 4]. When propagated into the far field this enables the focusing properties of the pump laser to be imparted onto the forward propagating terahertz radiation. This enabled the terahertz radiation to focus whilst removing the need for any lens, due to the broadband nature of the terahertz radiation such focusing devices inherently cause spectral dispersion and therefore temporal distortions and are therefore not desirable. In order to provide

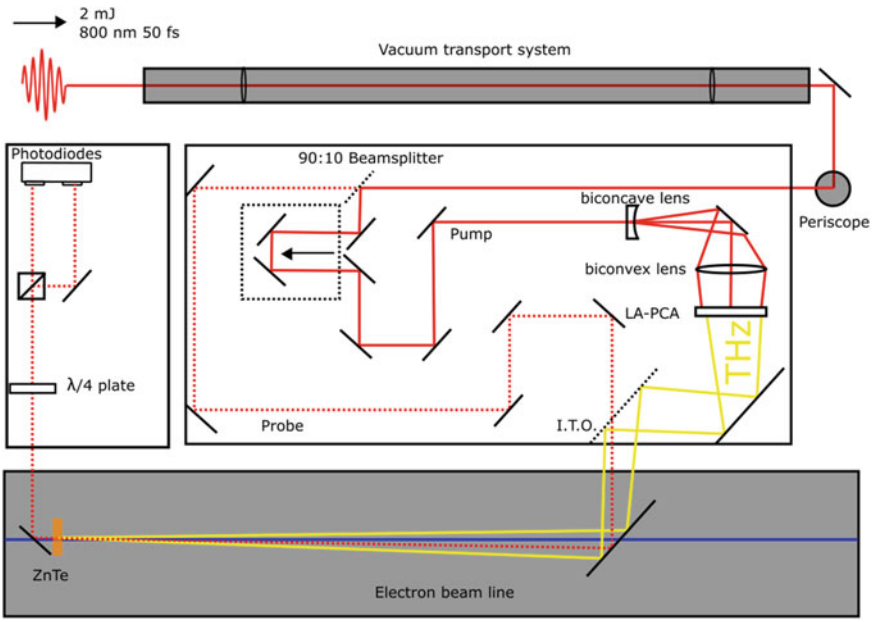

Fig. 5.1 AEMITR experimental schematic showing the laser transport system, terahertz generation system, interaction region and detection region

in situ detection of the terahertz radiation a ZnTe crystal and mirror were attached to a vacuum stage and placed inside the vacuum chamber within the interaction region. This allowed for electro-optic detection to be performed within the beam line. The whole optical setup can be seen in Fig. 5.1, more detailed information regarding different sections such as the terahertz injection and detection will be discussed in more detail in Sects. 5.2.2 and 5.2.3.

5.2.2 *Injection and Interaction*

Once the terahertz radiation was generated it propagated in free space towards, and perpendicular to, the electron beam line. The terahertz radiation entered the electron beam line through a vacuum port window which consisted of z-cut quartz. This material exhibits no birefringence and very little dispersion in the terahertz regime thus helping maintain the near single cycle temporal profile. Once inside the electron beam line the terahertz radiation was incident upon a mirror which had a circular hold cut in the centre. The mirror was 75 mm in diameter and had a 5 mm diameter hole cut in the centre [5]. This mirror directed the terahertz radiation in the direction of the propagating electron beam whilst still enabling the electron beam to pass through its centre. The mirror enabled the terahertz radiation to be brought co-linear with the electron beam.

In order to ensure the terahertz radiation and the electron beam were aligned correctly a screen was placed approximately 1 m downstream from the terahertz injection mirror. This screen was angled at 45° to the electron beam the terahertz radiation propagation direction and was imaged onto a two-dimensional CCD camera. When struck by the electron beam optical radiation was emitted by the screen thus providing two points of reference for the electron beam propagation, the first being the hold in the terahertz injection mirror and the second being the point on the detection screen.

In order to align the terahertz radiation to these two positions the SI-GaAs wafer was removed. Due to the nature of the generation method as long as the pump laser beam strikes the SI-GaAs wafer at 90° to the surface and contains no pulse front tilt it can be assumed that both the forward travelling terahertz radiation will take the same optical path as the pump radiation. The pump beam was aligned such that it was centred on the terahertz injection mirror, it must be noted that the optical spot size on this mirror was larger than that of the hole, and struck the same point as the electron beam on the downstream detection screen. Using this method it was possible to ensure that the electron beam and the optical pump beam, and hence the terahertz radiation, were co-propagating down the beam line.

The wafer and optical generation system was designed such that the focal plane was positioned approximately 40 cm downstream from the injection mirror. This enabled the co-propagation of both the terahertz radiation and the electron beam throughout the Rayleigh range of the focusing terahertz radiation. This was in order to maximise the interaction time and therefore the amount of energy modulation imposed.

5.2.3 Terahertz Detection

In order to help align and ensure that terahertz radiation is actually being generated and propagating down the beam pipe electro-optic detection of the terahertz radiation inside the electron beam line was performed. This detection was done using a 110 cut zinc telluride (ZnTe) electro-optic crystal which was 10 mm × 10 mm 0.5 mm in size. The crystal was positioned on a hydraulic arm that enabled it to be moved in and out of the radiation and electron beam path. The detection crystal was placed at the focus of the terahertz radiation in an attempt to help maximise the electric field strength and hence signal. The first method of detection used was a semi-co-propagating balanced detection method. Figure 5.2 shows a schematic view of this setup in which terahertz radiation is reflected of an indium-tin-oxide coated glass (ITO) plate which allows the probe beam to be transmitted. The probe beam then co-propagated with the terahertz through the beam pipe at a small angle. Perfect co-propagation was not possible due to the injection mirror having a central hole. The removable ZnTe-mirror combination was positioned inside the beam pipe and a balanced detection experiment was performed.

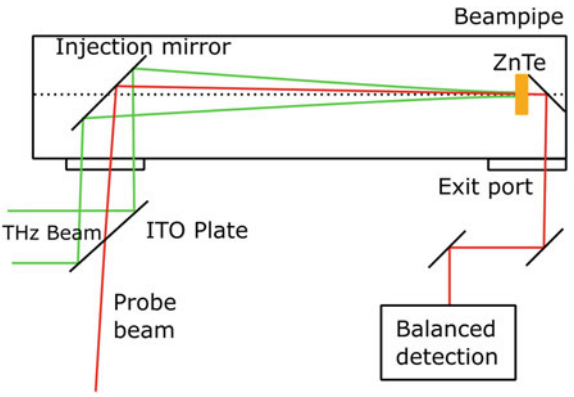

Fig. 5.2 Schematic diagram of the in situ electro-optic terahertz detection scheme used in the AEMITR beam line

Complications in aligning this setup led to a second optical system being designed and built. Again balanced electro-optic detection was used but this time in a reverse propagating reflection geometry. This can be seen in Fig. 5.3, in this system the probe beam enters the beam line through the exit port. It enters the ZnTe crystal on the opposite surface to the terahertz radiation. The probe beam now propagates through the crystal and reflects of the terahertz entrance surface. The terahertz radiation and probe beam then propagate through the detection crystal in a co-linear fashion and this reflected portion of the probe beam is then directed through the standard balanced detection optics and used to obtain a temporal profile of the terahertz electric field. Due to the way this optical setup works multiple reflections of the probe beam are present after the ZnTe crystal. These reflections are due to multiple reflections within the ZnTe crystal and the beam combiner-beam splitter optics. Apertures and beam steering was used to distinguish the correct probe beam reflection from others, which were then blocked.

The ITO plate was controlled via piezo-electric-controlled actuators which enabled the terahertz radiation alignment to be controlled remotely. Example

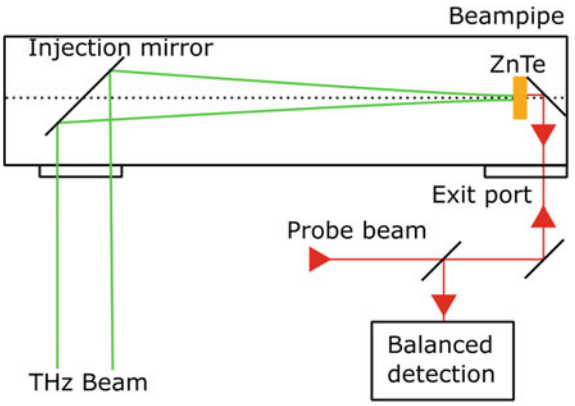

Fig. 5.3 Reverse propagating in situ terahertz balanced detection scheme

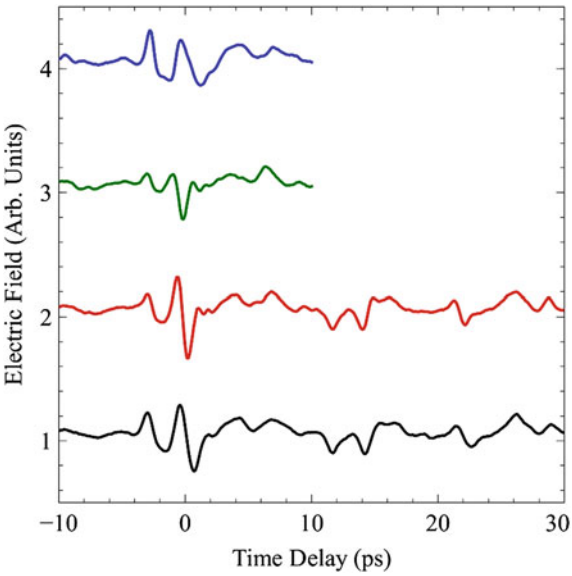

Fig. 5.4 Terahertz in situ electro-optic time scans taken with the horizontal actuator on the ITO plate adjusted with four constant steps

terahertz radiation waveforms taken using the configuration shown in Fig. 5.3 can be seen in Fig. 5.4. This figure shows electro-optic time scans taken with the horizontal actuator on the ITO adjusted with four constant increments. Due to the polarisation state of the terahertz radiation being generated, a polarity flip in the pulse was expected as the horizontal axis was scanned. This was not seen in the data obtained, in fact the temporal profile of the terahertz radiation detected did not take any expected form. This was attributed to the terahertz radiation being misaligned and either clipping the input port, injection mirror or inside of the beam pipe. As well as having an unexplained temporal profile the terahertz radiation detected inside the beam pipe also had electric field strengths that were a lot lower than was previously anticipated.

5.3 Temporal Synchronisation

As the aim of this experiment was to modulate the energy of a relativistic electron bunch with terahertz radiation the electron bunch and terahertz pulse were required to be overlapped in time. There are a number of ways that this was possible and a number of methods were attempted during the experiment. As the terahertz radiation was generated by an 800 nm laser pulse the generation wafer was removed allowing the 800 nm laser radiation to follow the same path as the terahertz radiation. This was done as the laser radiation was much easier to detect using fast photodiodes. To achieve good temporal synchronisation ideally both the electron beam and laser radiation should be detected at the same position on the same device.

To achieve this an optical transition radiation (OTR) screen was placed downstream from the injection mirror. The OTR screen was angled at 45° to the incoming radiation such that it acted like a mirror to the laser radiation directing it out of a viewport window. When the electron beam was incident upon the OTR screen optical radiation was generated and, again due to the angle of the OTR screen, directed out of the same view port. Two detection methods were then used to collect both forms of radiation such that temporal overlap could be achieved. The first detection device used was a streak camera (pco). The streak camera used within this experiment was able to provide a temporal resolution on the order of single picosecond. Due to the low energy of the electron bunch ($\sim$25 MeV) and the low charge (60 pC) insufficient OTR light could be generated such that it could be detected by the streak camera. A second attempt at collecting and imaging both the laser radiation and the optical radiation onto a fast photodiode was also attempted however the outcome was the same, no optical radiation generated by the electron bunch was able to be detected on the photodiode.

5.4 Electron Beam—Terahertz Alignment

Along with achieving temporal synchronisation and overlap between the electron beam and the terahertz radiation spatial overlap must also be achieved. To do this a HeNe laser was injected into the electron beam pipe upstream from the interaction region. Using both the terahertz injection mirror, with its central hole, and a downstream YAG screen as fixed points the HeNe laser was aligned such that it was centred throughout the beam pipe, this setup can be seen in Fig. 5.5. As the pump laser follows the same path as the terahertz radiation it was then aligned such that it co-propagated with the HeNe laser throughout the beam line. This was done by making sure it was centred upon the injection mirror and that it overlapped the HeNe laser on the downstream YAG screen. This YAG screen was mounted along with the same OTR foil that was used for temporal synchronisation. These screens were mounted with a vertical offset and orientated at 90° to each other on an arm which was fixed to the electron beam pipe. This arm can be seen in Fig. 5.6 where

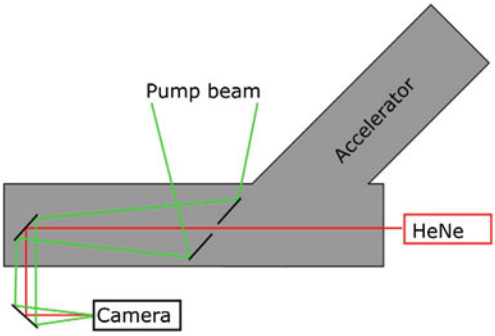

Fig. 5.5 Electron beam to terahertz radiation spatial alignment setup

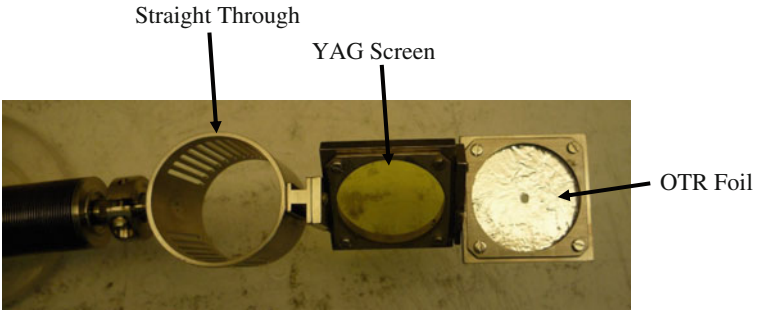

Fig. 5.6 Screen holder with the OTR foil, YAG screen and straight through piece labelled

the two screens are labelled along with the straight through piece which enables the electron beam to pass through the beam line section unhindered and the arm which enables the different components to be inserted into the beamline.

5.5 Electron Beam Detection

The concept of AEMITR was to modulate the energy of a relativistic electron bunch. It was therefore required to measure the energy distribution of the electron bunch so that any imposed modulation could be detected. The interaction region was positioned within ALICE such that there was a magnetic chicane downstream. Screens made of YAG crystal were placed within the centre of the chicane and imaged using a camera. These crystal screens emitted optical radiation when the electron bunch was incident upon them allowing for visual imaging of the electron bunch at the centre of the chicane. Typically a standard CCD camera was used to image the screen, an image of the screen taken by one of these cameras can be seen in Fig. 5.7.

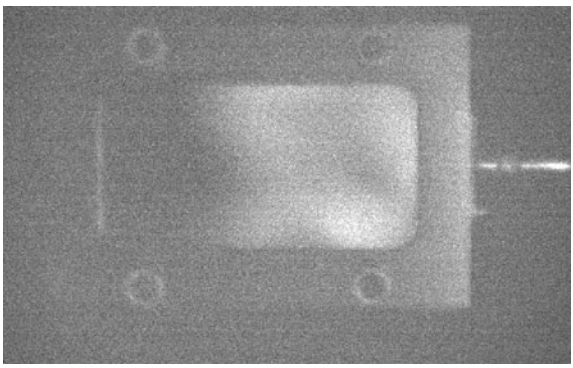

Fig. 5.7 Image of the YAG screen within the chicane taken by a standard CCD camera

Due to the magnetic makeup of the chicane within the centre, where the screen was located, the horizontal axis represented energy of the beam. This setup of the camera, screen and chicane acted as an energy spectrometer for the electron bunches. The temporal structure of the electron bunch train on ALICE enabled for a background subtracted image to be obtained. This meant that an image with no terahertz radiation present could be taken along with an image when terahertz radiation was propagating along with a bunch. By subtracting the two images any difference within their energy spreads became more apparent.

For this background subtraction to be most effective the two bunches should have identical temporal and energy profiles. As this is not possible due to temporal jitter from a multitude of sources, cathode laser arrival time jitter, cavity radio frequency jitter and temporal fluctuations to name a few, it was decided that the two bunches to be compared should be as close to each other in time as possible. It was noticed that the energy jitter measured was greatly reduced if the two bunches were taken from the same macro pulse. In order to obtain images of electron bunches separated by a short temporal duration a different camera to the standard CCD camera was used. An intensified camera (pco DICAM Pro) was installed below the beamline and optics used to image the screen. This camera had a double trigger function which enabled the capture of two images separated by only a few 100 ns. Whilst within the same macro pulse the minimum bunch to bunch separation was on the order of 9 ns. Limitations in the YAG screen and intensified camera used for detection meant that this separation was increased to a value on the order of 500 ns. When this separation was lowered it became apparent that the second bunch always appeared to be less intense than the first. This can be explained by the scintillation time of the intensified camera used.

To enable accurate measurements of the energy spread the screen must be imaged correctly onto the sensing element of the camera. An optical setup consisting of the intensified camera, beam splitters, mirrors, lenses and a HeNe laser were used. This setup can be seen in Fig. 5.8 where it can be seen that a HeNe laser is used to help obtain an initial alignment of the YAG screen image onto the camera. The HeNe beam is reflected of a beam splitter and passes through an iris. The beam was then raised up to the electron beam height by a periscope which directed the HeNe towards to beamline window. The back reflection from the

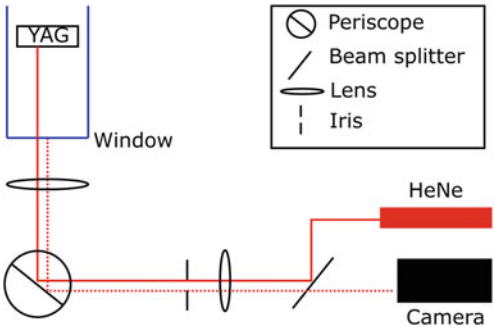

Fig. 5.8 Schematic of the intensified camera alignment system. *Solid red line* shows the HeNe beam path whilst the broken *red line* shows the back reflection from the electron beamline window

entrance window then re-entered the periscope where it passed through the iris, passes through the beam splitter and was incident upon the camera. By aligning the optics such that the HeNe was correctly positioned on the YAG screen, window and the back reflection was centred upon the cameras entrance optics it is possible to confirm proper alignment of the camera.

To further ensure correct alignment the camera was positioned such that the iris was centred within the sensor. Whilst this procedure enabled the correct placement of the camera and optics, the focusing and imaging of the screen onto the camera sensor was also important. The camera and imaging system were situated out of the plane of the electron bunch and screen to help protect any sensitive electronics from X-ray radiation. This therefore meant a periscope was required to image the HeNe and meant the alignment procedure was even more crucial as there was not enough light reflecting from the screen and travelling down the periscope to align the system by eye.

This was achieved by using a macro lens placed onto the front of the camera along with two biconvex lenses. The two biconvex lenses produced an image of the screen at approximately 15 cm in front of the camera. The macro lens then imaged and magnified this image plane onto the cameras sensor. The YAG screen had no decals or marking on its surface that could be used to fine tune the imaging optics. It was therefore held by a locking nut in a position such that the screens holder was visible by the camera. The holder had a number of marks and features that could be used to help find tune the focusing. Once these marks were within the field of view of the camera the macro lens was adjusted such that they were brought into focus. This can be seen in Fig. 5.9, here the markings (338) are shown in (c) and (d) whilst the screw holes are shown in (a) and (b). The initial images before the focusing had been optimised can be seen in Figures (a) and (c) with the final images after focusing had been optimised shown in (b) and (d). The combination of using the HeNe laser, iris and markings made for a reproducible imaging system that enabled confidence in the imaging system.

As it was only possible to achieve temporal synchronisation of 100's ps between the electron bunch and terahertz radiation the terahertz radiation was scanned in time with respect to the electron bunch and camera images were taken at various temporal positions. This was achieved by passing the terahertz pump laser beam through a delay stage, the delay stage varied the path length of the laser and hence delayed the generation of terahertz radiation. Camera images taken were summed across the axis orthogonal to the energy axis to give an energy spectrum plot per shot. A Gaussian fit was then applied to the energy spread from which the Gaussian width was extracted. The Gaussian width of the interaction bunch was then subtracted from the Gaussian width of the background bunch. The difference value was then recorded and plotted as a function of time. Any energy modulation imposed onto the electron bunch by the terahertz radiation should be visible as a spike in these plots caused by the difference in the Gaussian widths changing. This spike should be constant with position and indicate a change in energy spread.

To perform this action a MATLAB program was created which was able to automate the collection and analysis of the data. This program recorded the two

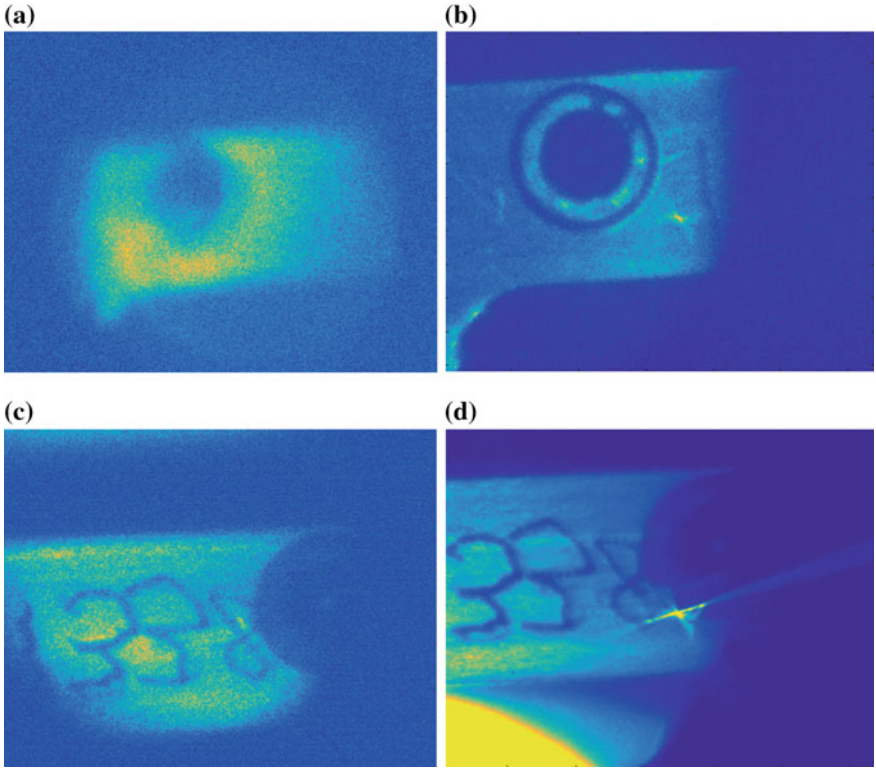

Fig. 5.9 Camera images taken of **a**, **b** the screw hole and **c**, **d** the markings on the screen mount. Images **a**, **c** are before focusing optimisation had occurred

images, performed the integration down the image axis, fitted a Gaussian to the data and plotted the Gaussian width against stage position. The program then moved the stage and repeated the process. A screen shot of the program graphical user interface (GUI) is shown in Fig. 5.10 where the top two images show both the modulated and unmodulated electron bunches, the summed down energy spectra along with fitted Gaussians and the Gaussian widths as a function of time and stage position. This automation enabled for time scans to be performed ensuring that temporal overlap between the electron bunch and terahertz radiation was achieved at some point. This software also enabled direct control of the camera and stage settings such as gain, trigger style, exposure time, delay, step size and time scan range.

As the temporal overlap of the electron bunch and terahertz radiation was limited to an accuracy of ± 3 ns a range of 6 ns was scanned. This was achieved by using a combination of optical stages and commercially available laser synchronisation software (Coherent SYNCHROLOCK). The optical stage delayed the pump beam arrival time with respect to the electron beam and provided a range of 0.5 ns. The

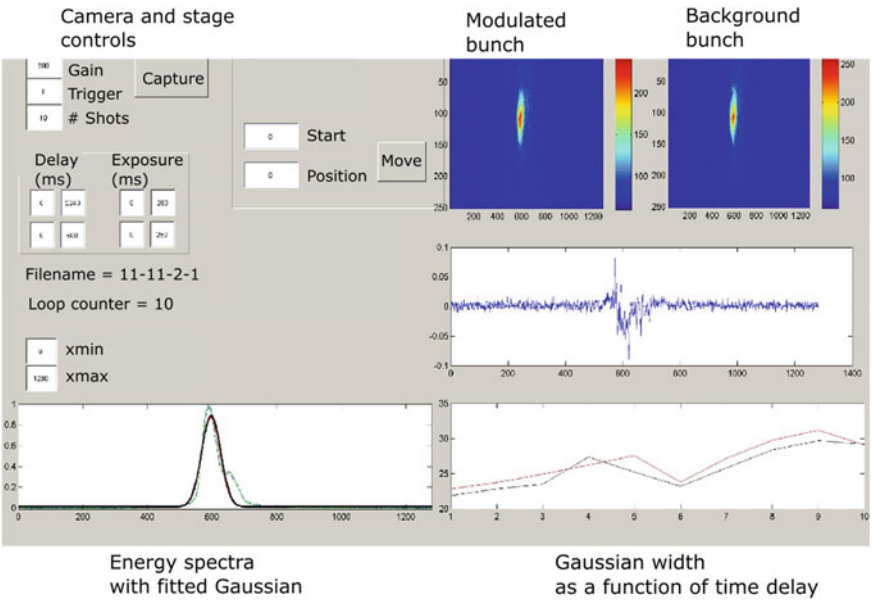

Fig. 5.10 GUI screenshot showing the camera controls, stage controls, electron bunch images and analysis

laser synchronisation software was able to adjust the relative phase of the drive oscillator laser with respect to the photo-injector oscillator and had a range of 9 ns. Using an iterative combination of scanning the optical delay stage, then stepping the laser synchronisation software and repeating it was possible to scan the full 6 ns range. Whilst the stage was scanning the electron beam energy profile was monitored and recorded as a function of stage position and laser synchronisation software offset.

5.6 Discussion and Conclusion

The AEMITR experiment aimed to modulate the energy profile of relativistic electron bunches on the ALICE accelerator with laser generated terahertz radiation in a co-linear geometry. The terahertz radiation was generated via a large area photoconductive antenna which was pumped using a femtosecond regenerative amplifier laser system. A radially symmetrical polarisation state was generated through the design of bias field applied to the antenna with the aim of generating large longitudinally polarised electric fields. The energy profile of two electron bunches separated by up to 500 ns were monitored with the aim of detecting a modulation of one of the electron bunches due to its co-linear propagation with terahertz radiation.

Spatial and temporal synchronisation of the terahertz radiation and electron bunch was attempted along with in situ electro-optic terahertz detection. Whilst temporal synchronisation was not achieved to a desirable level, less than 1 ps, it was achieved to within the range of the scanning apparatus available, 6 ns. No energy modulation of the electron bunches was detected whilst performing this experiment. This is attributed to a number of factors with the main being the low longitudinally polarised electric field strength of the terahertz radiation used. This coupled with the unexplained temporal profiles of the detected terahertz radiation and the lack of temporal synchronisation make the absence of a detected terahertz-induced electron bunch acceleration signal unsurprising.

Whilst no terahertz induced energy modulation was detected during this experiment a lot of useful and practical knowledge was gained. The importance of full source characterisation along with the need for good temporal synchronisation was realised. New practical techniques for the spatial alignment of electron beams and optical radiation were learnt and improved upon. All of which will be utilised in future experiments of this nature.

References

1. S.P. Jamison, M.J. Cliffe, D.M. Graham, T. Thakker, B. Muratori, Y.M. Saveliev, R.J. Smith, W.R. Flavell, D.J. Holder, D. Newton and A. Wolski (2012) Phase space manipulation with laser-generated terahertz pulses, in *34th International Free Electron Laser Conference*, Japan
2. J.A. Fülöp, L. Pálfalvi, S. Klingebiel, G. Almási, F. Krausz, S. Karsch and J. Hebling, Generation of sub-mJ terahertz pulses by optical rectification. Opt. Lett. **37**, 557 (2012)
3. D. You, R.R. Jones, P.H. Bucksbaum, D. R. Dykaar, Generation of high-power sub-single-cycle 500-fs electromagnetic pulses. Opt. Lett. **18**, 290 (1993)
4. M.J. Cliffe, A. Rodak, D.M. Graham and S.P. Jamison, Generation of longitudinally polarized terahertz radiation with field amplitudes exceeding 2 kV/cm. Appl. Phys. Lett. **105**, 1191112 (2014)
5. D. Holder, *Communication with*, 2015

Chapter 6
Photoconductive Antenna Generation

This chapter describes the characterisation of the radiation generated by a large-area PCA used within the experiment described in Chap. 6. Electro-optic detection was employed to detect the terahertz radiation and provided information regarding the temporal profile, polarisation state and spatial profile of the terahertz radiation. Electric field amplitudes were calculated for both the directly detected longitudinally polarised field and the transversely polarised field components. Work described within this section was published in Applied Physics Letters on the 12th November 2014 [1].

6.1 Introduction

In order to accelerate charged particle bunches with radiation in a co-linear propagation scheme, similar to the scheme described in Chap. 5, the electric field of the radiation must be orientated in the direction of the electron beam and hence radiation propagation [2]. This is commonly referred to as the longitudinally polarised electric field component, E_z. As described previously and shown in Eq. (6.1) longitudinal fields are present when there is a spatial transverse field gradient.

$$\nabla E_z(x, y, z) = -\int \nabla_{\perp} E_{\perp}(x, y, z) dz, \tag{6.1}$$

where $E_{\perp}(x, y, z)$ is the transversely polarised electric field. Radially polarised beams, which can be described as Laguerre-Gaussian 01 modes, contain very strong spatial transverse field gradients in the centre of the beam [3]. They should also therefore contain strong longitudinally polarised field components in the centre. A large area photoconductive antenna (PCA) made of SI-GaAs was designed and built such that it produced radiation of this polarisation state. Both the longitudinally and transversely polarised field components produced by this antenna were

M.J. Cliffe, *Longitudinally Polarised Terahertz Radiation for Relativistic Particle Acceleration*, Springer Theses, DOI 10.1007/978-3-319-48643-7_6

characterised as a function of longitudinal and transverse space and time via electro-optic detection techniques.

Photoconductive antennas consist of a semiconducting material which is held under a high electrical bias field. When photoexcited by an ultrafast laser pulse with photon energy larger than the band gap energy, electrons in the valence band are liberated into the conduction band. Once in the conduction band they are free to move and accelerated under the electric bias field. This acceleration of charge emits radiation polarised in the direction of acceleration of the charge. As electric bias fields with complex spatial profiles can easily be applied by shaping the electrodes this method offers a straightforward means of generating longitudinally polarised radiation. When photoexcited with an ultrafast laser pulse, such as a 50 fs 800 nm optical pulse, the temporal profile of the generated terahertz radiation is very nearly singe-cycle. Photoconductive antennas are also capable of producing fields with high peak electric field values [4]. All of these properties, the easily designable polarisation state, the near single cycle temporal profile and the high electric field strengths make antennas an ideal candidate for generating terahertz radiation suitable for relativistic electron beam manipulation [2].

6.2 Photoconductive Antenna

The photoconductive antenna used within this experiment consisted of a semi-insulating gallium arsenide (SI-GaAs) wafer with a thickness of 500 μm and a diameter of 76.2 mm. The electrode geometry was designed such that a radially polarised terahertz pulse would be generated and therefore contain strong longitudinally polarised components in the centre of the beam. This electrode geometry imposed a radially symmetric electric bias field upon the antenna which was achieved by attaching radially symmetric electrodes to the surface of the antenna. The electrodes consisted of a centre hemispherical electrode of radius 10 mm and an outer annular electrode of inner radius 36 mm. The outer electrode consisted of an aluminium ring which encased the outer edge of the wafer, whilst the central electrode consisted of an aluminium foil disc, both of which were attached with silver conductive paint. A direct current (DC) lab power supply provided a voltage to a car ignition coil which converted the DC voltage into a high voltage pulse with a temporal duration of 6 μs. This voltage pulse was applied directly to the antenna outer electrode via a copper wire attached to the end of the ignition coil and the electrode. The ignition coil was wired in parallel to a high resistance potential divider which divided the voltage by a factor of 4000 therefore enabling the signal to be monitored on an oscilloscope. An oscilloscope trace showing the voltage pulse applied to the wafer is shown in Fig. 6.1. The sharp cut off in the applied bias and the negative peak are due to the excitation laser pulse being incident upon the wafer and allowing current to flow. The position of this sharp cut off and hence the excitation laser pulse arrival time was adjusting using phase delay electronics to

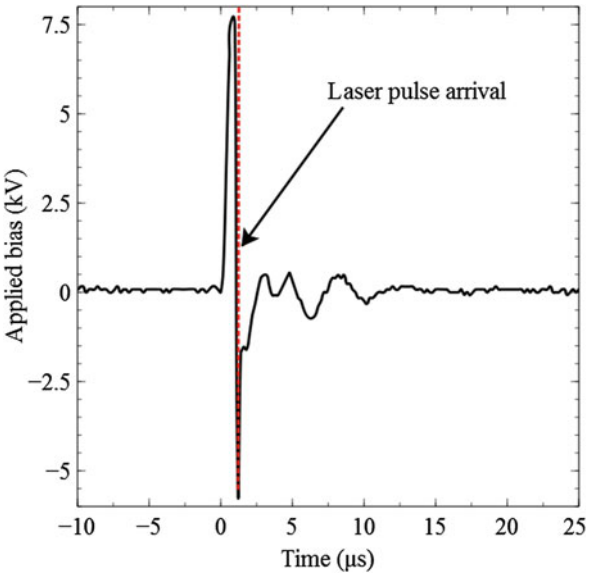

Fig. 6.1 Oscilloscope trace showing the voltage pulse applied to the PCA

give the maximum terahertz electric field strength. Peak voltages of 100 kV were achievable until breakdown prevented higher voltages from being applied.

The antenna was housed within polytetrafluoroethylene (PTFE) enclosure which was coated with aluminium foil and grounded to the optical table for safety reasons. Two holes were cut in the enclosure, one to allow the optical excitation radiation to enter and one to allow the terahertz radiation to exit. Inside the enclosure the wafer was orientated such that the surface to which the central electrode was attached was facing the incoming excitation radiation. As the excitation radiation cannot pass through the wafer, as the antenna is able to absorb the 800 nm photons, but the terahertz radiation can this enables the most efficient generation of terahertz radiation.

6.3 Optical Setup

An optical setup was designed and built that was able to generate and detect both the transverse and longitudinally polarised terahertz electric field components. This optical setup employed the optical radiation provided by a regenerative amplifier laser system (Spitfire Pro. Spectra-Physics). The laser produced pulses with 1 mJ of optical energy, with a central wavelength of 800 nm and a temporal duration of 100 fs. These pulses entered the setup at a repetition rate of 500 Hz and were split into two optical paths, the pump beam path and the probe beam path, by a 90:10 reflection:transmission beam splitter. The pump beam was used to generate the terahertz radiation and contained 90% of the optical energy whilst the probe beam

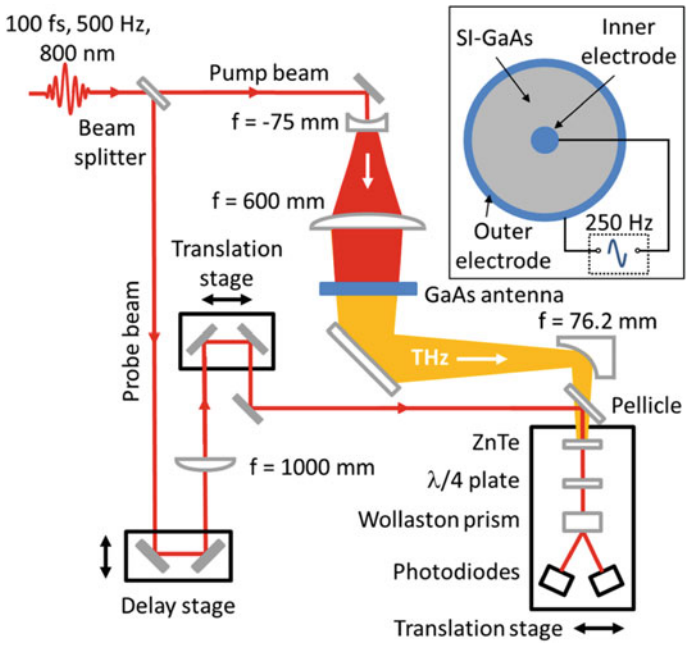

Fig. 6.2 Layout of the optical setup used to generate and detect both longitudinally and transversely polarised terahertz electric field components

was used to detect the generated terahertz radiation and contained 10% of the optical energy. The optical setup used within this experiment can be seen in Fig. 6.2 and a photograph of the optical table is shown in Fig. 6.3.

The pump beam was expanded by a 1 inch diameter plano-concave lens with a focal length of −75 mm. The radiation was then collected by a 3 inch diameter plano-convex lens with a focal length of 600 mm; this lens focused the diverging optical radiation which was then incident upon the photoconductive antenna. The photoconductive antenna was placed before the focal plane of the optical radiation. This meant that the optical wave fronts had a radially varying time delay. This in turn gave rise to a radially varying excitation region, effectively generating a phased array antenna, which caused the generated terahertz radiation to obtain the focusing properties of the optical excitation radiation. The generated terahertz radiation was then collected by a 2 inch diameter 90° off-axis gold-coated parabolic mirror with an effective focal length of 76.2 mm. Due to the curvature of the terahertz wave fronts before they were incident upon the parabolic mirror this effective focal length was reduced to 75 mm. A ZnTe electro-optic detection crystal was placed within the focal plane of the terahertz radiation. Depending on the required detection polarisation this crystal was either a (100), or a (110), cut ZnTe crystal, both of size 2 mm × 10 mm × 10 mm.

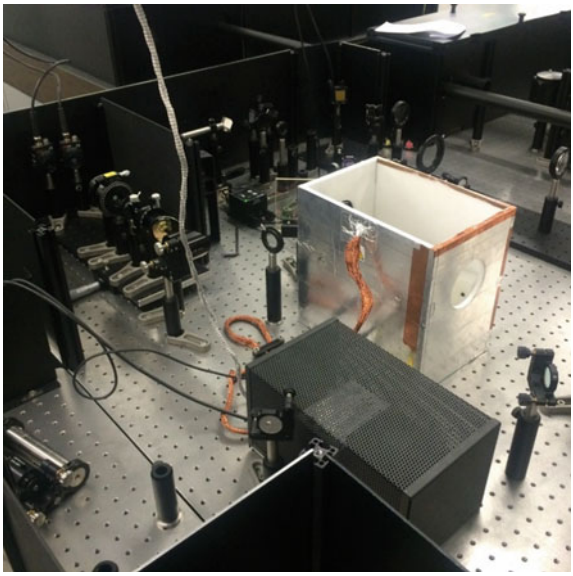

Fig. 6.3 Photograph of the optical setup used to generate and detect transversely and longitudinally polarised terahertz radiation

The probe beam was routed through optics such that it overlapped the terahertz radiation both spatially and temporally on the detection crystal. A plano-convex 1 inch diameter lens was used to focus the probe beam to a small spot in the focal plane of the terahertz radiation. The focal length of this lens was chosen to be 1 m so that it was not necessary to re-collimate the beam after the ZnTe crystal as it remained within the aperture size of all the detection optics. The probe beam and terahertz radiation were combined by a 2 inch diameter 60:40, reflective:transmitted, pellicle beam splitter. This allowed the terahertz radiation to pass through whilst reflecting 60% of the probe beam towards the ZnTe crystal. Two translation stages were placed in the probe beam path. The first moved in the direction of the probe beam propagation, as in a standard terahertz time-domain spectrometer, and enabled the arrival time of the probe beam at the detection crystal to be adjusted with respect to the terahertz radiation. The second stage moved orthogonally to the direction of propagation and enabled to the position of the probe beam to be scanned horizontally on the ZnTe crystal with respect to the terahertz radiation. All of the mirrors were 2 inches in diameter after this point as to ensure that the beam remained confined to the surface of the optics as it was translated. This stage was optically designed such that when moving horizontally no time delay with respect to the terahertz radiation was induced, removing the need for post processing and removing one potential degree of ambiguity from the data. By taking time scans at multiple transverse stage positions it was possible to build up a spatial map in one dimension. This one done using both the (100) (for longitudinal) and (110) (for horizontal) ZnTe detection crystals providing information regarding both the spatial and temporal properties of each of the terahertz polarisation states.

A balanced electro-optical detection scheme was used to measure any phase rotation imposed on the optical probe by the terahertz radiation within the ZnTe crystal. To ensure the correct polarisation component was being measured it was imperative that the terahertz radiation and probe beam were propagating in a co-linear fashion through the ZnTe crystal. To ensure that this was the case a wire crosshair alignment tool was created and placed in the pump beam and the antenna was then removed along with all of the detection optics. Both the pump and probe beam were then aligned such that they were travelling collinearly throughout the detection optics. The antenna and detection optics were then replaced with the detection optics being aligned to the probe beam and the back reflection of the pump beam off the antenna surface being used to ensure it was placed at 90° to the pump beam propagation. To help improve the signal-to-noise ratio a lock-in amplifier was used to monitor the photodiode signal. To enable the lock-in amplifier to measure the signal, the terahertz radiation was generated at half the repetition rate (250 Hz) of the probe laser (500 Hz). The frequency was set by applying a bias pulse to the antenna at half the repetition rate of the laser.

6.4 Confirmation of Radially Polarised Terahertz Radiation

A modified electro-optic detection system which enabled two-dimensional imaging of the terahertz electric field, as described in Sect. 2.4.2.2, was used to confirm the radially polarised nature of the terahertz electric field. A half-wave plate was added to the balanced electro-optic detection scheme between the quarter-wave plate and (110)-cut ZnTe crystal. With the (110)-cut ZnTe crystal removed the quarter-wave plate was set such that it did not alter the polarisation state of the probe beam and the newly added half-wave plate was set such that the probe beam was vertically polarised. This meant that the output of the Wollaston prism contained the full probe beam whilst one output was fully extinguished. The detection crystal was then placed back into the optical path and the quarter-wave plate was used to cancel out any birefringence added by the ZnTe crystal, ensuring the extinguished output of the Wollaston prism remained extinguished.

A CCD camera (pco. Pixelfly) was then used to image the ZnTe crystal whilst looking through the extinguished output of the Wollaston prism. When the terahertz beam was incident upon the ZnTe crystal a phase rotation of the near-IR optical probe beam was induced, in the same way that a phase rotation occurs in the standard balanced detection setup. However with this detection setup this phase rotation caused a proportion of the probe light to now exit the Wollaston prism through the previously extinguished output path, and hence be detected by the CCD camera. As the collimated probe beam was larger in transverse size than the terahertz beam the phase rotation undergone by the probe beam only occurred in spatial

areas where the terahertz beam was present. This enabled the CCD camera to see a spatial map of the terahertz electric field on the surface of the ZnTe crystal.

The direction of the phase rotation was dependent upon the polarity of the terahertz electric field, however due to the CCD camera only being able to detect the intensity this information was lost in this configuration. To obtain this polarity information the quarter-wave plate was slightly offset in azimuthal rotation, such that the camera was able to detect a small amount of optical laser probe. With this configuration when the terahertz electric field was incident upon the crystal the phase rotation either increased or decreased the intensity detected by the camera. If the terahertz radiation caused the intensity detected by the camera to increase then the phase rotation induced and hence the polarity of the terahertz electric field was opposite to that when the camera detected a decrease in optical probe intensity.

Using the technique previously described a full spatial map of the terahertz electric field polarisation state was built up. Due to the nature of electro-optic detection and the geometry of the (110)-cut ZnTe crystal only one linearly polarised component could be detected at a time. A half-wave plate was therefore added to the probe beam path which was used to rotate the probe beam polarisation and therefore sample different linearly polarised components of the terahertz electric field. By rotating the probe beam polarisation through 180° and monitoring the camera signal the radially polarised nature of the terahertz electric field was confirmed, as shown in Fig. 6.4. As can be seen the images in Fig. 6.4 with (a) showing horizontally polarised terahertz radiation and (b) showing vertically polarised terahertz radiation. This bipolar spatial field pattern rotates at twice the angle of the probe beam polarisation as is expected due to the (110)-cut ZnTe crystal geometry. The detected field pattern confirms the radial nature of the generated terahertz electric field polarisation.

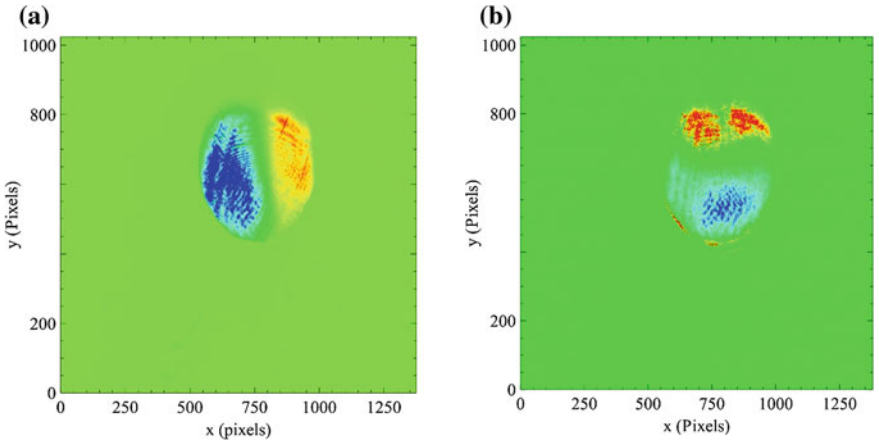

Fig. 6.4 Crossed polarisation images of terahertz radiation with **a** showing the horizontally polarised component and **b** showing the vertically polarised component

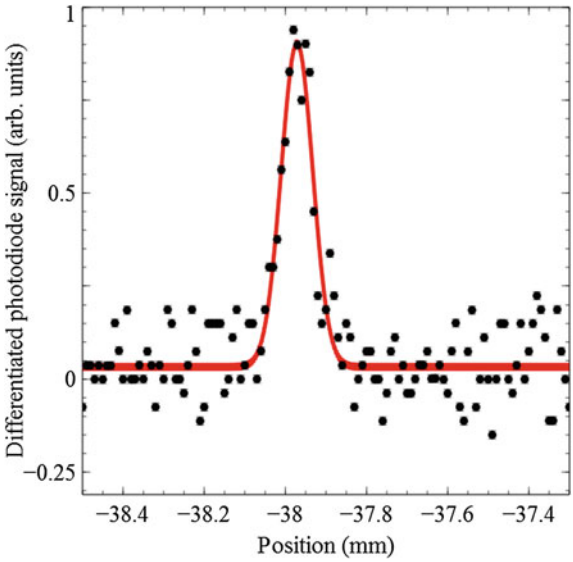

Fig. 6.5 Differentiated photodiode signal as a function of knife-edge position. *Black dots* represent the measured data points whilst the *red line* represents a Gaussian fit to the data (Color for online)

6.5 Profiling the Probe Beam

The imaging of the spatial properties of the terahertz radiation was carried out by moving the probe beam with respect to the terahertz radiation on the ZnTe crystal surface. The spatial resolution was of the imaging was limited by the smallest increment of the translation stage and the probe beam spot size. To enable accurate movement of both the transverse translation stage and the detection translation stage the optical breadboards that housed the optics were placed on micrometre-driven stages. To avoid hysteresis the stages were only moved in one direction during measurements. To obtain a small probe spot size at the ZnTe crystal surface the probe beam was focused by a lens with a focal length of 1 m.

To measure the probe beam spot size in the detection crystal plane a knife-edge scanning system was setup. In this setup a knife edge was placed on a micrometre-driven stage and was scanned horizontally through the probe beam. A photodiode situated behind the knife edge recorded the electric field intensity as a function of knife edge position. A Gaussian transverse profile was assumed, with $E(x,y) = E_0 \mathrm{e}^{\frac{r(x,y)^2}{\omega_0^2}}$, where $E(x,y)$ is the electric field intensity as a function of the transverse co-ordinates (x,y), $r = \sqrt{x^2+y^2}$ is the radius of the beam, ω_0 is the beam waist and E_0 is the scalar intensity of the electric field. The total power, P, within the beam is the intensity integrated over the area and may be expressed as,

$$P = \iint_{-\infty}^{\infty} E_0 \mathrm{e}^{-\frac{r(x,y)^2}{\omega_0^2}} dxdy, \tag{6.2}$$

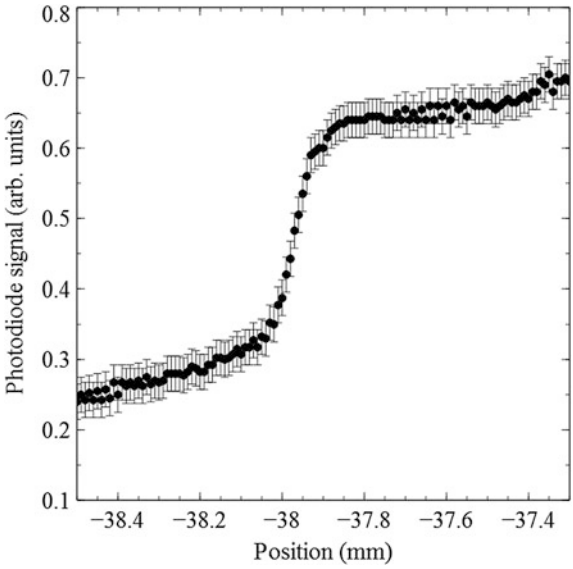

Fig. 6.6 Photodiode signal as a function of knife-edge position

which yields,

$$P = \frac{\pi}{2} E_0 \omega_0^2. \tag{6.3}$$

Therefore by differentiating the signal obtained by from the photodiode as a function of transverse position a complete spatial beam profile can be obtained. Figure 6.6 shows the measured photodiode signal as a function of the knife-edge position, whilst Fig. 6.5 shows the photodiode signal differentiated with respect to the knife-edge position. From this Gaussian fit a $1/e^2$ ω_0 value of 91.6 ± 2 μm was obtained.

6.6 Detection Crystal Angles

The azimuthal angles of both the (110)-cut and (100)-cut ZnTe detection crystals must be set correctly with respect to both the probe laser and terahertz radiation polarisation to enable the maximum detection signal to be obtained. As the (110) ZnTe crystal had previously been used to detect transversely polarised terahertz radiation its azimuthal angle could be set to enable optimal detection of horizontally polarised terahertz radiation with a horizontally polarised probe beam. For this case the azimuthal rotation of the (110)-cut ZnTe detection crystal was adjusted such that the $[1\bar{1}0]$ axis was in the horizontal plane. This was however not

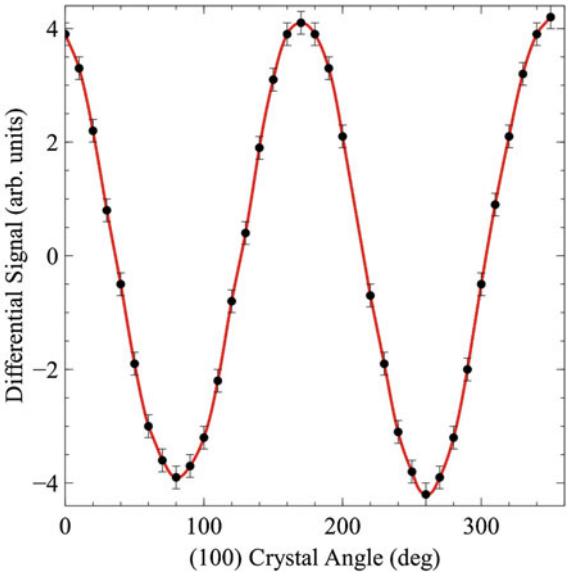

Fig. 6.7 Signal measured on the lock-in amplifier as a function of (100)-cut ZnTe crystal azimuthal angle. Measurements were performed with a horizontally polarised optical probe and longitudinally polarised terahertz radiation

optimal for the detection of longitudinally polarised terahertz radiation with the (100)-cut ZnTe crystal. It was therefore sensible to verify the crystal axis and investigate its azimuthal angular dependence upon the measured signal. To do this, a standard balanced electro-optic detection system was used and the maximum signal for the longitudinally polarized terahertz field was found. The transverse and temporal scanning stages were positioned for maximum signal and the (100) ZnTe crystal rotated around its azimuthal angle. Using the dependence reported by Winnerl et al. [5] as a guide the probe beam polarisation was set horizontally and the (100)-cut ZnTe crystal was orientated such that the [100] axis was at an angle of 30° with respect to the laser polarisation. The differential signal obtained by the lock-in amplifier was recorded at a number of angles; this data can be seen in Fig. 6.7. As can be seen the differential signal has a sinusoidal dependence on the azimuthal crystal angle with a period of 180°. This is different to the more commonly employed (110)-cut ZnTe crystals which whilst also showing a sinusoidal relationship have a period of $\frac{\pi}{3}$. This relationship agrees with the data published by Winnerl et al. [5] which shows the same relation. It should be noted that the maximum differential signal was found with the initial (100) ZnTe detection crystal angle of 30°; again this agrees with previously published data [5]. To ensure birefringence due to the rotating crystal angles was not affecting the results the photodiode signals were monitored on an oscilloscope and rebalanced if and when required using the quarter waveplate.

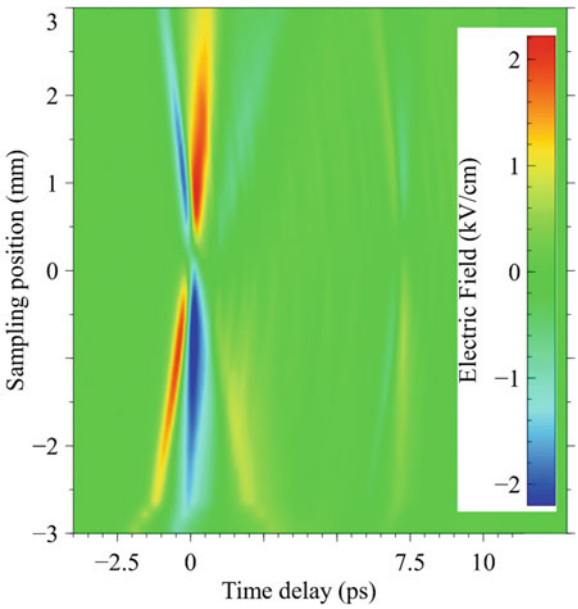

Fig. 6.8 Electro-optic time scans as a function of sampling position. Data taken using the (110)-cut ZnTe crystal with a horizontally polarised probe beam

6.7 Transversely Polarised Terahertz Radiation

Figure 6.8 shows electro-optic time scans that were obtained as a function of transverse position with the ZnTe (110)-cut crystal. This detection crystal was only sensitive to horizontally polarised terahertz radiation. In this figure electro-optic time scans were taken as a function of sampling position, where the sampling dimension is the same as the polarisation of the terahertz being detected i.e. the probe beam was scanned horizontally and detection scheme was sensitive to the horizontally polarised terahertz component. The data shown in Fig. 6.8 were taken with an electrical bias voltage of 40 kV applied to the antenna. The main terahertz pulse is shown at a time delay of 0 ps centred on a sampling position of 0 mm.

An electric field polarity flip can be seen in Fig. 6.9 as the sampling position is scanned through the origin of the beam at every point in time. This feature is expected from a radially polarised beam as the polarisation points outwards from the beam centre at all points.

A terahertz radiation reflection in the SI-GaAs wafer can be seen at approximately 7 ps. This reflection has the opposite polarity to the main pulse and is due to it being a reflection off the photoexcited plasma which forms on the excitation surface of the PCA. Due to the plasma having a higher refractive index than the SI-GaAs material a 180° phase rotation is observed. The measured time delay fits with an internal reflection of terahertz radiation within SI-GaAs as the refractive index of SI-GaAs is approximately 3.5 [6] in the terahertz region and the total distance travelled is 600 μm. More information regarding the terahertz temporal

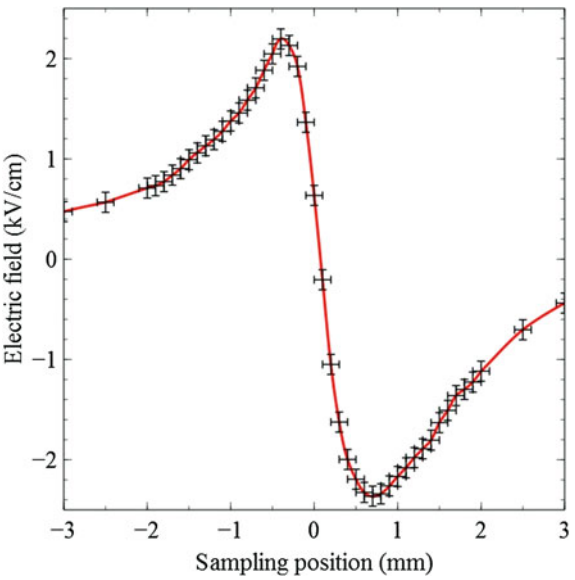

Fig. 6.9 Spatial profile of the transversely polarised terahertz electric field component. These data were obtained by keeping the temporal delay stage fixed (t = 0) and scanning the sampling position stage

profile can be obtained by looking directly at the electro-optic temporal scans. Figure 6.10 shows two individual time scans, one taken at a sampling position of +0.5 mm (black) and one taken at –0.5 mm (red). The terahertz electric field polarity flips as the sampling position is moved through the origin is again apparent as well as the reflection of the terahertz radiation due to the SI-GaAs.

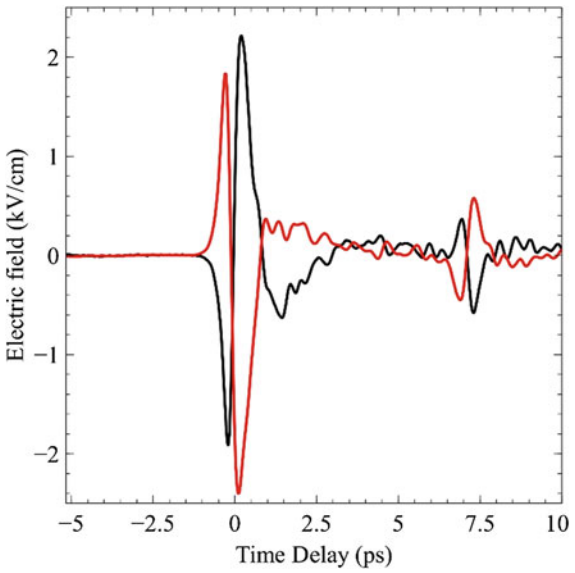

Fig. 6.10 Electro-optic time scans taken of the terahertz radiation transverse electric field at two sampling positions +0.5 mm (*black*) and −0.5 mm (*red*)

The data shown in Figs. 6.8 and 6.10 shows the terahertz electric field as a function of time. By taking the Fourier transform of these data the electric field as a function of frequency, $E(f)$, can be obtained. The power spectral density, $P(f)$, can then be calculated by taking the square of the magnitude of the electric field, $|E(f)|^2$ and is given by

$$P(f) = |FFT[E(t)G(t)]|^2, \tag{6.4}$$

where $G(t)$ is a Gaussian window function that has been applied to the time-domain data in order to remove oscillations in the frequency domain due to the sharp cut-off at the edges of the data sets. This Gaussian window function was normalised to the time-domain data and the width set such that the main peak was fully incorporated. These data can be seen in Fig. 6.11; here the power spectra are plotted as a function of frequency and sampling position.

As can be seen the higher frequencies are present in the centre of the terahertz spot whilst the lower frequencies are present more towards the edge of the terahertz spot. This is expected as the shorter wavelengths (higher frequencies) will have a smaller diffraction limited spot size. To obtain the complete spectrum of the beam this plotted function, $P(f, r)$, was integrated over the sampling position dimension, r, to obtain the power spectrum as a function of frequency. This information is shown in Fig. 6.12. As can be seen from this figure the typical near single cycle terahertz specrum is generated with a peak frequency of 0.3 THz.

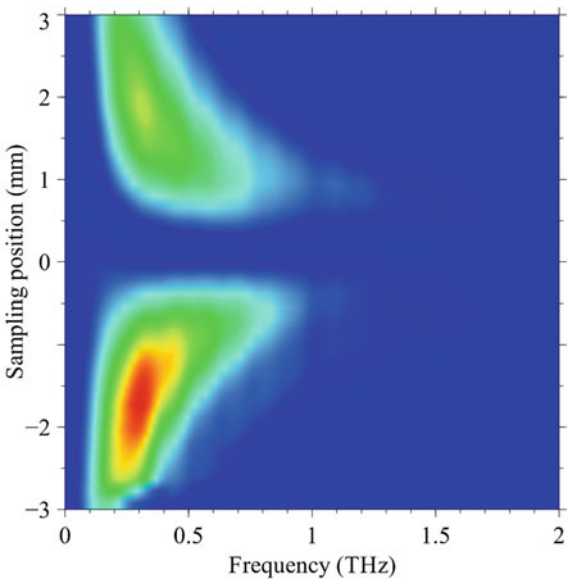

Fig. 6.11 Power spectra of the transversely polarised terahertz electric field as a function of frequency and sampling position

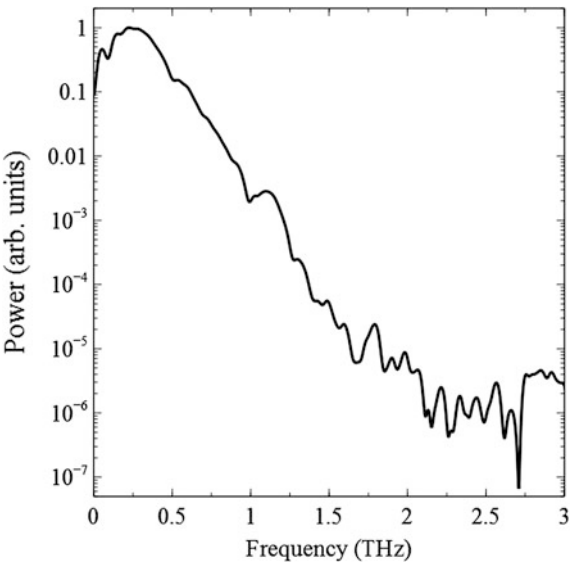

Fig. 6.12 Power spectrum obtained from integrating over the sampling position axis

6.8 Longitudinally Polarised Terahertz Radiation

Figure 6.13 shows electro-optic time scans that were obtained as a function of transverse position with the ZnTe (100)-cut crystal in place. Due to the geometry of the cut of the detection crystal it was only sensitive to the terahertz polarisation that

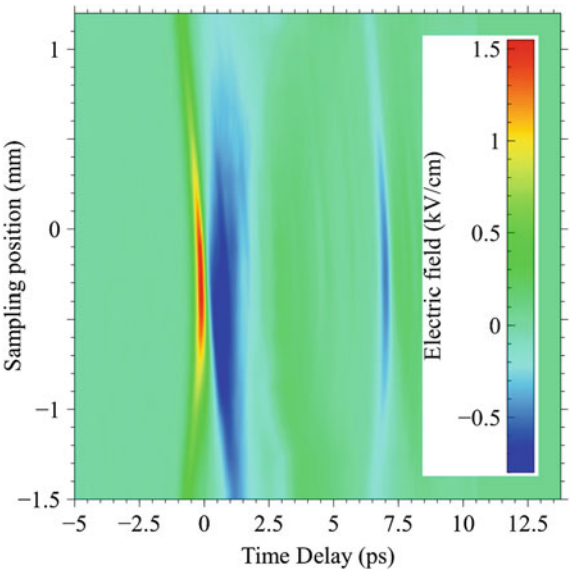

Fig. 6.13 Electro-optic time scans as a function of sampling position. Data taken using a (100)-cut ZnTe crystal and horizontally polarised probe beam

was aligned in the direction of propagation i.e. longitudinally polarised terahertz radiation. In this figure the electro-optic time scans were taken as a function of sampling position, where the sampling dimension was orthogonal to the polarisation of the terahertz radiation being detected. The data were taken with an electrical bias voltage of 40 kV applied to the PCA. The main terahertz pulse can be seen at a time delay of 0 ps and is centred on a sampling position of 0.1 mm.

The transverse profile of the terahertz electric field, taken a long time $t = 0$ ps, displays a unipolar shape as expected from a longitudinally polarised field component. The temporal profile of the longitudinally polarised component shows a bipolar shape, which is consistent with the derivative of the transverse field.

A terahertz pulse reflected in the SI-GaAs wafer can be seen at approximately 7 ps. This reflection has the opposite polarity to the main pulse which, for the same reasons explained in Sect. 6.7, is expected. More information can be gained regarding the temporal properties of the longitudinal field by plotting a single time scan. The data can be seen in Fig. 6.14. The SI-GaAs reflection can be seen at roughly 7 ps; its polarity flip is a clear indication that it is indeed a reflection of the terahertz radiation.

More information could be gained by taking a line out and plotting the electric field as a function of sampling position for a fixed time delay. A time delay of −0.17 ps was selected as this was where the longitudinal field was maximum. The data are shown in Fig. 6.15, where it is possible to see the unipolar shape of the field.

In order to further verify that the detected longitudinal field was as expected the transversely polarised data were used to calculate the longitudinal field. The longitudinally polarised electric field is related to the transversely polarised field by

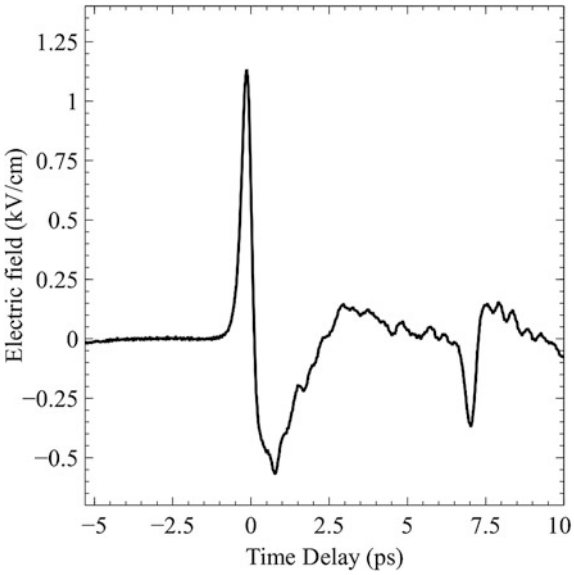

Fig. 6.14 Electro-optic time scan taken at a sampling position of 0 mm showing the longitudinally polarised electric field component of the terahertz radiation

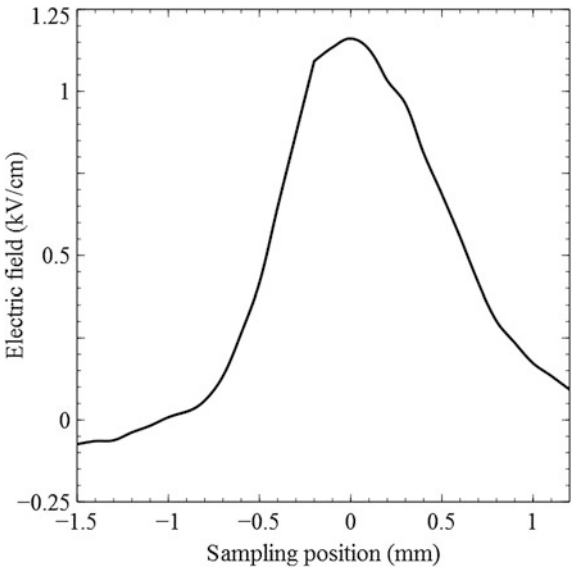

Fig. 6.15 Spatial profile of the longitudinally polarised terahertz electric field at a time delay of −0.17 ps

$$E_z(x,y,z) = -\int_{-\infty}^{\infty} \nabla_\perp E_\perp(x,y,z)dz + C(x,y), \tag{6.5}$$

where $E_z(x,y,z)$ is the longitudinally polarised electric field component, $E_\perp(x,y,z)$ is the transversely polarised electric field component, $\nabla_\perp = \bar{x}\frac{\partial}{\partial x} + \bar{y}\frac{\partial}{\partial y}$ which represents the spatial gradient and $C(x,y)$ is a constant which for the case of pulsed radiation must be zero. By assuming cylindrical symmetry and taking the measured field to be equivalent to the radial field it is possible to express this in cylindrical co-ordinates:

$$E_z(r,\phi,z) = -\int_{-\infty}^{\infty} \left[\frac{1}{r}\frac{\partial}{\partial r} rE_r(r,\phi,z) + \frac{1}{r}\frac{\partial}{\partial \phi}E_\phi(r,\phi,z)\right]dz, \tag{6.6}$$

where r is the radial co-ordinate and ϕ is the azimuthal angle. In this case there is no azimuthal electric field and hence the second term inside the integral can be ignored leaving

$$E_z(r,\phi,z) = -\int_{-\infty}^{\infty} \left[\frac{1}{r}\frac{\partial}{\partial r} rE_r(r,\phi,z)\right]dz. \tag{6.7}$$

Using Eq. (6.7) and the data obtained from the transversely polarised scans the expected longitudinal field as a function of sampling position and time can be

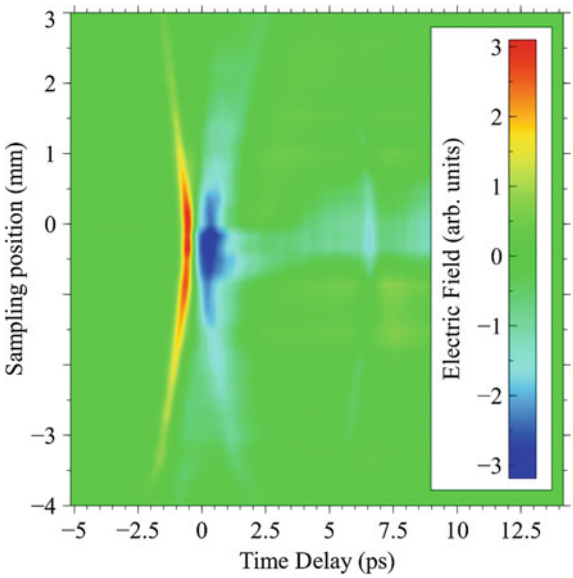

Fig. 6.16 Calculated longitudinally-polarised electric field component as a function of sampling position and time delay calculated from the data obtained in the transversely polarised electric field measurements

obtained. These data are shown in Fig. 6.16. The central time scans, between sampling position −0.5 mm and +0.5 mm, can be neglected as r in Eq. (6.7) has been truncated in this region to avoid numerical errors due to $\frac{1}{r}$ when r tends to zero. As can be seen the calculation shows a good resemblance to the measured data displayed in Fig. 6.13. Features such as the reflection due to the PCA are present and the front positive temporal peak is shorter in time than the second negative peak.

The data shown in Fig. 6.13 represent the terahertz electric field as a function of time. By taking the Fourier transform of these data the electric field as a function of frequency can be obtained as explained in Sect. 6.7. The longitudinally polarised electric field as a function of sampling position and spectral content can be seen in Fig. 6.17. The data shown in this figure take the expected form, once again with the higher frequency components present towards the centre of the beam with the lower frequency components existing towards the outer edges of the beam.

To obtain the complete spectral shape of the entire pulse the data are integrated over the sampling position dimension to give the terahertz longitudinally polarised electric field as a function of frequency. This can be seen in Fig. 6.18, where it is clear that the spectral content has a peak at around 0.2 THz.

In order to verify that the detection plane was situated at the focal plane of the terahertz radiation the temporal and sampling position delay stages were set such that the maximum longitudinal field was able to be detected. The ZnTe crystal was then placed on a separate hand-driven translation stage that enabled the crystal to be scanned both in the direction of, and orthogonal to the direction of terahertz propagation. The stage was then scanned in steps of 250 μm and the differential signal recorded at each step. The data obtained from this measurement can be seen

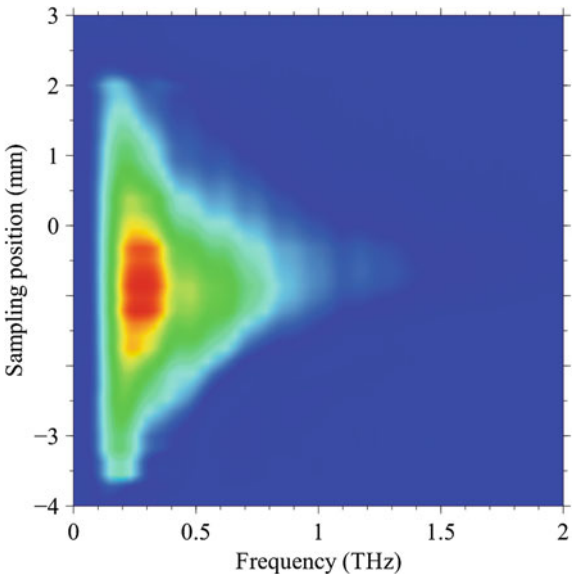

Fig. 6.17 Longitudinally polarised terahertz electric field component as a function of sampling position and frequency

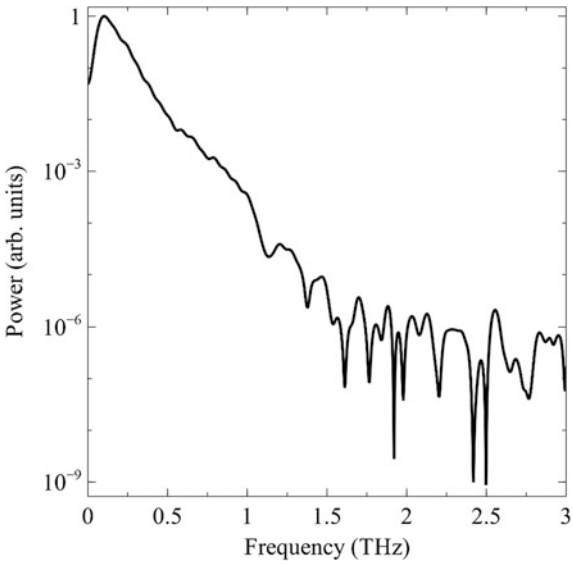

Fig. 6.18 Longitudinally polarised terahertz component as a function of frequency

in Fig. 6.19. As can be seen the maximum longitudinal differential signal exists at 0 mm. This confirmed that the ZnTe crystal was indeed situated in the focal plane of the terahertz radiation. The differential signal can be seen to decrease on both sides of this position. Two-dimensional scans were also taken with the ZnTe crystal at different longitudinal positions. These scans were taken using larger step sizes

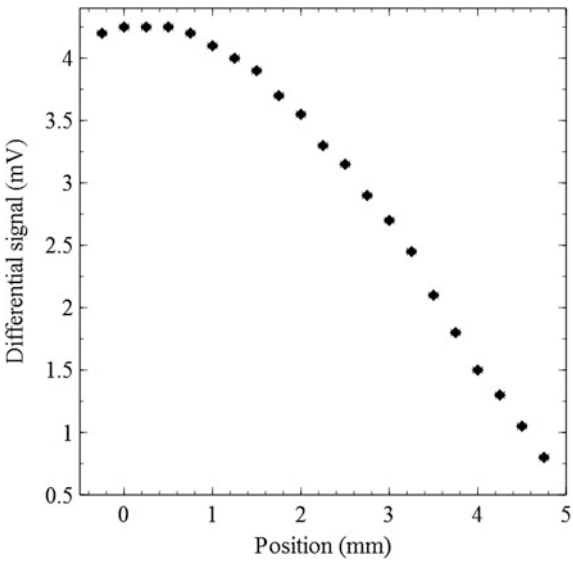

Fig. 6.19 Differential signal plotted as a function of longitudinal detection crystal position

than before however the general shape, both temporally and spatially, was confirmed to be similar. It was observed that the spot size of the longitudinal field increased as the detection crystal was moved away from the optimal position, again as expected for a focusing beam.

6.9 Field Strength Calculation

The calculation presented in Sect. 2.4.2.1 to convert the measured differential signal into an absolute electric field strength, Eq. (6.8), assumes a transversely polarised terahertz electric field and a (110)-cut ZnTe detection crystal:

$$E_{THz} = \frac{\Delta S}{S} \frac{\lambda}{2\pi c n^3 r_{41} L} \frac{C}{T}, \tag{6.8}$$

where ΔS and S are the change in the sum of the photodiode signals as measured by the lock-in amplifier, n is the optical refractive index at 800 nm, r_{41} is the non-linear susceptibility constant, L is the thickness of the detection crystal, C is the lock-in amplifier correction factor and T is the transmission coefficient. The lock-in amplifier correction factor is used to correct for the fact that the measurements with and without the terahertz radiation present are taken at different repetition rates, 500 and 250 Hz. In such a case the same terahertz electric field strength signal would give a different lock-in amplifier reading due the photodiodes response time being on the order of the repetition rate period [7]. For transversely polarised radiation,

the transmission coefficient is given by assuming continuity of the electric displacement vector, D, and takes the well-known form

$$T = \frac{2}{n+1}, \tag{6.9}$$

where n is the refractive index at the wavelength of the radiation entering the material. However for electric fields polarised orthogonal to the surface of the material continuity of the electric field vector, E, is required [8]. This modifies Eq. (6.9) such that it becomes,

$$T = \frac{2}{n(n+1)}. \tag{6.10}$$

These transmission equations can be used when calculating the electric field strength of the terahertz electric field external to the detection crystal.

In order to verify the validity of Eq. (6.8) for a longitudinally polarised electric field and a (100)-cut ZnTe crystal it is possible to use an expression for the generated polarisation term as previously explained in Sect. 2.4.2,

$$P_k^{opt} = \epsilon_0 \sum_{ij} \chi_{ijk}^{(2)} E_i^T E_j^o, \tag{6.11}$$

as the full geometric description of the optical system is contained within P_k^{opt}. Therefore if $P_k^{110} = P_k^{100}$, where in P_k^n n represents the detection geometry, any electric field strength expression that is valid for P_k^{110} must also be valid for P_k^{100}. As all of the varying geometrical entities in this case are contained within the $\chi_{ijk}^{(2)}$ and E_i^T terms it is convenient to compose a new variable D_{jk} such that

$$D_{jk} = \sum_i \chi_{ijk}^{(2)} E_i^T. \tag{6.12}$$

By now diagonalising D_{jk} for both geometrical cases it is possible to see that $D_{jk}^{110} = D_{jk}^{100}$ and therefore $P_k^{110} = P_k^{100}$. Therefore any field strength equation that is valid for P_k^{110} must also be valid for P_k^{100}. This result enables the previously derived field strength equation, Eq. (6.8), to be used for the detection of longitudinally polarised terahertz radiation as well as transversely polarised terahertz radiation.

The field strengths obtained in this experiment were all calculated using Eq. (6.8) combined with experimentally obtained data. The term "signal" will denote the value $\frac{\Delta S}{S}$ and is the measured value taken from the lock-in amplifier readings. With 40 kV applied to the PCA the transversely polarised component gave a peak signal of 0.13. This corresponded to a peak electric field strength of

2.5 kV cm^{-1}outside of the ZnTe crystal. By raising the PCA bias voltage to 100 kV a maximum signal of 0.36 was obtained giving a peak transverse electric field strength of 7.01 kV cm^{-1}. For the longitudinally polarised electric field the maximum signal with 40 kV applied to the PCA was 0.0205. This equated to a terahertz field strength of 1.26 kV cm^{-1} external to the ZnTe crystal. The signal rose to 0.036 when the wafer electric bias was increased to 100 kV giving a maximum longitudinally-polarised electric field strength of 2.22 kV cm^{-1}.

6.10 Transverse and Longitudinally Polarised Comparison

In order to again confirm that the signal measured with the (100) ZnTe crystal is indeed polarised in the direction of propagation a comparison between the data obtained with the (100) and (110) crystals was performed. First the transverse profiles of the two polarisation states were compared. Spatial profiles taken from the time scan/sampling position data for both the longitudinally polarised and transversely polarised terahertz radiation are shown in Fig. 6.20. In Fig. 6.20 in order to compare the relative size and shapes of the polarisation components each component was normalised to its maximum. The spatial profiles were taken, in both cases, from the temporal point when the fields reach their individual maxima. As can be seen the longitudinal field takes a unipolar form and the transverse field takes a bipolar form. The longitudinal field is smaller in spatial extent than the transverse

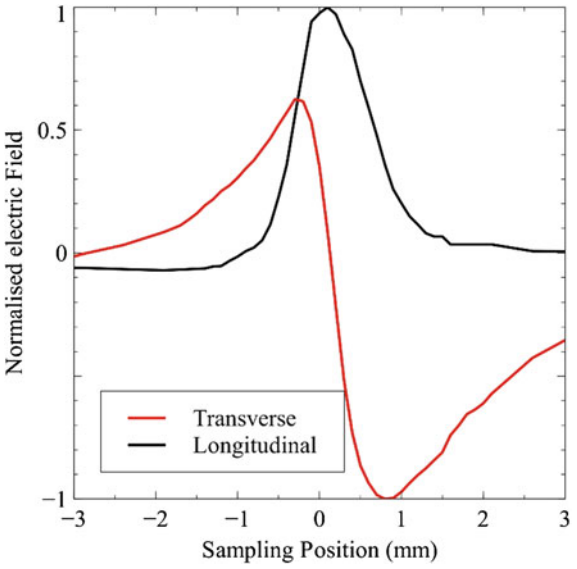

Fig. 6.20 Spatial profile of the longitudinal (*black*) and transverse (*red*) polarised terahertz electric field components taken from the temporal position with the highest electric field strengths

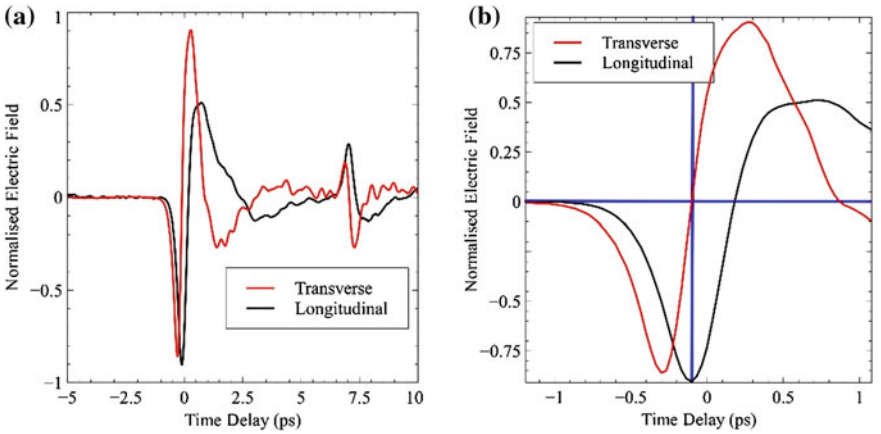

Fig. 6.21 **a** Temporal profiles of the longitudinal (*blue*) and transverse (*red*) terahertz electric field components. **b** Zoomed-in temporal profiles of the longitudinal and transverse field components with *blue lines* indicating the transverse zero-crossing point

field and fully confined within the extent of the transverse field. This aspect of the transverse—longitudinal spatial size has been utilised in many applications, and is a well-known property of radially polarised beams.

Figure 6.21a, b show the temporal profiles from both the longitudinal (black) and transverse (red) terahertz electric fields. Both field profiles were taken at spatial sampling positions such that their electric field values were maximum and normalised to their individual maxima. As can be seen there is a small time shift of 2.25 ps between the two fields. This is expected, as explained in Sect. 2.6, and can be seen in closer detail in Fig. 6.21b. In Fig. 6.21b the blue lines intersect with the transverse field when it crosses zero on the field strength axis. Using these lines as a guide it is apparent that the longitudinal field is a maximum when the transverse field is zero. As previously discussed this agrees with Winnerl et al. [5], and can be seen as further evidence that the longitudinal field measured is polarised in the direction of propagation.

It is also possible to compare the spectral content of both polarisation components. Figure 6.22 shows the electric field as a function of frequency integrated over the sampling position for both the longitudinally (red) and transversely (black) polarised terahertz field components. Surprisingly even though the longitudinally polarised component displays a smaller spot size its spectral components are more weighted towards the lower frequencies than the transversely polarised component. This is also shown in both simulations and measurements obtained by Imai et al. [9], but not fully explained. This feature could be attributed to the refractive index difference in the detection crystal axis.

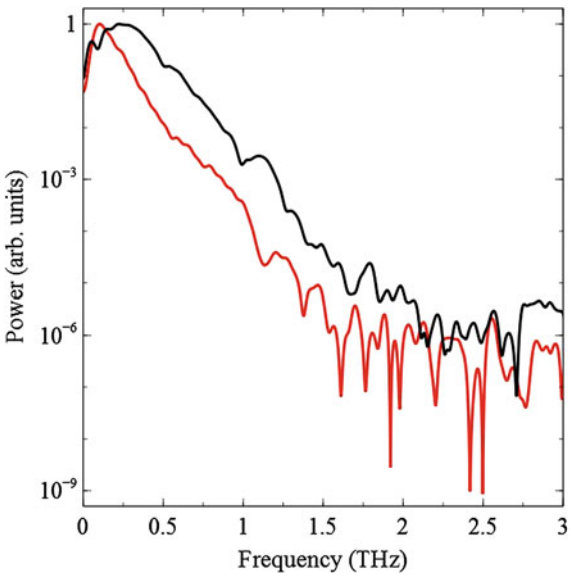

Fig. 6.22 Longitudinally (*red*) and transversely (*black*) polarised electric field components as a function of frequency integrated over the sampling range and normalised to their local maxima

6.11 Conclusion

In this chapter the work carried out on the generation and detection of both transversely and longitudinally polarised terahertz electric field components has been presented. The terahertz radiation was generated by a large-area photoconductive antenna (PCA) of dimeter 75 mm. The PCA was photoexcited by a laser pulse with an energy of 0.8 mJ and a temporal duration of 100 fs. Longitudinally polarised terahertz electric fields of 2.22 kV cm^{-1} were detected by electro optic detection.

The spatial and temporal characteristics of the longitudinal field agree with the literature as well as the comparisons made between the longitudinal and transverse components. The field strength of the longitudinal field is considerably higher than any previously published work. For instance the previous highest longitudinal terahertz field strength measured from a laser driven source was 1 kV cm^{-1} which was produced with a laser with 8 times more pulse energy using air-plasma generation [10]. The detected longitudinal electric field strength is also 100 times larger than any other published data that used similar, PCA, generation techniques [5].

Whilst there are numerous publications which describe the use of linearly polarised PCAs not much has work been published on their unique ability to produce complex polarisation states with ease. It would be useful, and possible, to perform more experiments such as the one conducted above using PCAs with various electrode configurations and sizes in attempt to further maximise and optimise the longitudinal field generated.

References

1. M.J. Cliffe, A. Rodak, D.M. Graham, S.P. Jamison, Generation of longitudinally polarized terahertz radiation with field amplitudes exceeding 2 kV/cm. Appl. Phys. Lett. **105**, 1191112 (2014)
2. S.P. Jamison, M.J. Cliffe, D.M. Graham, T. Thakker, B. Muratori, Y.M. Saveliev, R.J. Smith, W.R. Flavell, D.J. Holder, D. Newton and A. Wolski Phase space manipulation with laser-generated terahertz pulses, in *34th International Free Electron Laser Conference*, Japan (2012)
3. J.P. Conry, *Polarization properties of Maxwell-Gauss laser beams*, Ph.D. Thesis, University of Arkansas, 2012
4. D. You, R.R. Jones, P.H. Bucksbaum, D. R. Dykaar, Generation of high-power sub-single-cycle 500-fs electromagnetic pulses. Opt. Lett. **18**, 290 (1993)
5. S. Winnerl, R. Hubrich, M. Mittendorff, H. Schneider and M. Helm, Universal phase relation between longitudinal and transverse fields observed in focused terahertz beams. New J. Phys. **14**, 103049 (2012)
6. M. Schall, M. Walther, C. Winnerwisser, H. Helm and P. U. Jepsen, Subpicosecond time-resolved terahertz time-domain spectroscopy of transient carrier dynamics in semiconductors, in *SPIE International Symposium on Terahertz Radiation* (Munich, 1999)
7. A. Rodak, *Communication with*, 2014
8. J.D. Jackson, *Classical Electrodymanics* (Wiley, New York 1998)
9. R. Imai, N. Kanda, T. Higuchi, Z. Zheng, K. Konishi, M. Kuwata-Gonokami, Terahertz vector beam generation using segmented nonlinear optical crystals with threefold rotation symmetry. Opt. Express **20**, 21896 (2012)
10. Y. Minami, T. Kurihara, K. Yamaguchi, M. Nakajima, T. Suemoto, Longitudinal terahertz wave generated from an air plasma filament induced by a femtosecond laser. Appl. Phys. Lett. **102**, 151106 (2013)

Chapter 7
Non-linear Optical Crystal Generation

Within this chapter details of the generation of longitudinally polarised terahertz radiation within non-linear optical crystals are presented. The design of the different optical setups used are explained along with the results obtained from these setups. Two optical setups were designed and built using two different types of non-linear optical crystals, ZnTe (Sect. 7.3) and magnesium-oxide-doped stoichiometric lithium niobate (MgO:SLN) (Sect. 7.4). These different crystals required different pump geometries. Whilst the ZnTe crystal allowed for a co-linearly phase-matched pump scheme, the MgO:SLN crystal required a non-co-linear tilted-pulse-front pumping scheme. The terahertz radiation generated from both of the non-linear optical crystals was detected using an electro-optic balanced detection scheme with a movable probe beam allowing for both the spatial and temporal mapping of the terahertz electric field. The design and implementation of both the pumping schemes and electro-optic detection scheme is detailed within this chapter.

7.1 Introduction

The interaction between electromagnetic radiation and charged particle bunches requires the electric field of the electromagnetic radiation to be orientated in the direction of the charged particle bunch propagation. The interaction strength depends simply upon two attributes, the electric field strength of the radiation and the interaction duration. To enable the maximum interaction strength a co-linear geometry is required, and thus an electric field component in the direction of the radiation propagation. This as previously discussed is commonly referred to as the longitudinally polarised component.

As previously discussed in Chap. 6 the generation of a longitudinally polarised electric field component has been achieved via the generation of terahertz radiation

M.J. Cliffe, *Longitudinally Polarised Terahertz Radiation for Relativistic Particle Acceleration*, Springer Theses, DOI 10.1007/978-3-319-48643-7_7

through the photoexcitation of a large area photoconductive antenna. Whilst this was successful, limitations inherent to the generation device constrained the feasibility of such a device for the manipulation of relativistic charged particles. These included the inability to produce electric field strengths in the MV cm^{-1} regime and to temporally tune the waveform of the generated terahertz radiation by directly tuning the pump optical laser [1, 2]. An alternative generation technique considered here involves the non-linear generation of terahertz radiation in optical crystals. Generation within such crystals does not involve physical processes on timescales larger than the pump laser duration and so does not inherently disallow the temporal tuning of the terahertz radiation via optical pump laser manipulation. In fact the direct manipulation of the temporal waveform of the terahertz radiation via optical tuning has been demonstrated within magnesium-oxide-doped stoichiometric lithium niobate (MgO:SLN) and other common generation crystals such as ZnTe [3, 4]. It has been shown that generation techniques using such crystals have the ability to produce terahertz radiation with extremely high field strengths, on the order of 10–100's MV cm^{-1} [1, 5]. These two features make non-linear optical crystals a perfect media for the generation of terahertz radiation for the manipulation of relativistic particles.

So far discussion regarding the generation of terahertz radiation by non-linear interactions within crystals has solely focused on their ability to generate linearly, transversely-orientated, polarised terahertz radiation. As previously mentioned what is required for the interaction of terahertz radiation with an electron beam is a co-linear geometry and therefore terahertz radiation with a strong longitudinal electric field component. In Chap. 6 the generation of such a polarisation component was achieved via the generation of a radially polarised terahertz mode. Such a mode has strong spatial transverse field gradients on axis and hence contains strong longitudinal fields on axis. Such a polarisation state was simple to produce when generating terahertz radiation with a photoconductive antenna (PCA) as the polarisation state is wholly dependent upon the physical geometry of the electrodes. This, however, is not the case for non-linear generation within optical crystals.

The generation of terahertz radiation within optical crystals is typically a difference frequency or optical rectification second order non-linear process. In such a process the non-linear susceptibility tensor ($\chi^{(2)}$) component of commonly used crystals limits the microscopic generation of terahertz radiation to a linear component. Due to the transverse translational symmetry associated with crystals this therefore also limits the macroscopic generation of terahertz radiation to linearly polarised radiation. The generation of modes which contain strong longitudinally polarised electric field components must therefore be investigated further. Previously published work in this field points towards two possible methods of generating such modes from non-linear optical crystals.

The first is the segmentation of crystals; in this case multiple crystal segments are used to generate linearly polarised terahertz radiation. The segments are arranged such that when all of the linearly polarised terahertz field components are mixed in the far field they form the desired mode structure [6]. This method of

generating non-linearly polarised terahertz radiation has been used to generate radially polarised terahertz radiation with gallium phosphide (GaP). Gallium phosphide shares the same crystal symmetries as ZnTe and so the concept should be directly commutable to ZnTe [7]. The second method utilises the physics of phase matching and the velocity mismatch between the optical pump and generated terahertz radiation with the optical crystal to produce a Cherenkov-style cone of radiation. This cone of radiation has a polarisation structure that appears radial when collected and collimated [8]. The method of generating radially polarised radiation from velocity mismatching uses a (001)-cut ZnTe crystal and a Yb-doped fibre amplifier laser system [8].

Whilst both of these generation techniques provide the required polarisation state, both use crystals that are not the most efficient in generating terahertz radiation. In addition the velocity-mismatched generation technique inherently limits scalability and the efficient generation of terahertz radiation by purposefully using a non-optimal phase matching condition. Whilst the terahertz radiation generated in ZnTe and GaP is typically of low power, generating typical peak field strengths on the order of 10's to 100's V cm^{-1}, the velocity-mismatched generation technique subsequently reduces the peak transverse field strength by a factor of 3 [8]. In contrast non-linear optical materials such as stoichiometric magnesium-oxide-doped lithium niobate (MgO:SLN) provide much higher field strengths, on the order of 3–4 orders of magnitude higher [1]. MgO:SLN however has a different crystal structure to that of ZnTe of GaP, and so different $\chi^{(2)}$ symmetries and different phase-matching conditions. These new phase-matching conditions make the two generation methods discussed above impractical when combined with MgO:SLN.

While GaP and ZnTe are able to be used for terahertz generation in a co-linear phase-matching geometry, due to them having similar refractive indices for both terahertz and optical frequencies, MgO:SLN cannot. The refractive index of radiation of 800 nm wavelength within MgO:SLN is 2.21 whilst the refractive index of radiation of 0.1 mm wavelength is 5.2 [9]. This difference in refractive index means the generated terahertz waves travel much slower through the material and lag behind the generating optical wave, therefore not allowing for optimal coherent addition. If the generated optical wave is thought of as a pencil beam, such that it has zero transverse dimension, then the generated terahertz radiation forms a Cherenkov-style cone behind the optical radiation. However when a transverse extent is added to the generating wave it is found that multiple cones form which do not coherently add due to their continuous phase variation. A solution to this phase-matching problem is to use an optical pump beam with a pulse-front tilt. When the angle of this pulse-front tilt is matched inside the MgO:SLN crystal to the Cherenkov cone angle all the generated terahertz radiation adds coherently as there is a constant phase across the generation axis. Whilst this method of generation allows for the coherent addition of generated terahertz radiation the wavefronts are aligned with the Cherenkov cone angle. This means terahertz radiation is generated with a propagation direction which is at a non-zero angle to the propagating pump

beam. To enable the output coupling of the terahertz radiation, whilst still allowing the input coupling of the pump radiation, the crystal is cut with sides that allow for the normal incidence of the two beams.

As the aims of this experiment are to design and investigate the generation of longitudinally polarised terahertz radiation, strong transversely varying fields are required. Due to the points discussed above a design involving two generation crystals was decided upon. In this design each crystal generates a linearly polarised terahertz field which is subsequently collected and combined to create strong transverse field gradients and hence strong longitudinal fields.

7.2 Design

In order to produce the strong transverse field gradients that are required to generate a strong longitudinal field a design consisting of two crystals was chosen. In this design each crystal generated a single linearly polarised pulse of terahertz radiation. In order to maximise the transverse field gradient the two sources were designed such that they produced radiation with a 180° phase difference. This phase difference helped maximise the transverse field gradient with the resultant generated beam. A simulated example of such a spatial mode can be seen in Fig. 7.1. This simulated mode can be thought of as an input plane to the radiation propagation simulation discussed in Chap. 4 and would exist at the crystal exit surface.

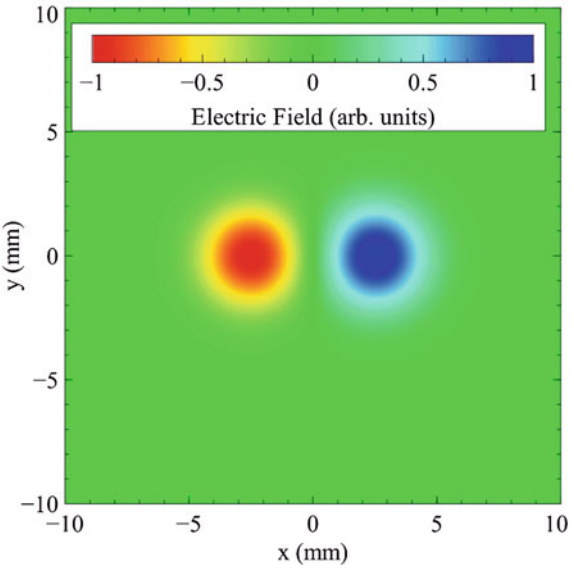

Fig. 7.1 Simulated spatial profile of two horizontally-linear polarised Gaussian beams one with a positive amplitude (*blue*) and one with a negative amplitude (*red*). This was created by the addition of two two-dimensional Gaussian beams, with *x*-axis offsets of 20 mm and FWHM diameters of 10 mm, with opposite signs

Here it can be seen that the polarisation states of both the beams are linear and pointing in the opposite direction. The radiation propagation simulation described in Chap. 4 was used to propagate the terahertz radiation through a lens and investigate its spatial and temporal properties throughout the focal region. This information was then used to calculate the longitudinal fields generated at the focus as described in Sect. 4.3. Parameters such as crystal separation, spot size and focal length were then adjusted in order to help design a source that maximised the longitudinal electric field at the centre. In order to help do this the longitudinal-to-transverse field ratio was used as a metric to compare the radiation at the focus from different generation schemes.

7.3 Preliminary ZnTe Experiment

7.3.1 Introduction

In order to test the concept of two linearly polarised terahertz pulses of opposite polarity mixing via a focusing lens and producing a longitudinally polarised field component, an experiment consisting of two ZnTe generation crystals was designed and built. Due to the co-linear phase matching that exists between near-infrared radiation and terahertz radiation within ZnTe the pump beam geometry did not require any pulse-front tilts or complex optical arrangements. This made for an ideal proof-of-principle experiment in which the concept could be tested.

7.3.2 Experimental Setup

As previously discussed the relative polarity of the terahertz radiation generated does not depend upon the relative polarity of the pump radiation. It was therefore required to rotate the two ZnTe crystals such that they produced radiation which was polarised in the correct way, in this case horizontally with a 180° phase shift between the two terahertz beams. A schematic diagram of the experimental setup used can be seen in Fig. 7.2. Here optical radiation produced by a regenerative amplifier with a pulse energy of approximately 1.8 mJ centred at a wavelength of 800 nm and with a temporal duration of 50 fs was split into two beams, a pump beam and a probe beam. The pump beam contains 90% of the optical pump energy and passes through a half waveplate allowing for control of the polarisation state of the pump radiation before it is incident upon the generation crystal. The radiation is then directed towards the generation crystals which are held in a custom-made double crystal mount. The optical radiation was aligned such that it was centred upon the two crystals which were held side-by-side with no gap between them. The pump beam spot size on the generation crystals was 12 mm in $1/e^2$ diameter thus enabling a collimated terahertz beam to be generated. Terahertz radiation generated

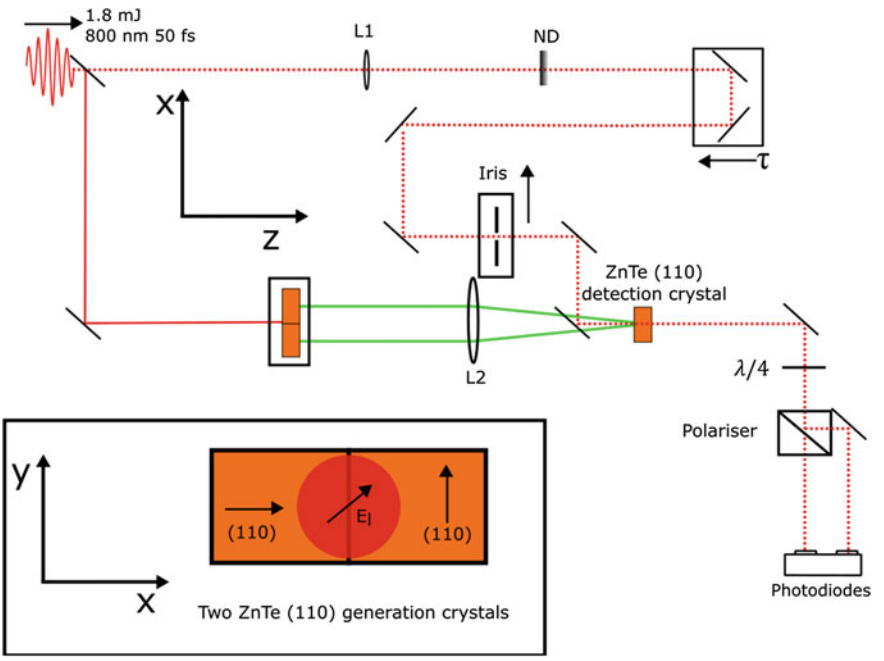

Fig. 7.2 Schematic diagram of the ZnTe generation and detection scheme. L1 is a lens of focal length 1 m, L2 a PTFE lens of focal length 300 mm and ND represents an adjustable reflective neutral density filter. The stage labelled τ is a temporal delay stage

by the two crystals was collected by L2, a 2-in.-diameter PTFE lens of focal length 300 mm situated 300 mm away from the crystals. This terahertz radiation was then focused to a focal plane 300 mm away from the lens. The probe beam which contained 10% of the optical pump energy passed through a temporal delay stage which enabled the relative time delay between the pump and the probe beam to be adjusted. After the delay stage the probe beam passed through a half-wave plate enabling control of its polarisation state. It was then apertured down using an iris, with a clear aperture of 1 mm in diameter. This iris was positioned on a hand-driven micrometre stage which travelled orthogonally to the direction of propagation of the optical radiation. The probe beam was then recombined with the terahertz radiation via a 60:40 reflection:transmission pellicle beam splitter.

Both the probe beam and the terahertz radiation were then incident one of two detection ZnTe crystals. The first was a 10 mm $\times$ 10 mm $\times$ 4 mm (110)-cut crystal employed to detect transversely polarised radiation and the second was a 10 mm $\times$ 10 mm $\times$ 2 mm (100)-cut crystal designed to detect longitudinally polarised radiation. The optical setup then consisted of a conventional balanced electro-optical detection scheme which contained a quarter waveplate, Wollaston prism and a pair of balanced photodiodes. This detection scheme was sensitive to both the amplitude of the terahertz electric field and the relative polarity. By

scanning the transverse position of the iris the terahertz electric field could be mapped as a function of both transverse space and time. To enable direct detection of both the transverse and longitudinally polarised electric fields the (110) and (100) crystals could be interchanged.

7.3.3 Results

The results obtained from this experiment include the spatial and temporal map of the terahertz radiation generated from two (110)-cut ZnTe crystals. A map of the spatial and temporal properties of the terahertz radiation generated can be seen in Fig. 7.3.

This figure shows data measured with a (110)-cut ZnTe detection crystal and hence shows terahertz radiation which is polarised horizontally (transverse). As can be seen from Fig. 7.3 there is a polarity flip as the iris is scanned over the range of −2 to 3 mm. Oscillations can be seen after the main pulse (at 0 ps) which are attributed to either water absorption of the terahertz that occurs as it propagates though air or to reflections of the optical probe within the ZnTe detection crystal and the reflections of the terahertz radiation within the ZnTe detection crystal. The polarity flip that occurs at a sampling position of approximately 0 mm can also be seen throughout all the post-pulse oscillations. A maximum differential signal, $\frac{\Delta I}{I_0}$, of 1.92×10^{-4} was measured from the data shown in Fig. 7.3 giving a maximum electric field strength of 179 V cm^{-1}. This number was calculated using Eq. (7.1) where r_{41} is the electro-optic coefficient of ZnTe and L is the ZnTe crystal thickness [10].

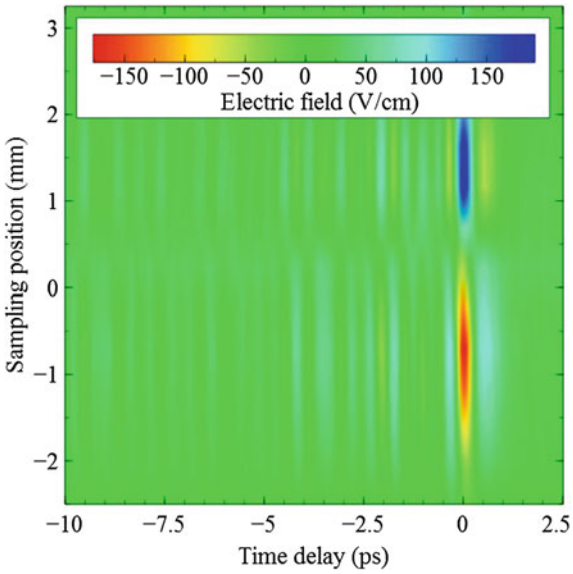

Fig. 7.3 Terahertz radiation generated by two ZnTe (110)-cut crystals at 90° to each other and a single 50 fs linearly polarised optical pump pulse as a function of sampling position and time

A transmission coefficient, T, was also included, as described in Sect. 6.9, to account for losses at the interface between air and the ZnTe crystal. A lock-in amplifier correction factor, C, was also employed as described in Sect. 6.9 [11].

$$E_{THz} = \frac{\Delta I}{I_0} \frac{\lambda}{2\pi n^3 r_{41} L} TC \tag{7.1}$$

From the data in Fig. 7.3 more information can be extracted such as the temporal profile of the transverse electric field, shown in Fig. 7.4, and the spatial profile of the terahertz radiation, shown in Fig. 7.5. In Fig. 7.4 the red line shows the temporal profile of the terahertz radiation taken at a sampling position of −1 mm whilst the black line shows the temporal profile of the terahertz radiation recorded at a sampling position of 1.25 mm. As can be seen the relative polarities of the electric fields are consistently opposite but the amplitudes are comparable in magnitude. This is to be expected from the orientation of both the pump polarisation and generation crystals. The temporal profiles of the main peaks, situated at 0 ps, show a near-single-cycle profile with a full-width half maximum height (FWHM) duration of approximately 300 fs. Figure 7.5 shows the spatial profile of the terahertz electric field measured at a temporal position of 0 ps. The spatial profile shows a FWHM of 4 mm. This is fairly large and can be attributed to the long focal length of the PTFE lens. The bipolar nature of the electric field can also be seen in Fig. 7.5. It can also be seen that the centre of the beams is not situated exactly at a sampling position of 0 mm. This is due to a slight misalignment in the pump and terahertz optics.

Direct detection of the longitudinally polarised terahertz radiation was also attempted via the same method as described above. However to detect the longitudinally polarised radiation the (110)-cut ZnTe crystal was replaced with a (100)-

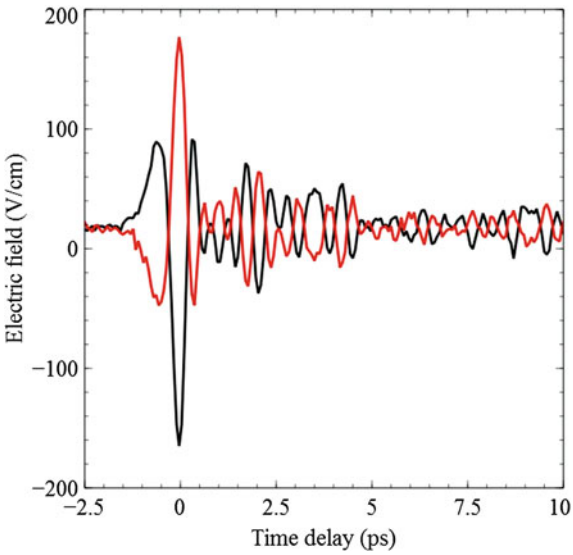

Fig. 7.4 Temporal profiles of the transverse terahertz electric fields generated by two (110)-cut ZnTe crystals. The *red line* shows the temporal profile taken at a sampling position of −1 mm whilst the *black line* shows the temporal profile taken at a sampling position of 1.25 mm

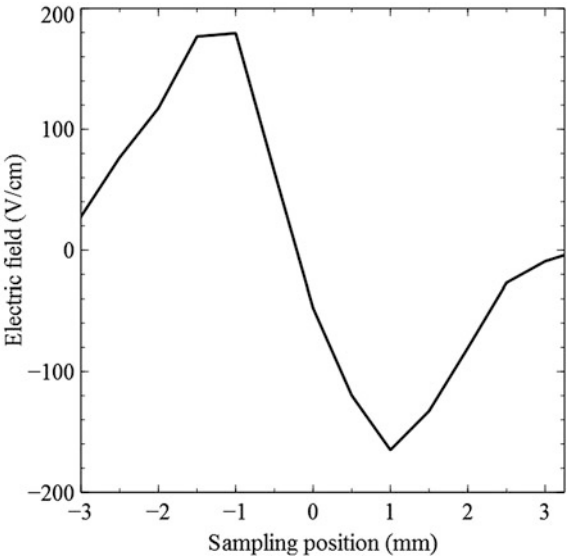

Fig. 7.5 Spatial profile of the transverse terahertz electric field taken at a temporal delay of 0 ps

cut ZnTe crystal. This was because the (110)-cut ZnTe crystal was only sensitive to a transversely polarised terahertz electric field whilst a (100)-cut ZnTe crystal is sensitive only to the longitudinally polarised terahertz electric field component. No longitudinally polarised terahertz radiation was detected. This is attributed to the low absolute electric field strengths measured by the (110)-cut ZnTe crystal and the long focal length of the PTFE lens. Whilst the longitudinally polarised electric field component was not directly detectable its electric field strength can be calculated from the detected transversely polarised electric field. This can be done using the method described in Sect. 4.3 assuming that the spatial profile does not change rapidly as a function of the longitudinal position. As the beam is not tightly focusing this is a reasonable assumption to make. The calculated longitudinal field as a function of time and sampling position can be seen in Fig. 7.6. Here it can be seen that the calculated electric field is only 9.3 V cm^{-1}. Such a low field would be undetectable using a regenerative amplifier based electro-optic detection setup. Using the measured transverse electric field strength and the calculated longitudinal electric field strength a longitudinal-to-transverse field ratio of 5.2% was calculated. The calculated longitudinal field displayed the characteristic bipolar temporal profile and the unipolar spatial profile.

7.3.4 Discussion

This experiment was useful to test the concept of intefereometrically combining two terahertz pulses via a lens to form a spatial mode with on axis longitudinal

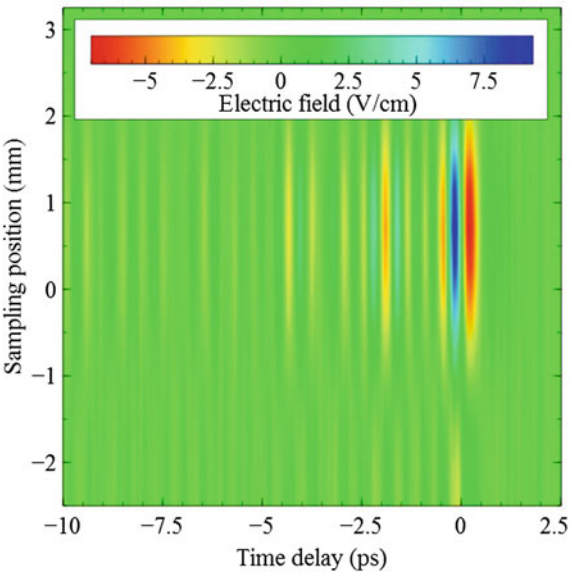

Fig. 7.6 Longitudinally polarised terahertz electric field as calculated from the measured transversely polarised terahertz electric field, Fig. 7.3, as explained in Sect. 4.3

components. The terahertz electric field strength was low, as expected from a ZnTe-based source, however more importantly the transverse spatial and temporal profile displayed the expected shape and features. The polarity flip observed when moving through the sampling position (displayed in Figs. 7.3 and 7.5) shows that the correct terahertz polarisation state was generated and detected. In order to improve upon this experiment spatial profiling with a better resolution would be required. This could be achieved by using the lens and transverse stage as described in the experiments described in Chap. 6. To improve upon the longitudinal-to-transverse field ratio a setup which contains tighter focusing of the terahertz radiation would be required.

7.4 Lithium Niobate Generation

Once the concept of combining two terahertz pulses via a lens had been investigated and shown to work the experiment was repeated with a terahertz source capable of producing higher electric field strengths. Magnesium-oxide-doped stoichiometric lithium niobate (MgO:SLN) is an electro-optic crystal which is capable of producing high terahertz electric field strengths, with reports in the literature of fields in excess of 10 MV cm^{-1} [1]. It was therefore decided to repeat the previous experiment but with MgO:SLN as the terahertz generation source.

7.4.1 Crystals

In order to use MgO:SLN crystals to create the required mode the crystals must be designed such that they generate the correct polarisation state. As explained in Sect. 2.3.1.2 and shown in Eq. (7.2) MgO:SLN generates linearly polarised radiation and the relative phase of this radiation can only be varied by manipulating the $\chi^{(2)}$ value of the crystal.

$$E_{THz} \propto \chi^{(2)} \left| E_{Opt} \right|^2 \tag{7.2}$$

In order to generate two linearly polarised beams with a 180° phase shift it was decided that two MgO:SLN crystals were required where one crystal had a positive $\chi^{(2)}$ and the other a negative $\chi^{(2)}$ value. This is analogues to the commonly-used periodically-poled lithium niobate crystals that are used to generate narrow band terahertz radiation. By placing these crystals together with a vertical separation, with the z-axis of the crystals aligned vertically and pumping them with vertically polarised radiation, two unique terahertz pulses are generated. These two pulses are vertically polarised and are 180° out of phase whilst being overlapped in time.

Due to the phase matching constraints between 800 nm radiation and terahertz radiation within MgO:SLN a non-linear propagation geometry is required as explained in Sect. 2.3.1.2. The crystals are therefore required to be cut in a triangular shape, as shown in Fig. 7.8. A photograph of one of the MgO:SLN crystals used within this experiment is shown in Fig. 7.7. The pump beam enters the crystal orthogonally to the surface labelled A in Fig. 7.8 in order to maximise input

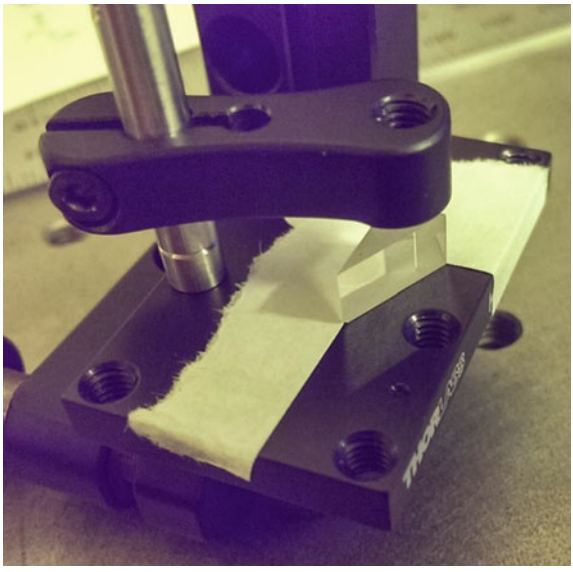

Fig. 7.7 Photograph taken of one of the MgO:SLN crystals used within this experiment

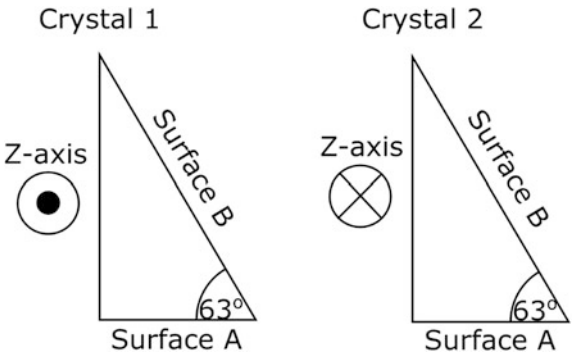

Fig. 7.8 Design of the MgO:SLN crystals used for the generation of longitudinally polarised terahertz radiation. Surface A and surface B represent the pump input surface and terahertz output surface respectively. The *z*-axis of crystal 1 is orientated out of the page whilst the *z*-axis of crystal 2 is orientated into the page

coupling and the output surface (labelled B) is cut at an angle of 63° to the input surface. This is orthogonal to the direction of the generated terahertz radiation again maximising the output coupling. Surface A was coated with an 800 nm anti-reflective coating and surface B was optically polished to a flatness of $\lambda/6$ at 640 nm. This enabled optimal input coupling and output coupling of the 800 nm and terahertz radiation respectively.

It is possible to pump the two crystals in two distinctly different pump geometries as shown in Fig. 7.9. In this figure the optical pump beam propagates into the page and the crystal *z*-axis orientations are displayed as arrows labelled by *z*. The laser polarisation orientation is also labelled by arrows labelled L. In scheme 1 the crystals are placed with one on top of the other, with the surfaces in contact with each other and are pumped by a single laser beam. Scheme 2 is similar

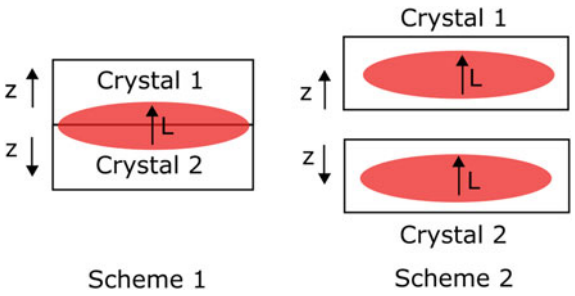

Fig. 7.9 Various pump geometries for the two MgO:SLN crystals. *z arrows* represent the *z*-axis direction for the MgO:SLN crystals and the L arrows represents the laser polarisation. In scheme 1 the two crystals are pumped by the same laser beam whilst in scheme 2 the two crystals are pumped by two separate laser beams

to 1 but with two important differences, firstly the vertical separation between the crystals can be adjusted and secondly two different pump laser beams are used. Whilst both of these schemes were proposed it was decided that scheme 1 would be implemented. The main factor in this decision was the complexity involved in having multiple pump beams as required for scheme 2.

7.4.2 Experimental Setup

An experimental setup was designed and built which is shown in Fig. 7.10. This setup used the same 1.8 mJ regenerative amplifier laser system as used in the ZnTe experiment with 90% of the beam directed towards the pump beam and 10% of the beam directed to the probe beam. This setup was re-designed such that a single MgO:SLN crystal or one of the double MgO:SLN schemes described in Sect. 7.4.1 could be used. It was necessary to enable a single crystal to be used in the same optical setup to both help with the terahertz beam alignment and to test that both the MgO:SLN crystal generated terahertz radiation that had the correct field strength and relative polarisation state.

The pump beam first passed through two cylindrical lenses of focal lengths 75 and 100 mm respectively that formed a telescope. This telescope reduced the pump beam down in one dimension producing a collimated beam with an elongated spatial profile, as shown in Fig. 7.10. The pump beam was then directed towards a holographic diffraction grating that had 1800 lines/mm. The pump beam was incident upon the grating at an angle of 35° with respect to the normal. The −1st order was reflected at an angle of 60° to the surface normal. This order had a pulse-front tilt at the grating surface of 70°. A 2-in. diameter lens with a focal length of 100 mm was used to collect the −1st diffraction order and to image the grating

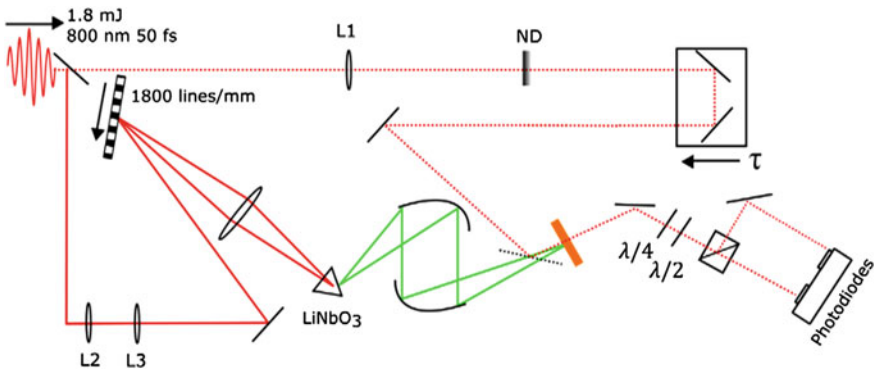

Fig. 7.10 Schematic diagram of the lithium niobate terahertz generation and detection scheme. L1 is a 1 m focal length biconvex lens, L2 and L3 are 75 and 100 mm focal length biconvex cylindrical lenses respectively which form a cylindrical telescope

surface into the MgO:SLN crystal. This produced a pulse-front tilt of 63° inside the MgO:SLN crystal at the image plane. Terahertz radiation was then collected by a 75 mm focal length gold coated off-axis parabolic mirror and directed towards a second gold coated off-axis parabolic mirror with a focal length of 100 mm. A (110)-cut ZnTe detection crystal was placed in the focal plane of the 2nd off-axis parabolic mirror and was used in conjunction with the probe beam to detect terahertz radiation.

The probe beam passed through a 1-in. diameter 1 m focal length plano-convex lens which focused the probe beam onto the ZnTe detection crystal. A neutral density filter was used to reduce the pulse energy of the probe beam such that it did not saturate the photodiodes and a temporal delay stage was used to vary the overlap time of the terahertz radiation and the probe beam. Both the terahertz radiation and probe beam were recombined via a 60:40 reflection:transmission pellicle beam splitter and were incident upon the detection crystal. A standard balanced electro-optic setup was then used to measure the temporal profile and field amplitude (including relative phase) of the terahertz radiation. This setup consisted of either a 10 × 10 × 0.5 mm (110)-cut ZnTe crystal or a 10 × 10 × 2 mm (100)-cut ZnTe crystal, a quarter wave plate, polarising beam splitter and a pair of photodiodes.

7.4.3 Single Crystal Results

The first experiment that was conducted using MgO:SLN was to confirm both the electric field strength and the relative polarity generated from both the MgO:SLN crystals. This experiment was crucial both as a learning exercise and a confirmation of the relative *z*-axis orientation. Figure 7.11 shows the terahertz waveform obtained from both MgO:SLN crystal 1 (black line) and MgO:SLN crystal 2 (red line). In order to make sure that the polarity of the terahertz generated by crystal 1 could be directly compared with the polarity of the terahertz generated by crystal 2 nothing in the optical setup was changed apart from the MgO:SLN crystal between measurements. Settings of the lock-in amplifier and photodiodes were also not changed throughout the duration of the measurement process. As can be seen in Fig. 7.11 the terahertz radiation generated by crystal 1 and crystal 2 has opposite polarities. As neither the pump beam or the probe beam polarisation was changed nor was the lock-in amplifier or photodiode settings this can be attributed to a 180° flip in the *z*-axis of the MgO:SLN crystal. Electric field strengths were also calculated from the waveforms. A maximum differential signal of 0.63 was detected which gave a maximum electric field strength of to 47 kV cm^{-1}. This was consistent between both the MgO:SLN crystals that were used. The polarity flip observed between the radiation generated by crystal 1 and crystal 2 can be seen throughout the waveforms including in the reflection at −10 ps and the water absorption oscillations observed after the main peak. This −10 ps reflection is consistent with a terahertz reflection within the ZnTe detection crystal, as the ZnTe crystal has a refractive index of 3.1 at 0.3 THz and is 0.5 mm thick.

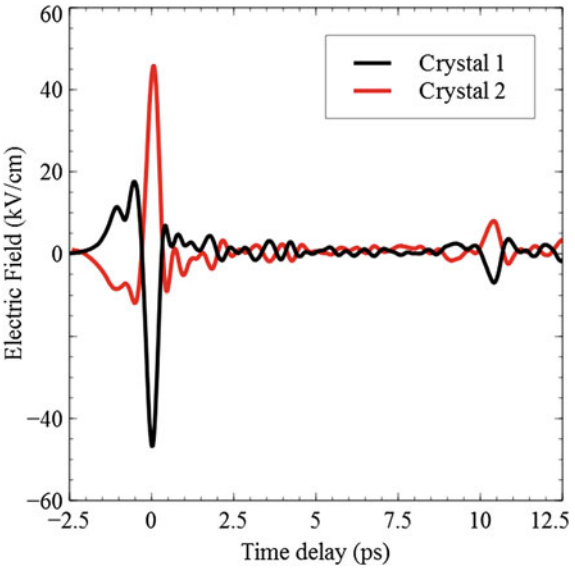

Fig. 7.11 Terahertz radiation generated by two MgO:SLN crystals and detected by electro-optic detection. The *black line* represents the radiation generated by crystal 1 whilst the *red line* represents the radiation generated by crystal 2

7.4.4 Double Crystal Results

Once both crystals had been confirmed as working and confirmed to generate the correct polarity of terahertz radiation a generation scheme consisting of two MgO:SLN crystals was built. This setup was similar to the one shown in Fig. 7.8 however an iris and orthogonal translation stage were placed after the first lens on the probe beam path. This enabled electro-optic sampling to be performed at different horizontal positions on the ZnTe detection crystal. The generation MgO:SLN crystals were positioned as shown in scheme 1 in Fig. 7.9 as this was the simplest setup to construct. Electro-optic temporal scans were then performed with the probe beam aligned to be at various horizontal positons on the detection ZnTe crystal. This measurement was performed twice, once with a (110) ZnTe detection crystal in place and once with a (100) ZnTe detection crystal in place. This enabled both vertically polarised and longitudinally polarised terahertz radiation detection as a function of time and space. Results obtained from these measurements can be seen in Fig. 7.12 where the black and red lines represent data collected with a (110) ZnTe crystal and the green line represents data collected with a (100) ZnTe detection crystal. As can be seen in Fig. 7.12 as the transverse position is scanned from 6 mm to -6 mm there is a flip in the polarity of the transversely polarised terahertz radiation. This agrees with the preliminary data obtained in Sect. 7.3 and confirms that the correct polarisation state has been generated. On axis a negligible amount of transversely polarised terahertz radiation was detected, with a field amplitude 3 orders of magnitude less than the transverse electric field maximum. From the transverse data a maximum differential signal of 0.39 was measured and using Eq. (7.1) a maximum transverse electric field of 29 kV cm^{-1} was calculated.

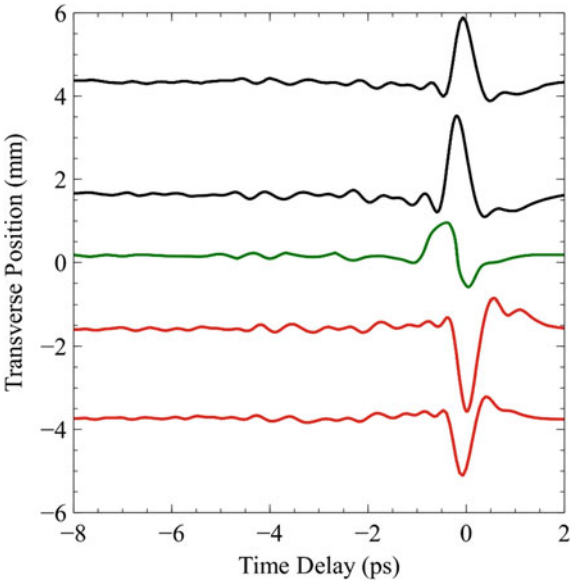

Fig. 7.12 Terahertz radiation generated by two MgO:SLN crystals with opposite vertically-orientated *z*-axis directions as a function of transverse position. *Black* and *red lines* show data collected using a (110) ZnTe crystal (transverse field) whilst the green line shows data collected using a (100) ZnTe crystal (longitudinal field)

The green trace shows the longitudinally polarised terahertz radiation as detected with a (100) ZnTe detection crystal. The temporal profile of the longitudinally polarised electric field takes the standard bipolar form as is expected and has been previously measured from other generation techniques such as the radially polarised photoconductive antenna generation technique as described in Chap. 6. A maximum differential signal of 0.21 was measured with the (100) ZnTe crystal which translates to a maximum longitudinal electric field of 11.6 kV cm^{-1} and thus giving a longitudinal-to-transverse field ratio of 0.4 (Fig. 7.12).

7.4.5 Discussion

Within this experiment the generation of strong longitudinally polarised terahertz radiation electric fields has been demonstrated. This was achieved via the generation of a complex spatial mode which was in turn generated by mixing the radiation from two MgO:SLN crystals interferometrically via the focusing of the radiation. From a single MgO:SLN crystal a peak transversely polarised electric field of 47 kV cm^{-1} was measured. This is comparable to field strengths measured with similar pump lasers and similar pump geometries [12]. Peak longitudinally polarised electric field strengths of 11.6 kV cm^{-1} were measured with electro-optic balanced detection and a (100) ZnTe crystal, whilst a maximum transversely polarised electric field strength of 29 kV cm^{-1} was measured with electro-optic balanced detection and a (110) ZnTe crystal. It is interesting to note that in a recent report by Nanni et al. [13] in 2014 electron acceleration via terahertz radiation in a waveguide

is demonstrated. In this report a linearly polarised MgO:SLN-based source is used and an on-axis accelerating gradient of 9.7 kV cm^{-1} is reported [13].

The work reported in this chapter is to the authors knowledge the only demonstration of the generation of longitudinally polarised terahertz electric fields by optical rectification within MgO:SLN and also the highest recorded free-space longitudinally polarised electric fields generated via laser based methods. As terahertz radiation generation within MgO:SLN has been shown to produce electric fields in excess of 100 MV cm^{-1} and the generation method described in this section does not alter any basic principles of a standard MgO:SLN-based terahertz generation scheme there is no reason why this method could not be scaled up to produce longitudinally polarised radiation with much higher electric field strengths than have been detected in this experiment. Scaling such a system up to produce terahertz radiation with higher longitudinally polarised electric fields could be achieved via a number of methods already addressed within the literature. Firstly the pump laser fluence could be increased. Within this experiment accounting for losses due the diffraction grating and other optical elements approximately 0.97 mJ of the original 1.8 mJ laser was incident upon the MgO:SLN surface over an area of approximately 0.25 cm^2 thus giving a pump fluence of 3.9 mJ cm^{-2}. Saturation of terahertz generation within MgO:SLN, with similar optical pump beam parameters, has been shown to occur at around 15 mJ cm^{-2} [14]. This gives the possibility of increasing the pump laser power by a factor of 3.8 times before saturation occurs, thus enabling the field strengths measured in this experiment to scaled by the same amount. It has also been shown that by cooling the MgO:SLN crystals down to 10 K it is possible to increase the electric field of the generated terahertz by a factor of 2.8 when compared to MgO:SLN at room temperature [2].

The temporal tuning of the pump laser is also another possible avenue to explore with respect to scalability. Calculations performed by Hebling et al. [2] predict that the electric field strength of the generated terahertz radiation depends strongly upon the temporal duration of the pump laser. In this paper the calculations show the optimal pump duration to be on the order of 500 fs. It is shown that by pumping MgO:SLN with pump-pulse duration of 500 fs compared to 50 fs can increase the generated terahertz electric field by a factor of approximately 8. Taking these scaling factors into account, along with the data obtained within this experiment, it is possible to predict the maximum longitudinal electric field strength that could be generated via this method. This produces an estimated maximum longitudinal electric field strength of 1.01 MV cm^{-1} which is far beyond the longitudinal electric field strength of any other known generation method.

Along with these quantifiable scaling factors there is also the possibility of increasing the crystal size. In the experiment described above relatively small, $5 \times 10 \times 9.81 \times 5$ mm, MgO:SLN crystals were used. In work performed by Kartner et al. [14] a crystal of $57.9 \times 57.9 \times 54.4 \times 25.4$ mm is used. By increasing the crystal size even more pulse energy can be used within the pump laser whilst avoiding the saturation threshold providing the ability to increase the terahertz electric field strength even more [14]. Other MgO:SLN crystal geometries

such as the one labelled scheme 2 in Fig. 7.9 also provide the possibility of increasing the detected terahertz electric field strength by increasing the effective numerical aperture of the focusing system.

7.5 Conclusion

Within this chapter two experimental setups for generating longitudinally polarised terahertz electric fields have been designed and built along with characterisation of the radiation they produced. The idea of using two ZnTe crystals to produce a polarisation state which contains a longitudinal field was tested and confirmed. Whilst the direct detection of longitudinally polarised radiation was not possible in this experiment this is not surprising due to the low transversely polarised electric field strengths measured and the long focal length used for terahertz radiation collection and focusing.

The generation of terahertz radiation via optical rectification with MgO:SLN was also investigated, single crystal experiments were performed and field strengths of 47 kV cm^{-1} were measured. This experiment was then extended into one of the two possible multi-crystal generation schemes. From this scheme transverse fields of 29 kV cm^{-1} were measured and longitudinally polarised electric fields of 11.6 kV cm^{-1} were detected, with the possibility of scaling the longitudinally polarised electric field values to in excess of 1.01 MV cm^{-1}. The correct spatial and temporal properties of both polarisation states have been detected and confirmed with the bipolar temporal and unipolar spatial characteristics of the longitudinally polarised terahertz electric field detected along with the unipolar temporal and bipolar spatial nature of the transversely polarised electric field.

References

1. J.A. Fülöp, L. Pálfalvi, S. Klingebiel, G. Almási, F. Krausz, S. Karsch, J. Hebling, Generation of sub-mJ terahertz pulses by optical rectification. Opt. Lett. **37**, 557 (2012)
2. J. A. Fülöp, L. Pálfalvi, M.C. Hoffmann, J. Hebling, Towards generation of mJ-level ultrashort THz pulses by optical rectification. Opt. Express **19**, 15090 (2011)
3. J. Ahn, A.V. Efimov, R.D. Averitt, A.J. Taylor, Terahertz waveform synthesis via optical rectification of shaped ultrafast laser pulses. Opt. Express **11**, 2486 (2003)
4. W.C. Hurlbut, B.J. Norton, N. Amer, L. Yun-Shik, Manipulation of terahertz waveforms in nonlinear optical crystals by shaped optical pulses. J. Opt. Soc. Am. B **23**, 90 (2006)
5. M. Shalaby, C.P. Hauri, Terahertz brightness at the extreme: demonstration of 5 GV/m low frequency λ^3 terahertz bullet. Arxiv (2014), Available: http://arxiv.org/abs/1407.1656
6. R. Imai, N. Kanda, T. Higuchi, Z. Zheng, K. Konishi, M. Kuwata-Gonokami, Terahertz vector beam generation using segmented nonlinear optical crystals with threefold rotation symmetry. Opt. Express **20**, 21896 (2012)
7. R.W. Boyd, *Nonlinear Optics* (Academic Press, 2003)

8. G. Chang, C.J. Davin, C. Liu, S.L. Williamson, A. Galvanauskas, T.B. Norri, Generation of radially polarized terahertz pulses via velocity-mismatched optical rectification. Opt. Lett. **32**, 433 (2007)
9. J. Hebling, G. Almási, I.Z. Kozma, K. Jurgen, Velocity matching by pulse front tilting for large-area THz-pulse generation. Optical Express **10**, 1161 (2002)
10. M.J. Cliffe, A. Rodak, D.M. Graham and S.P. Jamison, Generation of longitudinally polarized terahertz radiation with field amplitudes exceeding 2 kV/cm. Appl. Phys. Lett. **105**, 1191112 (2014)
11. A. Rodak, *Communication with*, 2014
12. M. Kunitski, M. Richter, M.D. Thomson, A. Vredenborg, J. Wu, T. Jahnke, M. Schoffler, H. Schmidt-Bocking, H.G. Roskos, R. Dorner, Optimization of single-cycle terahertz generation in $LiNbO_3$ for sub-50 femtosecond pump pulses. Opt. Express **21** , 6826 (2013)
13. E.A. Nanni, W.S. Graves, K.- H. Hong, W.R. Huang, K. Ravi, L.J. Wong, G. Moriena, R.J. Miller, F.X. Kartner, Linear Electron Acceleration in THz Waveguides, in *IPAC*, Dresden (2014)
14. S. Carbajo, K. Wu, K. Ravi, F. Ahr, G. Cirmi, Y. Zhou, O.D. Mucke, F.X. Kartner Terahertz generation in lithium niobate driven by Ti: sapphire laser pulses and its limitations. Opt. Lett. **39**, 5403 (2014)

Chapter 8
Conclusions and Future Work

Laser-driven longitudinally polarised terahertz sources have been designed and built with the aim of manipulating the energy profile of relativistic electrons. The radiation generated by both photoconductive antenna [1] and non-linear optical crystal generation methods has been profiled and characterised via electro-optic detection techniques.

A simulation which propagated electromagnetic radiation with arbitrary spatial profiles was developed. The ability to calculate the longitudinally polarised electric field component from a propagated transversely polarised electric field component was added and used to help verify and optimise the design of subsequent experiments. Effects such as the focusing of radiation via an imposed radially varying phase delay and the Gouy phase shift were observed. Key results provided by this simulation show the generation of strong longitudinally polarised electric field components from the mixing of two linearly polarised beams via a lens. In the future it would be attractive if the generated longitudinally polarised electric field component could be used in the simulation of relativistic charged particles.

Experimental details of the ALICE Energy Modulation Induced by Terahertz Radiation (AEMITR) experiment performed on the Accelerators and Lasers In Combined Experiments (ALICE) accelerator have been detailed. The experiments were limited by the lack of good in situ electro optic terahertz radiation detection and difficulties in obtaining suitable laser-electron-beam temporal synchronisation. The lack of measured terahertz radiation induced electron beam energy modulation was attributed to a combination of factors with the main one being related to the terahertz radiation source and the temporal synchronisation. Whilst this experiment did not achieve the goals that were set out a number of important experimental developments were made that will aid the success of future work. These included the importance of good in situ terahertz radiation detection along with new electron beam detection methods, such as intra-bunch background subtraction, which helped increase the sensitivity of the measurements.

M.J. Cliffe, *Longitudinally Polarised Terahertz Radiation for Relativistic Particle Acceleration*, Springer Theses, DOI 10.1007/978-3-319-48643-7_8

Large-area photoconductive antenna (PCA) based generation methods were investigated. The ability of a PCA to generate complex polarisation states by changing the geometry of the electrodes was exploited to design a terahertz source with a radially polarised electric field profile. The terahertz radiation generated by this source was fully characterised and the longitudinally polarised electric field was directly detected via electro-optical detection. This measurement was carried out as a function of both space and time enabling a two-dimensional map of the electric field profile to be measured. Absolute terahertz electric field strengths were measured for both the transverse and longitudinally polarised components. It was found that the longitudinally polarised electric field strength was much higher than any previously reported laser based source with a maximum electric field amplitude of 2.22 kV cm^{-1} being measured. Whilst this is only 2 times higher than the previously reported air-plasma based maximum longitudinally polarised terahertz electric field it is much more efficient, using a laser with 8 times lower pulse energy.

With the advances in non-linear optically based terahertz generation techniques enabling much higher electric field strengths such sources were investigated as a potential replacement to the PCA-based generation method described above. Whilst non-linear optical based sources were able to demonstrate the generation of strong longitudinally polarised terahertz electric fields they were not able to do so whilst producing radially polarised radiation. It has been demonstrated in the literature that it is possible to temporally tune the terahertz waveform of such non-linearly optical based generation techniques. Both of these aspects, the strong fields and the temporal tune ability, make such a source ideal for the generation of terahertz radiation for the energy modulation of relativistic electrons. An alternative generation scheme was therefore proposed that used two magnesium-oxide-doped stoichiometric lithium niobate generation (MgO:SLN) crystals and combined the radiation generated via a lens. It was predicted that this would generated longitudinally polarised electric fields within the focus due to the strong transverse spatial field gradients. The generation of longitudinally polarised terahertz electric fields on axis within the focal region of such a two MgO:SLN crystal generation system was demonstrated and longitudinally polarised electric fields were detected with amplitudes of 11.6 kV cm^{-1}. The potential scalability has been described in Sect. 7.4.5. The experimental exploration of this would be a useful extension of the work described here.

Reference

1. D.P. Bliss, K.S. Youngworth, T.G. Brown, Dark-field imaging with cyliderical-vector beams. Appl. Opt. **45**, 470 (2006)

Appendix

A.1 Conversion of Modulus Squared to Sinc Function

$$\begin{aligned}
&\left|\frac{e^{i\Delta k}-1}{\Delta k}\right|^2 \\
&= L^2\left(\frac{e^{i\Delta k}-1}{\Delta kL}\right)\left(\frac{e^{-i\Delta k}-1}{\Delta kL}\right) \\
&= 2L^2\frac{(1-\cos(\Delta kL))}{(\Delta kL)^2} \\
&= L^2\frac{\sin^2\left(\frac{\Delta kL}{2}\right)}{\left(\frac{\Delta kL}{2}\right)} \\
&= L^2\mathrm{sinc}^2\left(\frac{\Delta kL}{2}\right)
\end{aligned} \tag{A.1}$$

A.2 Radiation Propagation Simulation

In order to model the propagation of radiation the above expressions were converted into a MATLAB script. First a two dimensional input grid was defined. The code used is shown below. Here a two dimensional grid width x_s and height y_s is defined the number of points on the input grid is set to n^9. The width and height of the grid is set to 200 mm and the centre point is defined as zero.

```
n=9;
xs = ([0:2^n-1]./2^n-0.5)*200e-3;
ys = xs;
[Xs,Ys] = meshgrid(xs,ys);
Rs = sqrt((Xs).^2+(Ys).^2);
```


M.J. Cliffe, *Longitudinally Polarised Terahertz Radiation for Relativistic Particle Acceleration*, Springer Theses, DOI 10.1007/978-3-319-48643-7

Next an electric field distribution is defined on this input grid. Here two Gaussian beams with spatial horizontal offsets are added together. The $1/e^2$ width is set to 10 mm in both the x and y dimensions creating circular Gaussian beams.

```
sigx = 10e-3;
sigy = 10e-3;
offset = 10e-3;
Eing = exp(-((Xs-offset).^2)./(2.*sigx^2)) .*...
      exp(-((Ys).^2)./(2.*sigy^2))-...
      exp(-((Xs+offset).^2)./(2.*sigx^2)) .*...
      exp(-((Ys).^2)./(2.*sigy^2));
```

Next the interpolation grid is defined with the size of the interpolation grid being derived from the size of the input grid. The interpolation grid is required as the output grid total and element sizes are derived from z and the frequency. This therefore changes for each frequency and z-loop. The outputs are therefore interpolated onto this interpolation grid providing an output on a uniform grid.

```
xinterp = xs./4;
yinterp = ys./4;
[Xinterp,Yinterp] = meshgrid(xinterp,yinterp);
```

Next a focal length and range of z points to propagate to are defined as well as a bandwidth.

```
focallength = 75e-3;
zrange = [focallength-2e-3:0.01e-3:focallength+2e-3];
frange=[0.3e12:0.1e12:1e12];
```

A loop is now initiated which changes the z value to each value in the *zrange* array.

```
for z=zrange;
```

Inside this *zrange* loop a new loop is initiated which changes the frequency inside the loop to each of the frequencies defined within the bandwidth array. Inside the frequency loop the radially dependent phase variation that models focusing is imposed onto the input grid. The normalisation factor imposed by the bandwidth-shaping function is calculated and also applied to the input grid.

```
for f=frange

        lambda = c/f;
        k=2*pi/lambda;
        phaseThinLens = -((k.*Rs.^2)/(2*focallength));
        Esx = Eing.*exp(i.*phaseThinLens);
        w = 2*pi*f;
        sigw = 1e25;
        E0 =w.^2.*exp(-w.^2./sigw);
```

The Fourier co-ordinates are then calculated for each frequency loop and the output grid defined. This grid is unique for each frequency and z value.

```
kx = 1/(xs(2)-xs(1))*([0:2^n-1]/2^n - 0.5)*(2*pi);
ky = kx;
xi = z*kx/k;
yi = z*ky/k;
[Xi,Yi]=meshgrid(xi,yi);
Ri2 = Xi.^2 + Yi.^2;
Ri = sqrt(Ri2);
```

The propagation calculation is then performed for each frequency and z point. If it is possible the approximations listed above are used allowing for the two dimensional Fourier transform to be implemented.

```
EiTransformx = ifftshift(fft2(...
      fftshift(Esx.*exp(i*k*Rs.^2/(2*(z))))));
Eix = E0.*-i*(k/(2*pi))*(exp(i*k*(z))/z).*...
      (exp(i*k*Ri2/(2*z))).*EiTransformx;
Eix = Eix.*exp(-i.*k.*focallength);
Erf(:,:,fcounter) = Eix;
```

The frequency loop is now ended and the variable *Erf* which is a function of (x, y, ω) is summed over the frequency dimension. This output is then interpolated onto the interpolation output grid.

```
Efsum = squeeze(sum(Erf,3));
Erz(:,:,zcounter) =...
      interp2(Xi,Yi,Efsum,Xinterp,Yinterp);
```

The propagated beam is then stored in a three dimensional array as a function of $(x_{\text{interp}}, y_{\text{interp}}, z)$. The longitudinal field can now be calculated from this output. Depending on the input field it may be necessary to store the output and re-propagate a different polarisation state which is then summed to the saved output before the next step. To calculate the longitudinal field from this output first the transverse gradient is calculated at every z point.

```
for lmn = 1:length(zrange);
    [Gx(:,:,lmn),Gy(:,:,lmn)] = gradient(Er(:,:,lmn));
end
```

Next the cumulative sum of Gx is calculated over the 3rd dimension in the array. This represents the z direction. This is analogous to performing the integration over z and creates the longitudinal field at each z point.

```
dx=xinterp(2)-xinterp(1);
dz = zrange(2)-zrange(1);
Ez = -cumsum((Gx./dx),3).*dz;
```

This produces the variable Ez which is a function of $(x_{\text{interp}}, y_{\text{interp}}, z)$ and contains the longitudinal field. In order to now display these three dimensional fields as a function of one transverse dimension and z, either a lineout from the centre, $r = 0$, is taken or the variable is summed down over one of its transverse co-ordinates. For transversely polarised beams this is typically the dimension orthogonal to its polarisation.

The Author

Matthew J. Cliffe completed his degree in Physics at The University of Hertfordshire in 2010. Subsequently he moved to The University of Manchester to study for an M.Sc. in Photon Science. After successful completion Matthew remained at Manchester to undertake a Ph.D. in Physics, specialising in terahertz radiation and photonics, under the supervision of Dr. D.M. Graham, Prof. W.R. Flavell and Dr. S.P. Jamison. During his Ph.D. he developed terahertz radiation sources and diagnostic techniques for accelerator applications at Daresbury Laboratory. In 2015 Matthew started working as a postdoctoral research associate at The Cockcroft Institute in the field of ultrafast terahertz generation for particle acceleration.

To date Matthew has given invited international talks on the subject of terahertz generation and refereed for a number of peer-reviewed international journals. Matthew has also published a number of letters, articles and papers a list of which can be found below:

1. **M. J. Cliffe**, D. M. Graham and S. P. Jamison "Longitudinally polarized single-cycle terahertz pulses generated with high electric field strengths" *Applied Physics Letters* 108, 221102 (2016).
2. **M. J. Cliffe**, A. Rodak, D. M. Graham, and S. P. Jamison. "Generation of longitudinally-polarized terahertz pulses with field amplitudes exceeding 2 kV/cm" *Applied Physics Letters* 105, 191112 (2014).
3. D. A. Walsh, **M. J. Cliffe**, R. Pan, E. W. Snedden, D. M. Graham, W. A. Gillespie, and S. P. Jamison. "Role of misalignment-induced angular chirp in the electro-optic detection of THz waves" *Optics Express* 22, 12028 (2014).
4. **M. J. Cliffe**, D. A. Walsh, W. R. Flavell, D. M. Graham, and S. P. Jamison. "Developing terahertz sources with longitudinal polarisation components for the energy modulation of relativistic electrons". *IEEE IRMMW-THz Conference.* Germany (2013) DOI:10.1109/IRMMW-THz.2013.6665488.
5. S. P. Jamison, T. Thakker, B. Muratori, Y. M. Saveliev, R. J. Smith, **M. J. Cliffe**, W. R. Flavell, D. M. Graham, D. J. Holder, D. Newton, and A. Wolski. "Phase space manipulation with laser-generated terahertz pulses". *34th International Free-Electron Laser Conference.* Germany (2012) ISBN978-3-95450-123-6.

M.J. Cliffe, *Longitudinally Polarised Terahertz Radiation for Relativistic Particle Acceleration*, Springer Theses, DOI 10.1007/978-3-319-48643-7

6. B. F. Spencer, D. M. Graham, S. J. O. Hardman, E. A. Seddon, **M. J. Cliffe**, K. L. Syres, A. G. Thomas, S. K. Stubbs, F. Sirotti, M. G. Silly, P. F. Kirkham, A. R. Kumarasinghe, G. J. Hirst, A. J. Moss, S. F. Hill, D. A. Shaw, S. Chattopadhyay, and W. R. Flavell. "Time-resolved surface photovoltage measurements at n-type photovoltaic surfaces: Si(111) and ZnO(10$\bar{1}$0)". *Physical Review B* 88, 195316 (2013).
7. B. F. Spencer, **M. J. Cliffe**, D. M. Graham, S. J. O. Hardman, E. A. Seddon, K. L. Syres, A. G. Thomas, F. Sirotti, M. G. Silly, J. Akhtar, P. O'Brien, S. M. Fairclough, J. M. Smith, S. Chattopadhyay and W. R. Flavell. "Dynamics in next-generation solar cells: timeresolved surface photovoltage measurements of quantum dots chemically linked to ZnO(10$\bar{1}$0)". *Faraday Discussions. Royal Society of Chemistry.* (2014) DOI:10.1039/C4FD00019F.
8. B. F. Spencer, **M. J. Cliffe**, D. M. Graham, S. J. O. Hardman, E. A. Seddon, K. L. Syres, A. G. Thomas, F. Sirotti, M. G. Silly, J. Akhtar, P. O'Brien, S. M. Fairlough, J. M. Smith, S. Chattopadhyay, and W. R. Flavell. "Chemically-specific time-resolved surface photovoltage spectroscopy: Carrier dynamics at the interface of quantum dots attached to a metal oxide" *Surface Science* 641, 320 (2015).
9. B. F. Spencer, **M. J. Cliffe**, A. S. Knight-Percival, W. F. Smith, and D. M. Graham. "Single-Shot Terahertz Magneto-Spectrometer". *IEEE IRMMW-THz Conference.* Germany (2013), DOI:10.1109/IRMMW-THz.2013.6665868.